Application of Limit Analysis to Non-Linear and Non-Associative Yield Conditions

Rui Zhang

A thesis presented for the degree of

Doctor of Philosophy

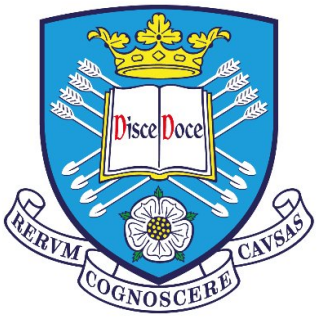

Supervisor Dr. Colin Smith

Prof. Matthew Gilbert

Department of Civil and Structural Engineering

The University of Sheffield

United Kingdom

August 2020

Application of Limit Analysis to Non-Linear and Non-Associative Yield Conditions

Rui Zhang

Abstract

Limit analysis is a widely used method for determining the collapse load of soil constructions. Conventional limit analysis theory assumes that the soil is plastic with a linear failure criterion and follows the associative flow rule. However, a linear failure criterion is often an idealisation of an actual non-linear response for which available analytical techniques are limited. The associative flow rule always overestimates the volumetric strains along shearing planes for frictional soils, potentially leading to unsafe failure loads and unrealistic failure mechanisms. Therefore, both non-linear and non-associative yield conditions require further consideration within the framework of limit analysis.

Within the framework of the numerical limit analysis procedure DLO (Discontinuity Layout Optimization), a multi-tangent technique is developed to conduct non-linear analysis of continuum geotechnical problems. A new fully general solution procedure for generating upper bound multi-wedge rigid block mechanisms for continuum soils with a non-linear power-law failure criterion is then presented. This approach utilises a curved interface that obeys the non-linear yield function flow rule along its full length. The ability of the proposed non-linear upper bound solution to predict the shear and normal stresses at every point along the failure surface is discussed, and the obtained variational solutions are verified by those from the proposed DLO non-linear approach.

The issue of non-associativity is investigated in the context of discrete rigid block limit analysis. New methods to obtain non-associative solutions are developed by separately quantifying dilation and shearing friction for frictional materials: (1) permutation method; (2) rapid direct method. The proposed non-associative procedures are applied to the determination of the load factors of rock slopes. The permutation method is able to determine the full range of

physically possible non-associative results, but is time-consuming. In contrast, the rapid direct method is fast and was shown able to generate results similar to experimental and analytical results in the literature.

Supervisors: Dr. Colin Smith and Prof. Matthew Gilbert

Acknowledgements

Finishing my PhD has, so far, been the most difficult task I have ever undertaken. It was a period of mixed feelings; I must take this opportunity to thank those who shared it with me and helped me get through it. I acknowledge, with gratitude and debt, the support of my two supervisors, Dr. Colin Smith and Prof. Matthew Gilbert without whom I could not have completed this work. I would like to thank them for selflessly extending their time and care. Special thanks go to my friends and colleagues with whom I shared a most memorable part of my life; they will forever be dear to me. I would like to acknowledge the secretaries and library staff, whose work behind the scenes is rarely appreciated.

I am grateful to the members of the thesis committee, for their insightful comments and valuable suggestions making significant improvement to the work.

I want to express my deepest appreciation to my family, particularly to my parents and my wife. The birth of my daughter also gives me a great motivation. This thesis could not have been completed without their constant encouragement and support.

Contents

Declaration

The work in this thesis is based on research carried out at the Department of Civil and Structural Engineering, University of Sheffield, England. No part of this thesis has been submitted elsewhere for any other degree or qualification, and it is the sole work of the author unless referenced to the contrary in the text.

Some of the work presented in this thesis has been published in journals and conference proceedings - the relevant publications are listed below. Such work is also referenced in the text.

Publications

Relevant Publications

Zhang, Rui, and Colin Smith. "Use of non-linear failure criteria to extract stress data from upper bound plasticity solutions." Conference: UKACM (2019), London, UK.

Zhang, Rui, and Colin Smith. "Upper bound limit analysis of soils with a non-linear failure criterion." Canadian Geotechnical Journal (2019).
DOI: https://doi.org/10.1139/cgj-2018-0513.

List of Figures

List of Tables

List of Symbols

Lowercase Symbol	Description
a	Scalar constant in power-law yield function
c	Cohesive strength
c_0	Normalisation stress in power-law yield function
c_t	Tangential cohesive strength
$\mathbf{d}$	Vector of discontinuities
$\mathbf{f}$	Vectors of block loads
$\mathbf{f}_\mathrm{D}$	Vector of dead loads
$\mathbf{f}_\mathrm{L}$	Vector of live loads
f	Yield function
$\mathbf{g}$	Vector of dissipation coefficients
g	Plastic potential
k_h	Horizontal pseudo-static acceleration coefficient
k_v	Vertical pseudo-static acceleration coefficient
m	Scalar constant in power-law yield function
m_b	Hoek-Brown constant for the rock mass
m_{bs}	Mobilized strength
m_i	Hoek-Brown constant
n_0, n_1	Integration constant coefficients
$\mathbf{p}$	Vector of plastic multipliers
$\mathbf{q}$	Vectors of joint forces
q	Surface surcharge load
v	Velocity
w	Thickness of the plastic zone

Uppercase Symbol	Description
B	Equilibrium matrix
B	Anchor width
C	Intercept matrix
$\hat{C}$	Dissipation coefficient
$\dot{D}_i$	Dissipation energy density
F	Limit load
GSI	The Geological Strength Index
N	Flow rule matrix
N	Normal force
T	Shear force
W	Weight of Soil
$\hat{W}$	Additional self weight coefficient

Greek Symbol	Description
α_i	Directional factors in the x-axis direction at discontinuity i
β_i	Directional factors in the y-axis direction at discontinuity i
γ	Weight per unit volume of soils
δ_x	Tangential displacement
δ_y	Normal displacement
ε	Total strain
$\dot{\varepsilon}$	Strain rate
$\dot{\epsilon}^p_{ij}$	Plastic strain rate
λ	Plastic multiplier
Λ	Objective function for variational method
σ_1	Effective maximum principal stresses
σ_3	Effective minimum principal stresses
σ_{ci}	Uniaxial compressive strength of the intact rock pieces
σ_h	Horizontal stress
σ_{ij}	Stress component
σ_M	Normal stress at the tangency point M
σ_n	Normal stress
σ_t	Normalisation stress in power-law yield function
σ_v	Vertical stress
τ	Shear stress
ϕ	Friction angle
ϕ_t	Tangential frictional angle
ϕ'_{crit}	Critical state friction
ϕ'_{max}	Peak friction
ψ_{max}	Maximum dilation
ψ_s	Global slip-line dilation

Chapter 1

Introduction

1.1 Motivation

Geotechnical analysis problems are broadly divided into two categories: plastic stability problems and elastic deformation problems. The methods used to deal with the two types of problems are often independent and unrelated. Plastic stability problems can include consideration of earth pressure, bearing capacity, slope stability and require the determination of the ultimate limit state (ULS).

Direct calculation methods for determining the collapse (or ultimate limit) state for geotechnical problems are popular for engineers in practical engineering. Among different direct methods (such as the limit equilibrium method and slip-line method), limit analysis is considered an efficient method for directly determining the collapse load and associated failure mechanism of a geotechnical system. As a rigorous tool based on limit analysis theory, computational limit analysis and design have developed rapidly in geotechnical applications (Smith & Gilbert 2010). For currently available computational limit analysis methods, such as finite element limit analysis (FELA) and discontinuity layout optimization (DLO), the engineer and researcher should choose an appropriate model to ensure accurate analysis. A choice will have to be made on the material model/failure criterion used, and any other required assumptions (Babiker 2013). There are a number of models used in geotechnical

engineering. The aim of the present study is to propose a model that is both simple and realistic.

Traditional limit analysis methods mainly adopt a linear failure criterion and often use translational failure mechanisms. However, the failure envelopes of many geomaterials are curved especially in the range of small normal stresses (Charles & Soares 1984, Day & Axten 1989, Maksimovic 1989). This has been demonstrated experimentally in the laboratory and field for many soils. The limit design theorems assume that the yield surface to be convex and to possess a unique normal in each of its points (Drucker et al. 1952). Conventional limit analysis theory (based on the limit design theorems) is formulated on the basis of the associative flow rule which requires that the plastic strain rate is represented by a ray normal to the yield surface and ensures a unique collapse load. However real soils, when modelled as rigid-perfectly plastic solids, do not obey the associative flow rule and the limit load is no longer unique. The adoption of the associative flow rule may result in an unrealistic failure mechanism, over prediction of the collapse load and/or volumetric locking (Cox 1963). Therefore, this work seeks to develop novel methods to enable the application of the limit analysis approach to assess the stability of the geotechnical constructions with non-linear or non-associative (abbreviated as NA) yield conditions.

1.2 Objectives and contributions

1. To develop a fully general variational approach for upper bound translational analysis in non-linear soils, extending the form of the classic upper bound multi-wedge analysis utilised for linear soils.

2. To demonstrate the proposed variational method in the calculation of a range of geotechnical problems under both static and seismic conditions.

3. To validate the variational solution against a multi-tangent analysis using

Discontinuity Layout Optimization (DLO).

4. To develop a technique for establishing all possible non-associative solutions to rock toppling/sliding problems using a permutation approach coupled with a modified limit analysis formulation.

5. To develop a robust and rapid method for determining non-associative solutions for large scale block toppling/sliding problems.

1.3 Overview of the thesis

This thesis contains nine core chapters. This chapter (Chapter 1) provides an introduction as well as a brief outline of subsequent chapters.

The reminder of the thesis is organised as follows:

In Chapter 2, the important fundamental concepts related to this research are introduced and the state-of-the-art is described through an overview of the published literature in the related research field.

Chapter 3 describes the background to discontinuity based limit analysis techniques that can be applied to both continuous media (e.g. soil) and discontinuous media (e.g. fractured rock). It also describes the use of the multi-tangent technique as an alternative approach to model non-linear soils.

In Chapter 4, the fully general variational approach for generating single translational slip-line upper bound failure mechanisms for non-linear soils is put forward. It is also shown how shear and normal stresses can be determined along slip-lines, these are compared with related lower bound solutions. This method has been published in the Canadian Geotechnical Journal (Zhang & Smith 2019).

The proposed variational method is further extended to conduct multi-wedge analysis in Chapter 5. The analysis follows the form of the classic upper bound multi-wedge analysis utilised for linear soils. This method has been published in the Ca-

nadian Geotechnical Journal (Zhang & Smith 2019) and "Use of non-linear failure criteria to extract stress data from upper bound plasticity solutions." (Conference: UKACM London, 2019).

In Chapter 6, the non-associative permutation method is developed and applied to exemplar problems.

Chapter 7 develops the rapid direct method for generating non-associative solutions for a series of rock toppling problems and presents a number of numerical examples.

Chapter 8 presents discussion of the key significant issues in this thesis and potential applications of the proposed methods are put forward.

Finally, Chapter 9 provides a summary of the key conclusions arising from this thesis with recommendations for future work.

Chapter 2

Fundamentals and state-of-the-art

2.1 Introduction

In geotechnical engineering, soil is a significant material with diverse properties and complex behaviour. The assessment of deformation and stability for soil construction is challenging. There are two broad types of calculations used in the geotechnical engineering: elastic and plastic calculations. The elastic calculation is often used to predict deformation and settlements. When the deformation of the soil gradually increases to a certain critical value, the soil will reach a plastic stage and become unstable. The plastic calculation is useful for stability prediction of geotechnical problems.

Building on earlier plastic theory, Hill (1950) and Drucker (1953) among others developed a sophisticated theoretical framework, limit analysis, allowing an "exact" collapse load to be bracketed. In terms of input, less effort is required for obtaining valid solutions by limit analysis theory when compared with other methods. Limit analysis solution may be regarded as a more rigorous solution compared with other methods, e.g. the limit equilibrium method. For the limit equilibrium method, the static admissibility of the stress field is often not satisfied, because some arbitrary assumptions are made to remove statical indeterminacy. In this thesis, both non-linear and non-associative yield conditions will be considered in the application of

limit analysis.

This chapter will introduce the limit theorem and limit analysis method including the upper and lower bound theorems. In geotechnical engineering, real soils do not obey the associative flow rule (the basic assumption of limit analysis theorem) and the limit load is no longer unique. Therefore, this chapter will distinguish the difference between the associative flow rule and non-associative flow rule by reviewing the concepts of yield function and plastic potential.

According to field tests/observations of the normal and shear stress relationship of soil/rock, different yield functions have been developed to describe the material behaviour at its yield strength. The linear Mohr-Coulomb failure criterion is a common choice by engineers, but a large amount of field tests demonstrate that the non-linear relationship between normal and shear stresses cannot be ignored. Therefore, different non-linear yield functions have been developed by researchers, such as the power-law and Hoek-Brown failure criteria. Both these yield functions are introduced in this chapter in detail, and this work adopts the power-law form to represent both of them. The yield surface curves for some classical non-linear soil/rock samples in power-law form are generated by mathematical methods in this chapter. In geotechnical engineering, the non-associative behaviour of soil/rock cannot be ignored since it is more close to the real case. Therefore, the related concepts of the non-associative flow rule are introduced to provide a basic principle for the non-associative analysis of toppling block problem in this chapter.

After introducing the important concepts relevant to this research, an overview of numerical procedures will be made. Furthermore a literature review will be conducted to introduce the state of the art for the non-linear failure analysis of geotechnical engineering and toppling-sliding failure of rock slopes.

2.2 Limit state design

Two different types of limit states are typically considered during the deformation and stability analysis of geotechnical constructions. The first one (Serviceability Limit States) is used to ensure the maximum deformation a structure can withstand while still maintaining its function is not exceeded (Terzaghi 1943). The second is Ultimate Limit State (ULS), which determines the limit load that leads to the failure of a geotechnical construction. In engineering, the limit state approach can be applied in design codes. Partial factors are adopted, which allow for probability and reliability issues and address uncertainties in the strength parameters, loading and material models (Smoltczyk 2003). Ultimate limit state design has been taken as a good design methodology to determine the collapse load (Bolton 1981) and the direct methods are normally used to calculate the ultimate limit load, the widely used direct methods will be illustrated in the following.

2.3 Direct methods of limit load calculation

The maximum load, which can be supported by a system before failure, may be calculated by direct methods without resort to any pre-failure stage (Babiker 2013). There are two main approaches: Limit equilibrium and Limit analysis. These two direct methods for calculating the limit load will be discussed below.

2.3.1 Limit equilibrium

The limit equilibrium method has traditionally been used to solve stability problems in soil mechanics (Chen & Scawthorn 1968). As an approximation of the slip-line method, the limit equilibrium method typically entails an assumed failure surface of various simple shapes, such as plane, circular, log spiral. In this method it is also necessary to make certain assumptions regarding the stress distribution

along the failure surface such that the overall equation of equilibrium, in terms of stress resultants are satisfied (Chen 1975).

2.3.2 Limit analysis

As a rigorous and concise theoretical method, limit analysis can provide an effective method for the stability evaluation of geotechnical structures. Limit analysis makes use of the simple rigid-plastic material model to directly estimate the collapse load. The rigid-plastic model assumes that elastic strain at failure is insignificant and directly studies the ultimate load of the soil mass during plastic failure. Limit analysis considers a restrictive stress-strain relationship that results in the proof of the limit theorems. Compared with the limit analysis approach, the classical limit equilibrium method basically gives limited consideration to the kinematic and equilibrium conditions.

2.4 Limit theorems

The limit analysis method is developed based on the limit theorems. The principal assumption underlying the limit theorems is Drucker's postulate (Davis & Selvadurai 2002) and the limit theorems of plasticity can be used to calculate lower and upper bound to the true collapse load, which is illustrated in the following.

2.4.1 Drucker's postulate

According to Drucker's postulate, for a stable material, positive work is done by the external agency during the application of the loads. This statement means a positive change in stress is accompanied by positive strain, as shown in Figure 2.1(a). For this case, the strain hardening material is stable. If a negative change in stress is related to an increase in strain, the work done would be negative and

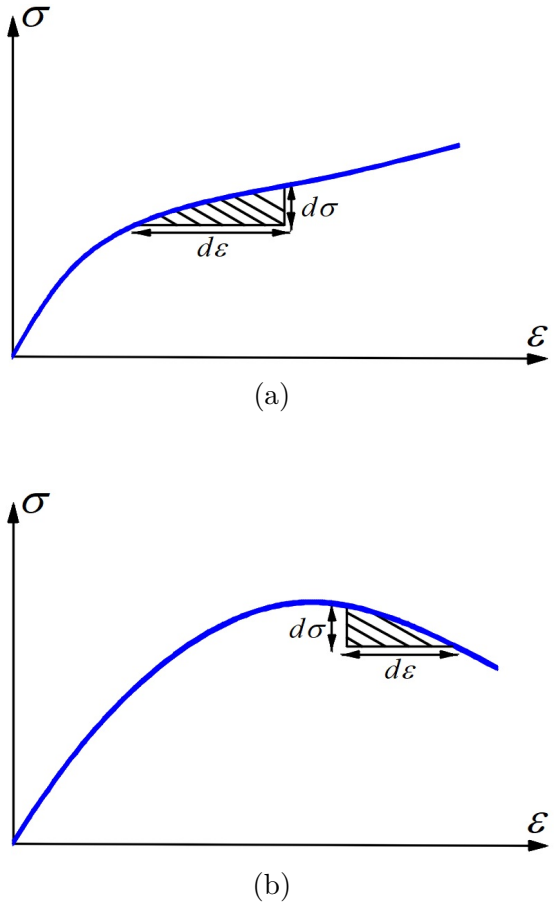

Figure 2.1: Stress-strain relationship: (a) stable material (strain-hardening), $d\sigma d\varepsilon > 0$; (b) unstable material (strain-softening), $d\sigma d\varepsilon < 0$ (after Drucker (1957)).

the strain softening material (is not applicable for limit theorems) is unstable as shown in Figure 2.1(b).

Drucker's postulate is based on not just positive work, but a maximum work principle (stable material). Arising from the assumption of Drucker's postulate, the fundamental conditions for the limit theorems could be stated as:

(i) On the basis of the principle of maximum work, the yield surface of a stable plastic material is convex, which guarantees that solutions based on the associative flow rule are unique (Babiker 2013); and (ii) the strain rate should be normal to the yield surface. This normality condition is used to prove the bound theorems of

limit analysis (Chen & Liu 1990).

The limit theorems are the foundations of limit analysis. They provide two bounds on the exact limit load, from above (upper-bound) and below (lower-bound), the statements will be introduced in the following (Chen 1975).

2.4.2 Upper bound theorem

An upper bound solution is typically found by trying different potential mechanisms and equating the work done by a system of external loads to the dissipation of energy by shear (Chen 1975). If the external work exceeds the internal energy dissipation, the soil cannot withstand the applied load. The calculated loads in kinematically admissible mechanism are greater than or equal to the actual limit loads (Babiker 2013).

2.4.3 Lower bound theorem

The statement of lower bound theorem can be defined as: if a state of stress can be found which at no point exceeds the failure criterion for the soil, failure cannot occur. The true load will be greater than or equal to the applied loads (Chen 1975). In the lower bound theorem, the stress state is not required to be the actual stress state at failure. By evaluating different admissible stress states, the maximum lower bound load can be obtained (Yu et al. 1998).

2.5 Yield function and flow rule

A yield criterion describing the yield surface could be used to determine the critical state of soil. The yield function defines the soil strength (especially the relationship between normal stress and shear stress) and material properties. The yield function

(f, F) can take the following form:

$$f(\sigma_{ij}) = F(\sigma_n, \tau) \tag{2.1}$$

where σ_{ij} is the stress tensor. The collapse will only happen when the yield condition $f(\sigma_{ij}) = 0$ (Chen & Liu 1990).

The flow rule, which explains the relationship between yield and strain rate, relates the plastic strain rate to the stress state. The plastic flow rule can be defined as (Yu 2007):

$$\dot{\epsilon}^p_{ij} = \lambda \frac{\partial g}{\partial \sigma_{ij}} \tag{2.2}$$

where g is the plastic potential and $\dot{\epsilon}^p_{ij}$ is plastic strain rate. While the differential in the right side of the equation defines the direction of strain rate, λ is a plastic multiplier that defines the magnitude of the strain rate. For the associative flow rule (known as normality flow rule), the plastic potential coincides with the failure surface, as shown in Figure 2.2.

However, the yield function cannot be used to describe the transition from elastic to plastic deformation. Therefore, the concept of plastic potential (g, G) is introduced to illustrate the nature of flow which is initiated at yield, it can be expressed as:

$$g(\sigma_{ij}) = G(\sigma_n, \tau) \tag{2.3}$$

The inception of plastic flow will be allowed only if the plastic potential equals zero. The yield function and the plastic potential are distinct and the interaction between the yield surface and plastic potential should be introduced.

In this section, four different cases for describing the relationships between the plastic potential and yield surface are introduced (Babiker 2013). As shown in Figure 2.3(a), the case which the yield surface is completely contained by the plastic

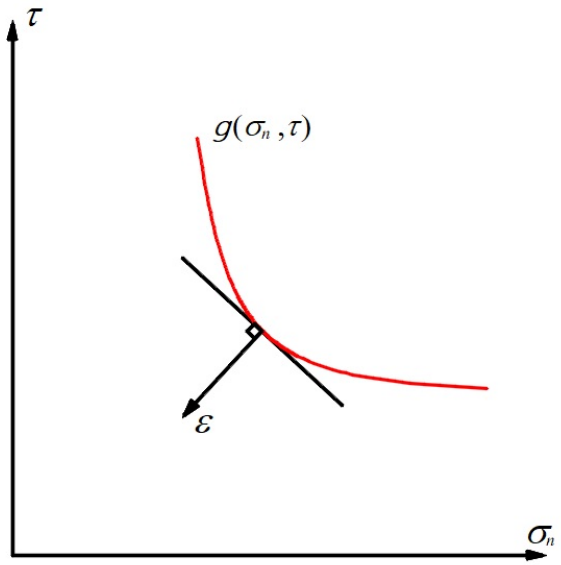

Figure 2.2: Associative flow: the strain vector ε is normal to the plastic potential g, which is also equal to the yield function.

potential will never occur since this case would require the soil to lose its integrity at its elastic stage. If the plastic potential is completely contained by the yield surface, as shown in Figure 2.3 (b), it is compatible with the proof of the lower bound theory, see Chen (1975). If the plastic potential coincides with the yield surface, as shown in Figure 2.3(c), then this is a case of associative flow which requires that the strain rate is normal to both yield surface and plastic potential. The last condition requires that the surfaces do not coincide but intersect as shown in Figure 2.3(d). In the last case, the strain rate vector is only normal to the plastic potential. A valid non-associative collapse load and failure mechanism exists at the intersection where all yield conditions are satisfied in stress level and the kinematic admissibility is guaranteed (Babiker 2013).

Most limit analysis theory based approaches adopt the linear yield function to conduct the associative analysis of soils. But a large amount of evidence shows that the yield surface should be curved and the conventional limit analysis considering the associative flow rule may overestimate stability because of the assumption of

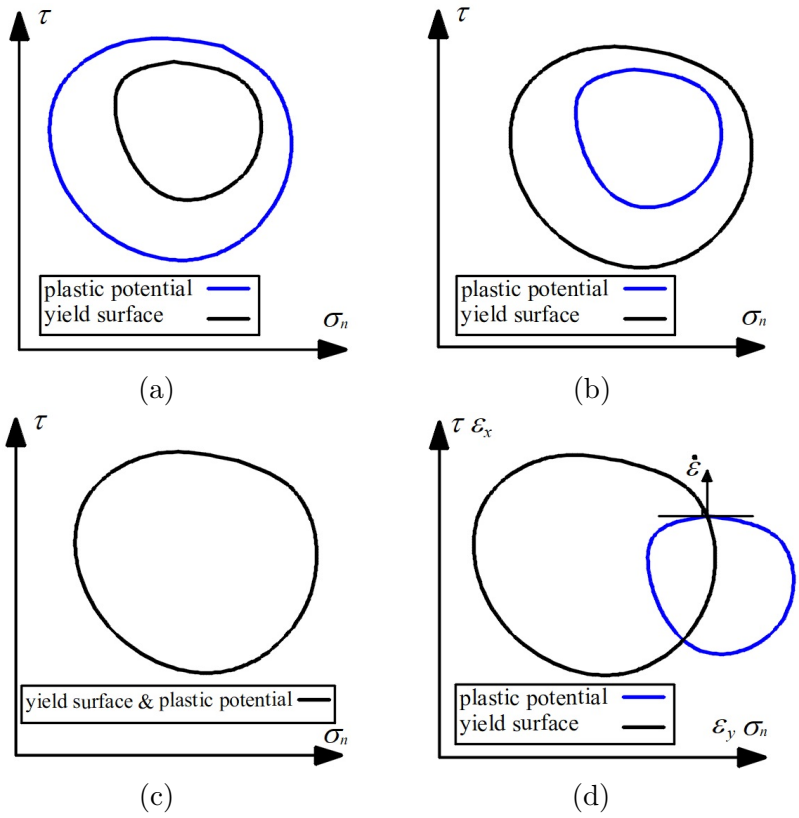

Figure 2.3: Interaction between the plastic potential g and the yield surface f: (a) f lies inside g; (b) g lies inside f; (c) g and f coincide; (d) g and f intersect.

excessive dilatancy. It is therefore necessary to introduce non-linear yield functions and the fundamentals of non-associative flow.

2.6 Linear and non-linear yield functions

In limit analysis theory, many yield functions are defined using the relationship between shear stress and normal stress. There are many yield functions used to describe the behaviours of soils and rocks. Both linear and non-linear failure criteria will be introduced below.

2.6.1 Linear failure criterion

2.6.1.1 Mohr-Coulomb model

The failure of soil will occur when the shear stress reaches a critical state (Knappett & Craig 2012). The shear strength of soil along any plane is determined by both cohesion and friction. The Mohr-Coulomb failure criterion describes the linear envelope that is obtained from a plot of the shear strength of a soil (τ) versus the applied normal stress (σ_n), shown in Figure 2.4.

$$\tau = c + \sigma_n \tan \phi \tag{2.4}$$

where c is the cohesion intercept and ϕ is the friction angle.

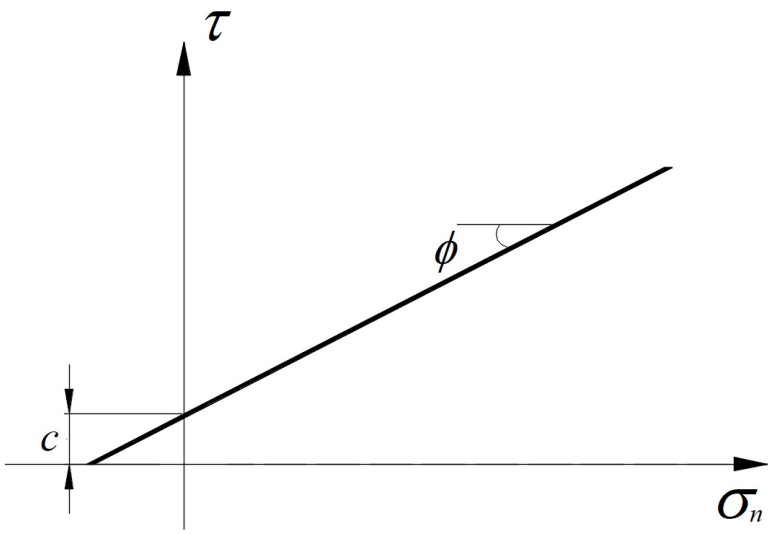

Figure 2.4: Mohr-Coulomb failure surface.

2.6.1.2 Friction and Dilation

The friction angle of soils affects the strength and resistance of soils (Sadrekarimi & Olson 2011). The particles resist shearing by interlocking when they are under

applied loading. If the soil particles roll over each other, the shearing will occur and the energy is dissipated in two ways as follows (Das 2008):

- By shearing friction due to the contact between particles in motion.
- By volume expansion due to the particles rolling over each other and rearranging (dilation).

Dilation is normally experienced by dense sands (Knappett & Craig 2012). The amount of dilation will depend on the arrangement of the soil particles and the confining pressure. Shear tests on soil mass demonstrate that the dilation may be significant if the confining pressure is low. Dilating soil has a larger peak strength than contracting or non-dilatant soils, which can be illustrated by the following empirical equation (Bolton 1986).

$$\phi'_{max} = \phi'_{crit} + 0.8\psi_{max} \tag{2.5}$$

where ϕ'_{max} is peak friction, ϕ'_{crit} is critical friction (residual) and ψ_{max} is the maximum dilation.

In terms of the relationship between dilation angle ψ and friction angle ϕ, both associative and non-associative flow cases are demonstrated in this section. Sliding block kinematics are used to illustrate the flow rule conditions. An increase in the horizontal force results in the block moving with an inclined angle ψ (dilation angle) to the horizontal. Figure 2.5(a) illustrates the classical associative case where $\psi = \phi$. In the second case, the angle of dilation takes values in the range of $0 \leq \psi < \phi$ (non-associative), shown in Figure 2.5(b). Especially, when the dilation angle equals zero, the pure-friction will occur. For sliding block (of weight W), the dissipated energy along the interface is obtained by adding the vertical distance δ_y multiplied normal force N ($N = W$) to horizontal distance δ_x along the slip surface multiplied shear force T ($T = N \tan\phi$).

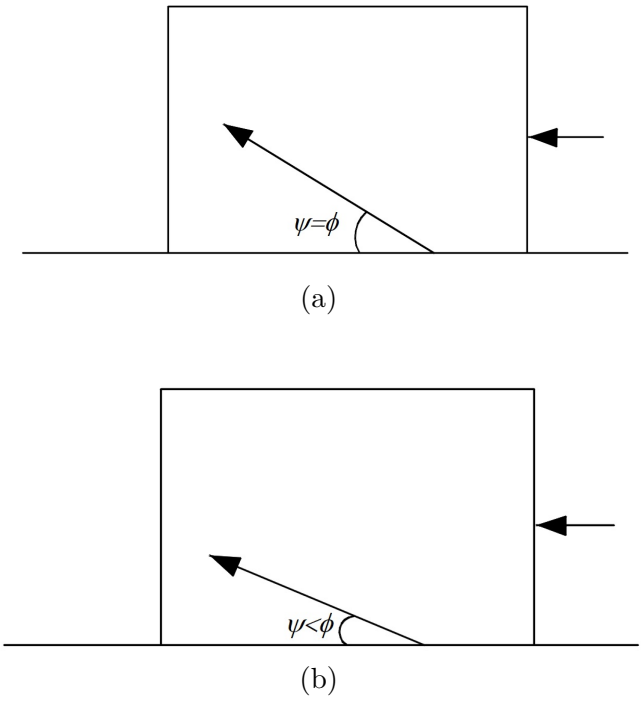

Figure 2.5: Rigid blocks kinematics illustrating the difference between associative and non-associative flow rules: (a) associative ($\psi = \phi$); (b) non-associative ($0 \leq \psi < \phi$).

2.6.1.3 Tresca model

For the Mohr-Coulomb criterion, if the frictional angle ϕ is zero, the form considering only cohesion c is called a Tresca material. The Tresca yield function is often applicable to metallic materials. In geotechnical engineering, the Tresca material normally applies to an undrained material, namely clay under short term loading, as shown in Figure 2.6.

2.6.2 Non-linear failure criterion

A large amount of experimental evidence demonstrates that failure criteria of many soils are non-linear in the range of small normal stresses (Charles & Soares 1984, Day & Axten 1989, Maksimovic 1989). For slope design, Baker (2003) and Jiang

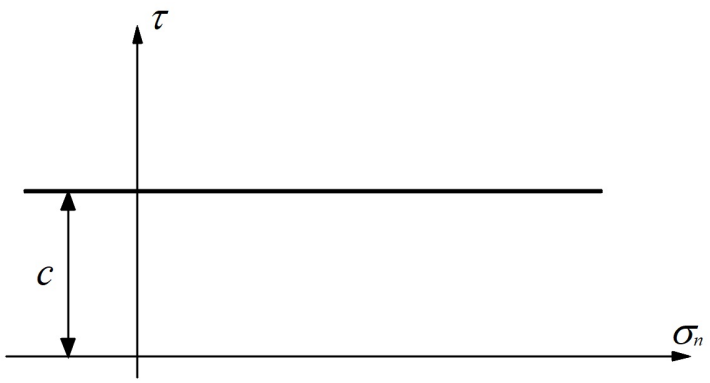

Figure 2.6: Failure surface of Tresca material.

et al. (2003) illustrated that the non-linear failure criterion plays a key role for the design.

Various non-linear yield functions have been proposed for soils and rocks, such as bilinear functions (Lefebvre 1981), the power-law failure criterion (Anyaegbunam 2013) and the Hoek-Brown failure criterion (Hoek & Brown 1997). Among these different models, the last two are widely used.

2.6.2.1 Power-law model

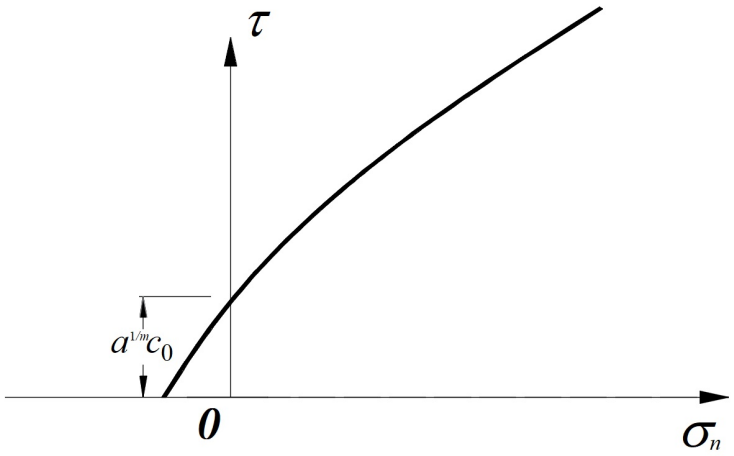

Figure 2.7: Non-linear power-law (Eq. 2.8) failure criteria.

The simple power-law failure criterion was originally proposed for rockfills by De Mello (1977):

$$\tau = A_0(\sigma_n)^n \tag{2.6}$$

where σ_n and τ are the normal and shear stresses on the failure surface, respectively; n is a coefficient to describe the non-linearity of soils. A_0 is the controlling scalar constants. Taylor (1978) discovered that for colliery spoil, $n = 0.82$. Perry (1994) gave $n = 0.60$ for London clay. Jiang et al. (2003) found $n = 0.86$ for heavily compacted Israeli clays in a drained condition. For heavily compacted rockfills, Charles & Watts (1980) found from laboratory tests that n was commonly equal to 0.75. For rocks, Li (2007) put forward a variant in the form:

$$\tau = \tau_0(\sigma_n/\sigma_0 + 1)^n \tag{2.7}$$

where τ_0 is the unconfined shear strength and σ_0 is the tensile strength.

Non-linear power-law failure criterion for geomaterials are increasingly being adopted for investigations of the stability of geotechnical problems (e.g. Zhang & Chen 1987, Baker 2004, Anyaegbunam 2013). To cover the general case, as shown in Figure 2.7, the following non-linear power-law failure criterion will be used in this study,

$$\tau/c_0 = (a + \sigma_n/\sigma_t)^{1/m} \tag{2.8}$$

where σ_n and τ are the normal and shear stresses on the failure surface, respectively; c_0 and σ_t are normalisation stresses; and a and m are scalar constants. When $m = 1$, Eq. 2.8 reduces to the well-known linear Mohr-Coulomb failure criterion, where $a = 1$, $c_o = c$ and $\sigma_t = c/\tan\phi$.

The power-law non-linear yield function can be widely used for different types of soils and rocks, such as lateritic clay (Anyaegbunam 2013), London clay, dune sand,

soft marine clay (Baker 2004), dense sand (Bolton 1986) and fractured rock mass (Hoek & Brown 1997). The parameters for a power-law yield function representation for these different soils and rocks can be obtained from the original non-linear form by generating the relevant yield surface and carrying out a least squares fit. Taking dense sand and fractured rock mass as examples, the following section will illustrate the conversion process in detail.

2.6.2.2 Bolton sand model

In order to understand the strength and dilatancy of sands, the concepts of friction and dilatancy in relation to the selection of strength parameters for design have been clarified by Bolton (1986). According to Bolton (1986), the secant angles of shearing are required in a rational approach to the strength and dilatancy of dense sands. And $\phi'_{max} - \phi'_{crit}$ is useful to measure the extra component of strength due to dilatancy in a dense sand. In terms of relative density and effective stress level, a new relative dilatancy index I_R is used. Based on the work of Bolton (1986), the definition for a relative dilatancy index can be expressed as:

$$I_R = I_D(10 - \ln p') - 1 \tag{2.9}$$

The parameters describing non-linear power-law failure envelopes are from triaxial test data (Jiang et al. 2003, Baker 2004, Anyaegbunam 2013). Therefore, according to Bolton (1986), for triaxial strain condition:

$$\phi'_{\max} - \phi'_{crit} = 3I_R^{\circ} \tag{2.10}$$

for $0 < I_R < 4$. For values of I_D that give $I_R < 0$, e.g. $I_D = 0$, the angle of shearing resistance is assumed to be ϕ'_{crit}.

2.6.2.3 Hoek-Brown model

The Hoek-Brown failure criterion was originally put forward to describe the strengths of hard rock masses and is extended to the application of a variety of rock masses including very poor quality rocks. The general form for describing jointed rock masses can be defined as:

$$\sigma_1 = \sigma_3 + \sigma_{ci} \cdot [m_b \cdot (\frac{\sigma_3}{\sigma_{ci}}) + s]^a \tag{2.11}$$

where σ_1 and σ_3 are the effective maximum and minimum principal stresses at failure, respectively. m_b is the value of the Hoek-Brown constant for the rock mass, s and a are constants which depend upon the characteristics of rock mass, and σ_{ci} is the uniaxial compressive strength of the intact rock pieces.

The Geological Strength Index (GSI), introduced by Hoek (1994) and Hoek et al. (1995), provides a system for estimating the reduction in rock mass strength for different geological conditions. GSI is greatly affected by the rock mass structure and the surface condition of the joints. According to Hoek & Brown (1997) and Anyaegbunam (2013), the parameters m_b, s, a are given by

$$\frac{m_b}{m_i} = \exp(\frac{GSI - 100}{28 - 14D}) \tag{2.12}$$

$$s = \exp(\frac{GSI - 100}{9 - 3D}) \tag{2.13}$$

$$a = \frac{1}{2} + \frac{1}{6} \cdot [\exp(-\frac{GSI}{15}) - \exp(-\frac{20}{3})] \tag{2.14}$$

where D refers to a disturbance coefficient and its values vary from 0 for the case of undisturbed to 1 for very disturbed rock materials. The magnitude of m_i can be obtained from the measured inclination of the fracture planes in compression experiments. Therefore, the value of m_i should be different with respect to specific

rock strata. The yield function was given by Hoek (1990) for the following five categories of rock masses, specifically,

1. $m_i \approx 7$ for carbonate rock masses with well-developed crystal cleavage;

2. $m_i \approx 10$ for the case of the lithified argillaceous rock;

3. $m_i \approx 15$ for arenaceous rocks with strong crystals and poorly developed crystal cleavage;

4. $m_i \approx 17$ for fine-grained polyminerallic igneous crystalline rock materials; and

5. $m_i \approx 25$ for the coarse-grained polyminerallic igneous and metamorphic rocks.

For convenience in non-linear analysis, the original form of generalized Hoek-Brown failure criterion can be written in power-law form (Hoek & Brown 1997) by generating the relevant yield surface and carrying out a least squares fit.

2.7 Exemplar non-linear materials in power-law form

2.7.1 Bolton sand model

In this thesis the value of ϕ'_{crit} of 33° has been used which is typical for a quartz sand (Bolton 1986). The relevant yield surface curve for sand on a $\tau - \sigma_n$ plane can be generated using Eq. 2.9 with Eq. 2.10. As shown in Figure 2.8, curves of power-law form can be produced for any given I_D.

2.7.2 Hoek-Brown fractured rock model

The relationship between the normal and shear stresses can be expressed in terms of the corresponding principal effective stresses as suggested by Hoek & Brown

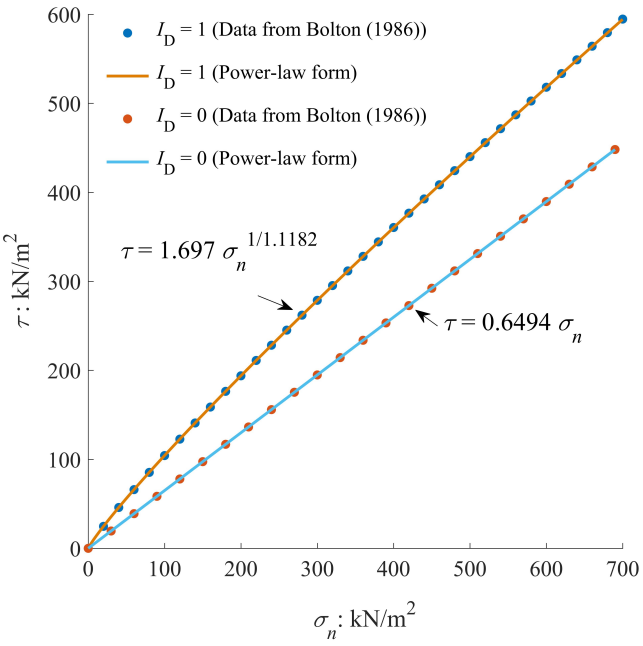

Figure 2.8: Mohr envelopes derived from empirical relations for triaxial tests on quartz sands.

(1997):

$$\sigma_n = \sigma_3 + \frac{\sigma_1 - \sigma_3}{\partial\sigma_1/\partial\sigma_3 + 1} \tag{2.15}$$

$$\tau = (\sigma_1 - \sigma_3)\sqrt{\partial\sigma_1/\partial\sigma_3} \tag{2.16}$$

$$m_b = m_i \exp((GSI - 100)/28) \tag{2.17}$$

When $GSI > 25$,

$$s = \exp((GSI - 100)/9), a = 0.5 \tag{2.18}$$

$$\partial\sigma_1/\partial\sigma_3 = 1 + \frac{m_b\sigma_{ci}}{2(\sigma_1 - \sigma_3)} \tag{2.19}$$

When $GSI < 25$,

$$s = 0, a = 0.65 - GSI/200 \tag{2.20}$$

$$\partial\sigma_1/\partial\sigma_3 = 1 + am_b^a(\frac{\sigma_3}{\sigma_{ci}})^{(a-1)} \tag{2.21}$$

The tensile strength of the rock mass is calculated from

$$\sigma_{tm} = \frac{\sigma_{ci}}{2}(m_b - \sqrt{m_b^2 + 4s}) \tag{2.22}$$

The equivalent Mohr envelope may be written in the form:

$$Y = \log A + BX \tag{2.23}$$

where $Y = \log(\frac{\tau}{\sigma_{ci}})$, $X = \log(\frac{\sigma_n - \sigma_{tm}}{\sigma_{ci}})$

The modified Hoek-Brown failure criterion in power-law form can be expressed as

$$\tau = A\sigma_{ci}[(\sigma_n - \sigma_{tm})/\sigma_{ci}]^B \tag{2.24}$$

Using the value of σ_{tm} calculated from Eq. 2.22 and a range of values of τ and σ_n calculated from Eqs. 2.15 and 2.16, the values of A and B are determined by linear regression where:

$$B = \frac{\sum XY - (\sum X \sum Y)/T}{\sum X^2 - (\sum X)^2/T} \tag{2.25}$$

$$A = 10^{(\sum Y)/T - B((\sum X)/T)} \tag{2.26}$$

And T is the total number of data pairs included in the regression analysis. The fit for the fractured rock is shown in Figure 2.9.

Let $\sigma_{ci} = \sigma_t$, $A\sigma_{ci} = c_0$, $-\sigma_{tm}/\sigma_{ci} = a$, $B = 1/m$, the Hoek-Brown failure criterion can be expressed in power-law form proposed in this thesis.

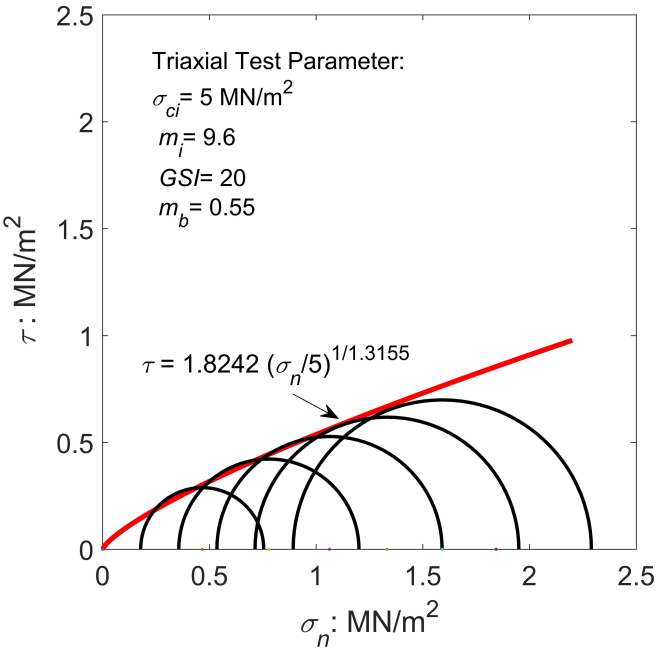

Figure 2.9: Power-law curve fitting for Mohr circle describing fractured rock by Hoek-Brown failure criterion.

2.8 Non-associative flow rule

2.8.1 Frictional material with non-associative flow rule

In general, for frictional material, the flow rule can be divided into associative flow, e.g. Hill (1950), Drucker (1953); or non-associative flow, e.g. De Josselin De Jong (1959), Cox (1963), Spencer (1964), Davis (1968), Collins (1969), Mehrabadi & Cowin (1978), Drescher & Detournay (1993). Non-associativity applies to frictional (granular) material only. For cohesive soils (e.g. undrained clay), the flow rule is naturally associative. Hence, this work adopts the Mohr-Coulomb yield criterion as

the basis for exploring the effects of non-associativity. In terms of different values of dilation angle ψ, two different cases should be considered to model non-associative behavious. One case requires $0 < \psi < \phi$, which leads that the shearing resistance is shared between the frictional and dilational elements of the material. The other case defines dilation angle $\psi = 0$. Here shearing occurs at a constant volume as the material is non-dilatant. An example of this is two rigid blocks sliding over each other.

2.8.2 Coaxial and non-coaxial strain increments

Among the limit load calculations that considered non-associative flow, solutions can be categorised as coaxial, e.g. Davis (1968), Collins (1969), Drescher & Detournay (1993) and non-coaxial, e.g. De Josselin De Jong (1959), Cox (1963), Spencer (1964), Mehrabadi & Cowin (1978). The assumption of coaxiality suggests that the principal axes of stress and plastic strain-rate coincide. However, this assumption is not supported by some experimental work (Roscoe 1970, Drescher & De Jong 1972) and numerical studies (Thornton & Zhang 2006) for frictional material.

Due to the limitation of the assumption of coaxiality, non-coaxiality of the stress and strain vector has been proposed. De Josselin De Jong (1959) proposed a non-coaxial model for describing the plastic flow of granular material. A brief representation of a coaxial and non-coaxial flow rule is illustrated in Figure 2.10. The strain rate is denoted $\dot{\varepsilon}$. The vector perpendicular to the Mohr-Coulomb surface is coaxial while the other two are non-coaxial. The assumption of non-coaxiality allows for a range of non-associative solutions to be developed, which is different from coaxial case.

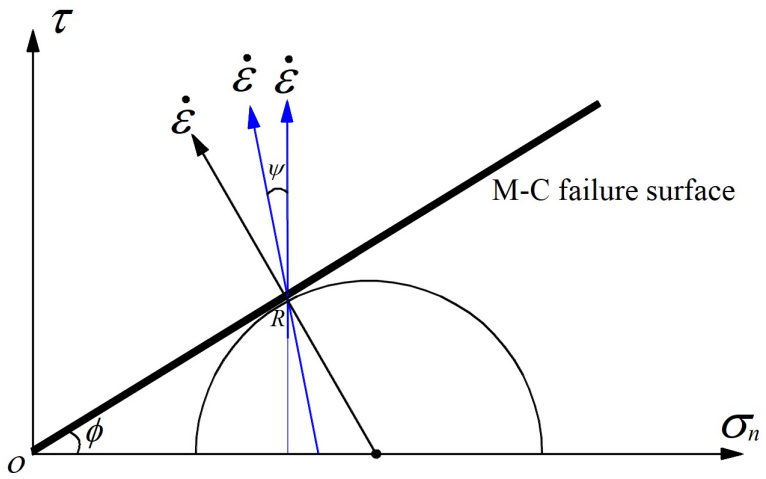

Figure 2.10: Coaxial and non-coaxial concepts: only the black strain vector is associative (it is normal to the yield surface) and coaxial (it intersects the centre of the Mohr's circle).

2.8.3 Underlying principles for this work

For associative flow, the yield function coincides with the plastic potential, leading to $\psi = \phi$. For non-associative flow, as discussed in Section 2.5, the yield surface will cross the plastic potential at point R shown in Figure 2.11. The direction of plastic strain vector should be normal to the plastic potential. According to Figure 2.11, a point R on the MC failure surface (indicated by the solid line), where the normal stress is given by ($\sigma_n = \sigma_n$') and the shear stress ($\tau = \sigma_n \tan\phi$). The associative flow rule clearly requires ($\psi = \phi$). For the non-associative case, the plastic potential surface should be represented by the dashed line ($\tau = c^* + \sigma_n \tan\psi$) to make sure the dilation angle $\psi < \phi$.

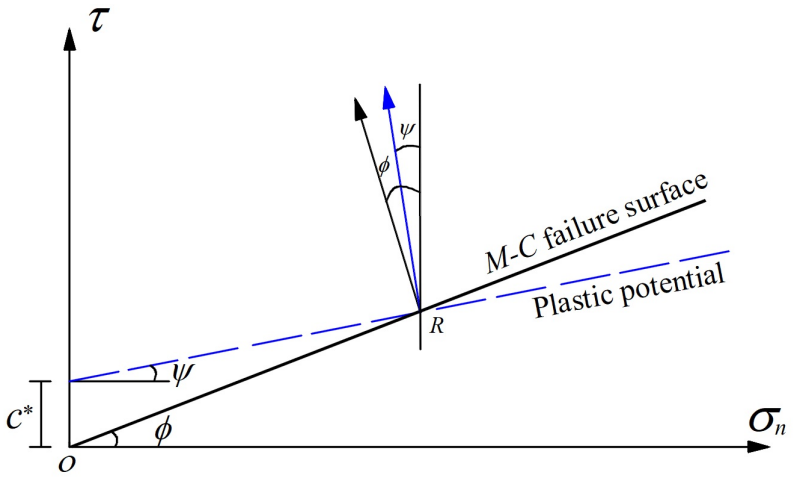

Figure 2.11: Stress state satisfying plastic potential surface and yield surface ($\psi > 0$).

2.9 Review of numerical procedures

2.9.1 The finite element method

There have been many numerical efforts to predict geotechnical stability, such as the finite difference method, the displacement finite-element method and finite-element limit analysis. Among different numerical tools, the displacement finite-element method is a common choice. However, the shortcomings of the displacement finite-element method (DFEM) cannot be ignored: (1) it costs significant computation time for a simulation of the load-deformation response (Sloan 2013, De Borst & Vermeer 1984); (2) multiple input variables for the constitutive model are needed. Compared to DFEM, finite-element limit analysis is a good alternative choice for many researchers since only a small number of variables are required for soil simulation and the error estimate can be assessed by comparing upper and lower bound solutions with each other.

The finite element limit analysis (FELA) uses an optimization technique to directly compute the upper or lower bound plastic collapse load. In terms of computation time, the computational efficiency of a FELA formulation is normally closely linked to that of its optimization algorithm. The FELA includes lower bound and up-

per bound analysis. Lysmer (1970) first applied finite elements and optimization theory to compute lower bounds for plane-strain geotechnical problems. Following Lysmer's seminal work, Anderheggen & Knöpfel (1972), Bottero et al. (1980) proposed various discrete methods for lower bound limit analysis based on linear triangles and linear programming. Sloan (1988) proposed a fast linear programming formulation that can solve small- to medium-scale 2D problems based on a novel active set algorithm. The method has been used successfully to predict the stability of geotechnical problems. By imposing non-linear yield conditions, Lyamin & Sloan (2002*a*) dramatically improved the practical utility of the discrete lower bound method by solving the resulting non-linear optimization problem. Anderheggen & Knöpfel (1972), Maier et al. (1972) proposed the formulations of the upper bound theory based on finite elements and linear programming. Then Sloan (1989) proposed an upper bound method based on the steepest-edge active set solution scheme, which had been proved successful for lower bound limit analysis. Then Lyamin & Sloan (2002*b*) developed an upper bound finite-element method that was also based on non-linear programming (NLP). NLP allows non-linear constraints to be included directly in the optimization, provided these constraints are differentiable everywhere. The Mohr-Coulomb yield function, however, cannot be handled directly as this is not differentiable at its apex. Instead, Lyamin & Sloan (2002*a*), Lyamin & Sloan (2002*b*) have used NLP with smoothed approximations to the two- and three-dimensional Mohr-Coulomb yield functions.

Except for the algorithms mentioned above, conic programming may be used to directly enforce the Mohr-Coulomb yield condition. For example, Makrodimopoulos & Martin (2007), Makrodimopoulos & Martin (2008), Krabbenhøft et al. (2007) have used efficient second-order cone programming (SOCP) to consider the two-dimensional Mohr-Coulomb yield condition. Krabbenhøft et al. (2008) have used semidefinite programming (SDP) to consider the three-dimensional Mohr-Coulomb yield condition. However, the failure surfaces used in limit analysis are generally non-linear, although these may be linearized to permit the problem to be solved us-

ing linear programming (LP). Alternatively, problems involving certain non-linear yield surfaces can be treated using efficient convex programming techniques (e.g. second order cone programming (Makrodimopoulos & Martin 2006)). Unfortunately, the solutions obtained using finite element limit analysis are often highly sensitive to the geometry of the original finite element mesh, particularly in the region of stress or velocity singularities.

In general, the use of finite element limit analysis suffers from two problems. Firstly, the accuracy of the solutions are found to be dependent on the mesh resolution. Secondly, numerical difficulties can be experienced as a result of volumetric locking and singularities. In an effort to overcome the potential issues arising from using the finite element methods, (e.g. discretization, singularities, volumetric locking, numerical instability and mesh refinement), an alternative formulation may be used. The procedure will be introduced in the following section.

2.9.2 Discontinuity layout optimization - DLO

Discontinuity layout optimization (DLO) was first introduced by Smith & Gilbert (2007). During the process of layout optimization, closely spaced nodes are distributed across the problem domain, and numerous potentially active discontinuities connecting related nodes are added to the problem. The DLO procedure is formulated as a linear programming (LP) problem that identifies the optimal subset of discontinuities that produces a compatible mechanism with the lowest energy dissipation.

Compared with other numerical tools, i.e. finite element limit analysis, some advantages of DLO procedure are: (1) the procedure is able to overcome volumetric locking and stress/velocity singularity; (2) the inputs parameters are simple and easily understood; (3) the results can easily be checked (using a force and/or velocity diagram). A detailed description of the development of the numerical formulation of DLO will be demonstrated in the following chapters.

2.10 Review of the previous work

This thesis is dedicated to the application of the limit analysis approach to assess the stability of the geotechnical structures with non-linear or non-associative yield conditions. There are many literatures covering the stability analysis using non-linear yield condition and the non-associative analysis of toppling-sliding block problems. A brief overview will be made in the following.

2.10.1 Failure analysis with use of non-linear yield function

Many researchers have used different approaches to explore the influence of non-linearity on the stability of geotechnical problems. By use of variational calculus, Baker & Frydman (1983) derived the governing equations for the bearing capacity of a strip footing on the surface of a slope. However, except in very special cases, it is not possible to derive an explicit solution for a system of non-linear differential equations. By considering a general non-linear failure criterion for soils, Zhang & Chen (1987) proposed a novel numerical procedure by converting the complex differential equations into an initial value problem. This inverse method is used to solve the slope stability problem. To simplify the solution procedure by inverse method, Drescher & Christopoulos (1988) proposed an alternative limit analysis method with 'tangential' line technique to evaluate the stability factors of an infinite and homogenous slope. The calculated stability factors are upper bound solutions to those of Zhang & Chen (1987) and the differences are very small. It has been demonstrated that the limit analysis-based minimizing tangent criterion (MTC) approach suggested by Drescher & Christopoulos (1988) provides a sound and rigorous way of solving non-linear problem, however, MTC requires employing a proper minimization scheme to detect the global minimum for some problems, i.e. passive earth pressure. In order to simplify this procedure, Soon & Drescher (2007) presented an approach based on the classic multi-wedge rigid block upper bound kinematic method, using straight slip-lines and a specific linear yield surface

for each sliding interface, where this linear surface was selected as a tangent to the non-linear yield surface, shown in Figure 2.12. The specific tangent location was chosen as part of a multivariable optimization across all slip-lines. The advantage of the 'tangential' technique is that the non-linear failure analysis can be linearized and it is easy to calculate the energy dissipation compared with the method which uses the non-linear failure criterion directly. Different from the linear analysis which doesn't need to consider the stress distribution along the failure surface, the general non-linear analysis should include the stress distribution along the slip surface for the calculation of the energy dissipation (Zhang & Chen 1987). However the normal stress distribution based on the non-linear failure slip-line is difficult to be obtained for the calculation of the internal energy dissipation. Different from multi-wedge rigid block upper bound kinematic method (by Soon & Drescher (2007)) which assumes that the tangent representing each linear surface is different from each other, a 'generalized tangential technique' is proposed to compute seismic active earth pressures (Yang 2007). This 'generalized tangential technique' allows for the calculation of the external and internal work using a unique tangent (a linear Mohr-Coulomb yield criterion) instead of non-linear failure criterion. This method assumes that the friction angle and interception are unchangeable along the entire slip surface both in translational and rotational fracture failure mechanisms of active smooth retaining wall problem. With help of a non-linear sequential quadratic programming algorithm, the maximum active earth pressure problem could be solved by the 'generalized tangential technique' (Yang 2007). For translational mode, there are only two variables (the angle of the sliding plane to the vertical and friction angle of the chosen tangent); for rotational mechanism, there are only three variables (two geometry parameters of failure slip-line and tangential line angle), which simplifies the optimization process. However, this method is only applicable for one-wedge upper bound kinematic analysis. And the failure mechanisms used by Yang (2007) are pre-defined with referring to the classic linear translational mechanism and the linear analysis based log-spiral rotational

mechanism, which are not rigorous non-linear failure slip-lines. This non-linear optimization procedure is verified by the semi-analytical expression proposed by Yang (2007), which is based on the effective stress analysis using Mohr's circles. The results obtained from the 'generalized tangential technique' are also validated by the non-linear optimization method based on the normal stress distribution function along the failure surface in soil obeying general non-linear failure criterion within the framework of limit equilibrium (Sun & Song 2016). The normal stress distribution function is derived from the method of characteristic and the calculation procedure could be summarized shown in Figure 2.13. The limitation of this method is the failure surface should be assumed in advance and the kinematic constraints are not satisfied rigorously since it follows the limit equilibrium theory.

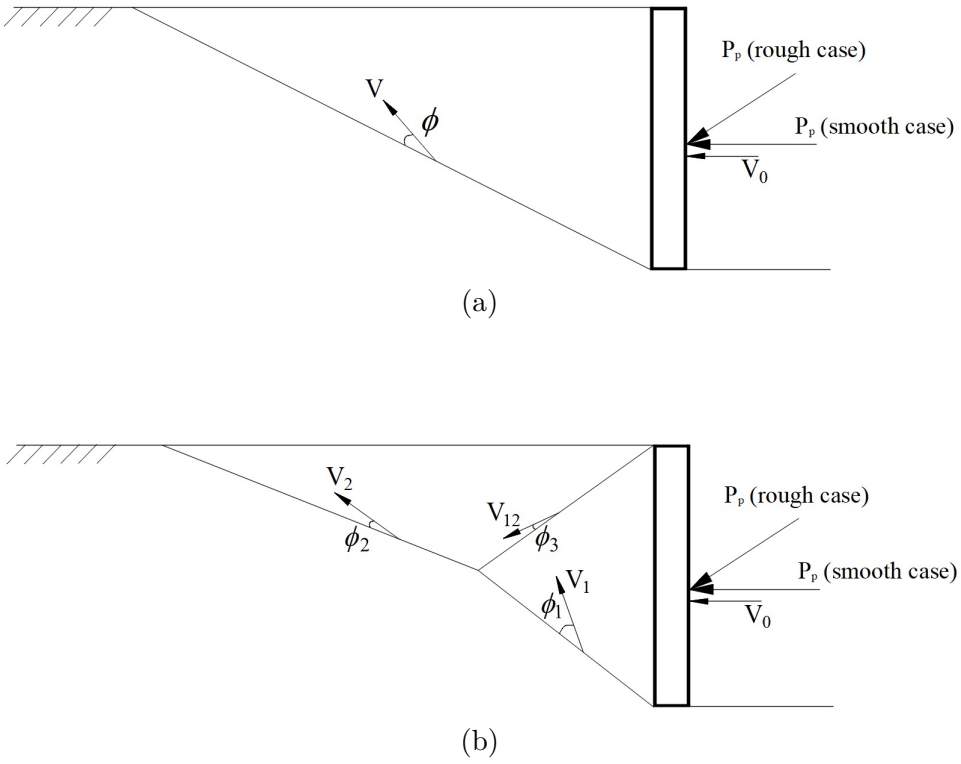

Figure 2.12: Multi-wedge rigid block analysis for passive earth pressure problem: (a) one-block failure mechanism; (b) two-block failure mechanism (after Soon & Drescher (2007)).

The non-linear Hoek-Brown (HB) failure criterion is often used to describe the strength of different types of rocks. Collins et al. (1988) applied the minimizing

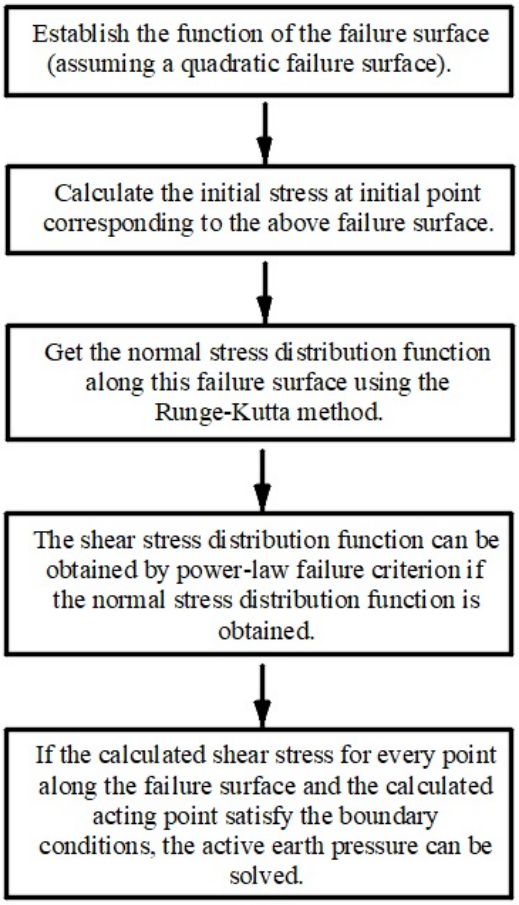

Figure 2.13: The procedure for calculation of the active earth pressure (after Sun & Song (2016)).

tangent criterion (MTC) technique to assess the stability of an infinite and homogenous slope with the Hoek-Brown yield rule, and the slope stability factors are presented for different kinds of rocks with back analysis. With help of the Hoek-Brown yield rule, the 'generalized tangential technique' is extended to assess the stability of slopes (Yang et al. 2004) and the bearing capacity of foundations (Yang & Yin 2005). As an alternative approach, other scholars (e.g. Fraldi & Guarracino 2009, Yang & Huang 2011 and Yang & Long 2015) used a variational approach to analyse the stability of anchors, trapdoors and tunnels with a single curved slip-line, defined by a closed form equation, that obeys the non-linear Hoek-Brown yield function flow rule along its full length. However, these analyses were restricted to single wedges constrained to move vertically and to the author's knowledge this

approach has not been extended to a wider range of problems.

2.10.2 Toppling-sliding block problems

It is well understood that the stability of a rock slope is controlled by discontinuities or joints existing in the rock mass. Toppling-sliding failure often exists in flatter slopes or in large scale slopes, where toppling columns force the rock near the toe of the slope to fail by sliding or shearing through intact material. Compared with a pure sliding failure which occurs when the geological structure dips out of the face, toppling failure often involves rotation of jointed columns about pivot points. Pure toppling failure only occurs in very steep of overhanging slopes. Studies of toppling failure were initiated in the late 1960s and early 1970s using physical models, e.g. Ashby (1971). Subsequently various workers have identified the toppling-sliding mechanism in failures observed in the field (De Freitas & Watters 1973).

Many different numerical models have been put forward in the past decades: (1) finite element method (FEM) (Goodman et al. 1968); (2) boundary element method (BEM) (Crotty & Wardle 1985); (3) discontinuous deformation analysis (DDA) (Shi 1992); (4) Ishida et al. (1987), Lanaro et al. (1997), Meng et al. (2018) and Sarfaraz & Amini (2019) have used the distinct element numerical method (DEM) to model the toppling failure process.

On the basis of the theoretical fundamentals of block toppling problems proposed by Goodman & Bray (1976), other approaches have been proposed to conduct toppling-sliding failure analysis including limit equilibrium and limit analysis approaches. Due to its simplicity, the limit equilibrium procedure has been used by many researchers, e.g. Wyllie (1980), Lanaro et al. (1997), Zanbak (1983), Adhikary et al. (1997), Sagaseta et al. (2001) and Jiang & Zhou (2017). Based on equilibrium theory, Zhang et al. (2018) put forward a new calculation method for

the stability of rock slopes subject to three-step flexural toppling failure. By this new method, analyses of the effects of different factors on stability factors are conducted and the method shows a potential to calculate the stability for the real case. With considering the rigorous kinematic constraints, some researchers used limit analysis based approaches to conduct the toppling failure analysis of rigid block problem. Babiker et al. (2014) proposed a modified plastic limit analysis procedure incorporating a non-associative, low dilation, friction model. The proposed non-associative iterative method (short for NAIM) adopts the same assumption as that in this thesis: the yield surface and potential function are separate and the intersection follows the non-associative flow rule and the yield surface. In order to find the normal force on this intersection, a number of iterations may be required before a converged solution is reached, as shown in Figure 2.14. Each iterative process could be taken as an independent associative procedure (Babiker et al. 2014). Firstly, by solving the problem assuming associative flow, the initial normal $N_{i,0}$ and shear $S_{i,0}$ forces can be extracted from the solution for each joint i. At the next iteration k the modified shear strength parameter $C_{i,k}$ for joint i can be computed using the normal force from the previous iteration $N_{i,k-1}$ to multiply $\tan\phi$ (ϕ is the actual material angle of friction of the yield surface). The new values of $N_{i,k}$ and $S_{i,k}$ can be obtained by solving the associative problem, which obeys the modified yield surface using the parameter $C_{i,k}$. When the difference between $N_{i,k}$ and $N_{i,k-1}$ is smaller than the pre-defined tolerance, the iterative algorithm stops. This method provides a range of feasible solutions instead of a unique solution on the basis of the non-associative flow rule. However using this computational limit analysis procedure, the risk of non-convergence could not be avoided during the iterative process and different LP solvers may generate non-consistent results, which limits this procedure as a method for producing NA solutions.

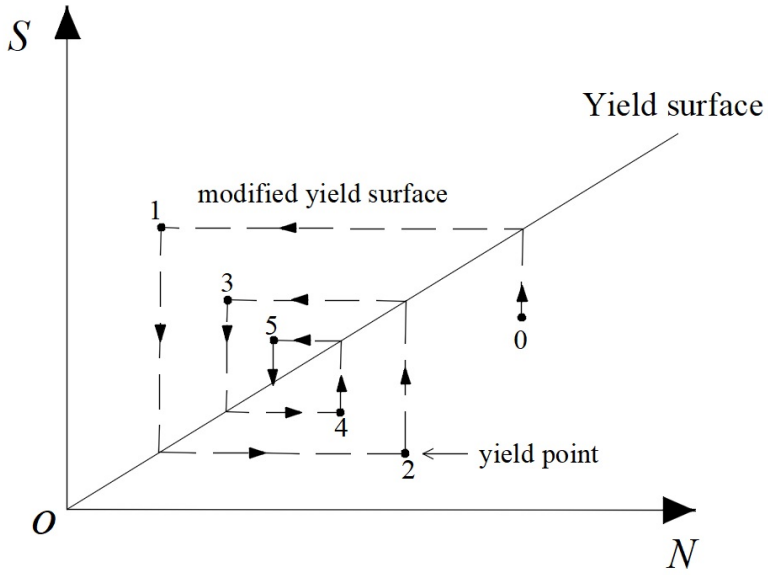

Figure 2.14: Variable normal force at joint for multiple iterations (after Babiker et al. (2014)).

2.11 Conclusions

In this chapter, the important fundamental concepts related to this research are introduced and the state-of-the-art of the published literature in this research field is given. A summary and outline of the conclusions are shown below:

1. Limit analysis is a good choice to estimate the stability of geotechnical problems (ULS) and is more rigorous than the limit equilibrium method.

2. The bound theorems of limit analysis are particularly useful if both upper and lower bound solutions can be calculated because the true collapse load can then be bracketed from above and below.

3. The Mohr-Coulomb criterion has been widely used in soil mechanics, but it has been observed that the yield envelopes of many soils are not linear.

4. Among different non-linear yield functions, a power-law yield rule is widely used in limit analysis. Many different classical non-linear soils and rocks in textbook can be represented by a power-law form.

5. For frictional soils, the assumption of non-associative flow rule is expected to provide a range of feasible solutions instead of a unique solution, which is more realistic. To model non-associative behaviour, the interaction between a yield function and a potential function has been introduced. The case where the yield surface intersects the plastic potential can be taken as underlying principles for the proposed non-associative methods in this thesis.

6. There have been many attempts to formulate the limit analysis approach using the finite element method. However, the accuracy of the solutions were found to be dependent on the mesh resolution and the singularities cannot be avoided. As an alternative choice, DLO procedure can overcome some of these issues.

Chapter 3

Discontinuity based numerical limit analysis

3.1 Introduction

The purpose of this chapter is to introduce the basic formulation of discontinuity based numerical limit analysis applied in continuum problems, DLO (Discontinuity layout optimization), and the variant for solving rigid block problems. This chapter also describes a non-linear method based on DLO that approximates a power-law non-linear failure surface using several linear yield surfaces (in Mohr-Coulomb form) which are tangential to the non-linear failure surface. This includes a methodology to determine the optimal locations of multiple tangency points.

3.2 Formulation of DLO

The DLO procedure is an upper bound method that uses numerical optimisation to identify a critical collapse mechanism. The basic stages of the DLO procedure are demonstrated in Figure 3.1. Different from other available numerical procedures which use fixed size elements to discretize the relevant problem domain, the DLO problem is discretized in terms of potential discontinuities connected by defined

nodes. Increased accuracy can be obtained by increasing the nodal density.

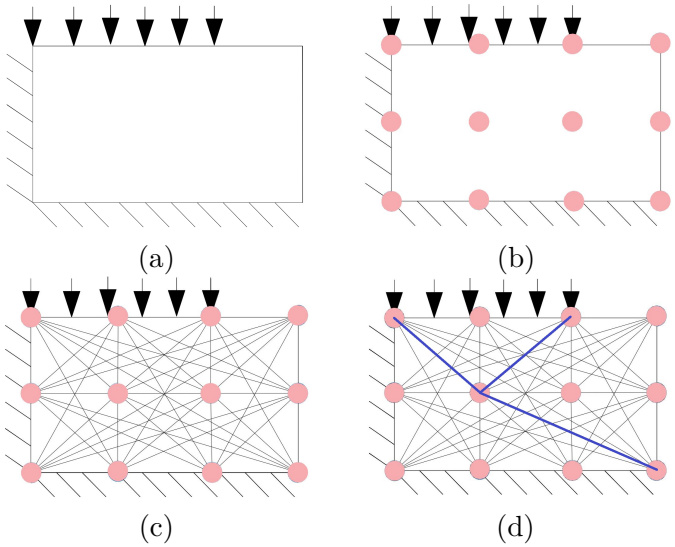

Figure 3.1: Stages in DLO procedure: (a) starting problem (surcharge applied to block of soil close to a vertical cut); (b) discretization of soil using nodes; (c) interconnection of nodes with potential discontinuities; (d) identification of critical subset of potential discontinuities using optimization (after Smith & Gilbert (2007)).

3.2.1 The kinematic problem formulation

The DLO procedure can be formulated in a kinematic or equilibrium form. In the kinematic formulation, the objective function seeks to minimize the energy dissipated at failure state. Analogous to the equilibrium conditions in optimum trusses problems, the compatibility condition is considered and enforced locally at the nodes. In order to follow the associative flow rule, the case of Mohr-Coulomb (or Tresca) yield surface is used in the flow rule matrix in a basic DLO formulation.

$$\min \lambda \mathbf{f}_{\mathrm{L}}^{T}\mathbf{d} = -\mathbf{f}_{\mathrm{D}}^{T}\mathbf{d} + \mathbf{g}^{T}\mathbf{p} \tag{3.1}$$

subject to:

$$\mathbf{Bd} = 0 \tag{3.2}$$

$$\mathbf{Np} - \mathbf{d} = 0 \tag{3.3}$$

$$\mathbf{f}_{\mathrm{L}}^{T}\mathbf{d} = 1 \tag{3.4}$$

$$\mathbf{p} \geq \mathbf{0} \tag{3.5}$$

where λ is the load multiplier at collapse, $\mathbf{f}_{\mathrm{D}}$ and $\mathbf{f}_{\mathrm{L}}$ are vectors containing respectively specified dead and live loads. The objective is thus to minimize the objective function whilst ensuring that the yield condition is not violated along any discontinuity $i = 1, ...c..$ $\mathbf{B}$ is compatibility matrix, $\mathbf{N}$ is a matrix defining the flow rule, $\mathbf{p}$ is a vector of plastic multipliers and $\mathbf{g}$ is a vector containing dissipation coefficients. In the kinematic formulation, the vector $\mathbf{g}^T = \{c_1 l_1,\ c_2 l_2,\ ...\ \ c_m l_m\}$ is intercept matrix, where c_i and l_i are, respectively, the cohesive shear strength and the length of discontinuity i. Thus matrix $\mathbf{d}^T = \{s_1, n_1, s_2, ...n_m\}$; where s_i and n_i are the relative shear and normal displacement rates across discontinuity i $(i = 1...c)$.

3.2.2 Compatibility

In order to enforce the compatibility at the nodes, the LP variables n_i, s_i should be constrained in compatibility matrix. The details of its extension to cohesive-frictional or more complex yield criteria are illustrated by Smith & Gilbert (2007).

To transform the local nodal compatibility to the global problem matrix, the compatibility constraint for discontinuity i can be expressed as:

$$\mathbf{B}_i\ \mathbf{d}_i = \begin{bmatrix} \alpha_i & -\beta_i \\ \beta_i & \alpha_i \\ -\alpha_i & \beta_i \\ -\beta_i & -\alpha_i \end{bmatrix} \begin{bmatrix} s_i \\ n_i \end{bmatrix} \quad (3.6)$$

where α_i and β_i represent the directional factors for the velocities in the x-axis and y-axis direction at discontinuity i.

3.2.3 Flow rule

The flow rule is enforced by introducing the following constraint:

$$\mathbf{N}_i\ \mathbf{p}_i - \mathbf{d}_i = \begin{bmatrix} 1 & -1 \\ \tan\phi_i & \tan\phi_i \end{bmatrix} \begin{bmatrix} p_i^1 \\ p_i^2 \end{bmatrix} - \begin{bmatrix} s_i \\ n_i \end{bmatrix} = 0 \quad (3.7)$$

where $\mathbf{N}_i$ is the flow rule along the discontinuity i, $\mathbf{p}_i$ is a vector of the plastic multipliers p_i^1,p_i^2. The plastic multipliers guarantee the work done and energy dissipated is always positive. They are governed by the condition that they should not take negative values, p_i^1,$p_i^2 \geq 0$. The shear and normal velocity along the discontinuity (vector $\mathbf{d}$) and the plastic multipliers in (vector $\mathbf{p}$) are the variables in the optimization problem.

3.2.4 The dual equilibrium formulation

Duality principles can be used to derive the dual of the kinematic formulation above (Smith & Gilbert 2007), which is an equilibrium formulation. Thus a planar body

discretized using m nodal connections (slip-line discontinuities) and n nodes this may be stated as follows:

$$\max \lambda \tag{3.8}$$

subject to:

$$\mathbf{B}^T\mathbf{t} + \lambda\mathbf{f}_\mathrm{L} - \mathbf{q} = -\mathbf{f}_\mathrm{D} \tag{3.9}$$

$$\mathbf{N}^T\mathbf{q} \leq \mathbf{g} \tag{3.10}$$

where $\mathbf{t}^T = \{t_1^x,\ t_1^y,\ t_2^x,\ t_2^y\ ...\ \ t_n^y\}$ and t_j^x and t_j^y can be interpreted as x and y direction equivalent nodal forces acting at node $j(j = 1, ..., n)$, corresponding in a work sense to u_j^x and u_j^y, respectively; and $\mathbf{q}$ is a vector of shear and normal forces acting on discontinuities. Therefore, the LP variables are t_j^x, t_j^y, the shear force, the normal force and the live load factor λ. The objective is thus to maximize λ while ensuring that the yield condition is not violated along any potential discontinuity.

3.2.5 Extension to model rotational failure using DLO formulation

The formulation introduced above is used to identify mechanisms that are purely translational using plane-strain DLO. Extended by the basic DLO formulation above, a more general formulation has been developed to identify mechanisms that can involve arbitrary rotations and/or translations in cohesive media (Smith & Gilbert 2013). Considering the more complicated cases involving confined geometries, where curved slip-lines could potentially intersect boundaries, the improved method

including kinematic and equilibrium formulations has been proposed (Smith & Gilbert 2015).

3.3 Non-linear analysis in DLO with multi-tangent technique

In this section, a multi-tangent technique is developed to conduct non-linear analysis of geotechnical problems within the framework of the numerical procedure DLO (Discontinuity Layout Optimization), by using the upper bound theorem of limit analysis in conjunction with the non-linear failure criterion. The proposed approach can be used to validate results from the methods developed in the following chapters.

3.3.1 Single tangential line analysis

The implementation of DLO within the software LimitState:GEO Version 3.2e is used in this thesis. This allows the use of multiple tangents to enclose the non-linear yield surface. One tangential line to the curve at the location of tangency point M as shown in Figure 3.2 can be expressed as

$$\tau = c_t + \sigma_n \tan \phi_t \tag{3.11}$$

where ϕ_t and c_t are tangential frictional angle and intercept of the straight line on the τ-axis. σ_n and τ are normal and shear stresses, respectively. The c_t and ϕ_t at point M are determined by the following two expressions:

$$\tan \phi_t = \frac{d\tau}{d\sigma_n} = \frac{1}{m\sigma_t} c_0 (a + \frac{\sigma_M}{\sigma_t})^{(1-m)/m} \tag{3.12}$$

$$c_t = \frac{m-1}{m} c_0 (\frac{m\sigma_t \tan \phi_t}{c_0})^{1/(1-m)} + a \cdot \sigma_t \tan \phi_t \tag{3.13}$$

For simplicity, curved power-law yield surface is defined by combinations of linear surfaces (expressed by different tangential lines) in this study. The shear strength function of linear materials (expressed by Mohr-Coulomb failure criterion) can be obtained by the proposed single tangential line analysis. In Eq. 3.12, the stress σ_M is the value of normal stress at the tangency point M as shown in Figure 3.2. The schematic diagram of two-tangent line mode and three-tangent line mode are shown in Figure 3.3 and Figure 3.4.

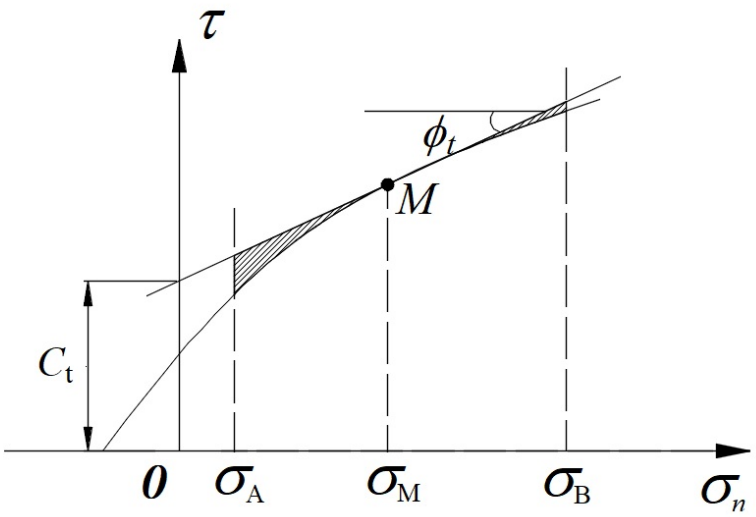

Figure 3.2: Tangential line for a non-linear failure criterion.

3.3.2 Optimum locations of tangents

The actual optimum locations of tangents will be specific and complex to determine. In this thesis the best fit tangent to the original curve will be considered assuming a uniform distribution of normal stresses within the system to be modelled. Since the yield surface is convex and smooth, the tangential line at any point of the strength curve always lies outside of the curve, and the strength corresponding to the tangential line is more than or equal to that of the corresponding non-linear curve. In the coordinate axis system the area between the tangential lines and σ_n-axis is bigger than that between the strength curve and σ_n-axis over any intervals.

The search for the optimum location of the tangency point can be approximately represented by the search for the minimum area between a set of tangential lines and the exponential strength curve. The 'Minimum area' technique is illustrated below.

A convex and smooth yield surface may be represented by several tangential lines which lie outside of the curve. On the assumption that the normal stresses are uniformly distributed within a given interval, the optimum location of the tangential point can be regarded as a search for the minimum area between a set of tangential lines and the exponential strength curve.

The search for the optimum solution procedure involves a number of steps:

1. The area between the tangential line and the σ_n-axis in the specified interval should be calculated first.
2. The area between the strength curve and σ_n-axis in the same intervals should then be calculated.
3. The minimum area difference can be obtained by an optimization procedure, allowing the optimal location of the tangential point to be set.

For the 1-line mode, as shown in Figure 3.2, the shear stress values at points A and B can be expressed as follows:

$$\tau_A = c_t + \sigma_A \tan \phi_t \tag{3.14}$$

$$\tau_B = c_t + \sigma_B \tan \phi_t \tag{3.15}$$

The area contained by the tangential line and σ_n-axis between interval $[\sigma_A\ ,\ \sigma_B]$ is,

$$S_T = \frac{1}{2}(\tau_A + \tau_B) \cdot\ (\sigma_B - \sigma_A) \tag{3.16}$$

The area contained by curves and σ_n-axis between interval $[\sigma_A\ ,\ \sigma_B]$ is,

$$S_C = \int_{\sigma_A}^{\sigma_B} c_0(a + \sigma_n/\sigma_t)^{1/m} d\sigma_n \tag{3.17}$$

We search for the minimum of the objective function S

$$S = S_T - S_C \tag{3.18}$$

Because the area between the curve and the σ_n-axis in the interval $[\sigma_A, \sigma_B]$ is only determined by the values of σ_A and σ_B, the search for the minimum area difference can be simplified to the search for the optimum value of S_T. Moreover the term $(\sigma_B - \sigma_A)/2$ also cannot affect the optimum result, so the aim of the work is to seek for the optimum value of $(\tau_A+\tau_B)$,

Based on Eq. 3.14 and Eq. 3.15,

$$\Lambda\ = (\tau_A + \tau_B) = 2c_t + (\sigma_A + \sigma_B)\tan\phi_t \tag{3.19}$$

According to the analysis for single tangent,

$$\begin{aligned}\Lambda\ &= (\tau_A + \tau_B) = 2[\frac{m-1}{m}c_0(\frac{m\sigma_t \tan\phi_t}{c_0})^{1/(1-m)} + a\cdot\sigma_t\tan\phi_t] + (\sigma_A + \sigma_B)\tan\phi_t \\ &= 2\frac{m-1}{m}c_0(a + \sigma_M/\sigma_t)^{1/m} + (2a\cdot\sigma_t + \sigma_A + \sigma_B)\frac{c_0}{m\sigma_t}(a + \sigma_M/\sigma_t)^{(1-m)/m}\end{aligned} \tag{3.20}$$

In order to find the extremum of the objective function Λ, $\partial\Lambda/\partial\sigma_M$ should be zero,

$$\frac{\partial\Lambda}{\partial\sigma_M} = 2 - (2a + (\sigma_A + \sigma_B)/\sigma_t)(a + \sigma_M/\sigma_t)^{-1} = 0 \tag{3.21}$$

The optimum value of σ_M should be $(\sigma_A + \sigma_B)/2$.

We can conclude that the optimum tangency point always occurs at the mid-point of the segment. Theoretically, the two endpoints σ_A , σ_B are determined by the minimum and maximum stresses in the assumed uniform normal stresses distribution system.

If the uniform normal stresses distribution system could be predicted for some specific problems, the two endpoints of the feasible normal stress range could be taken as the minimum and maximum stresses.

For 2-line, as shown in Figure 3.3, the shear stress values of the first tangent (tangency point is M_1) and the second tangent (tangency point is M_2) can be expressed

$$\tau_1 = c_{t1} + \sigma_n \tan \phi_{t1} \tag{3.22}$$

$$\tau_2 = c_{t2} + \sigma_n \tan \phi_{t2} \tag{3.23}$$

Let $\tau_1 = \tau_2$, the σ_n-height of intersection of two tangential lines σ_C can be obtained,

$$\sigma_C = \frac{c_{t1} - c_{t2}}{\tan \phi_{t2} - \tan \phi_{t1}} \tag{3.24}$$

Area bounded by the first tangential line and σ_n-axial between interval $[\sigma_D$, $\sigma_C]$ is,

$$S_{T1} = \frac{1}{2}[2c_{t1} + \tan \phi_{t1}(\sigma_D + \sigma_C)] \cdot \ (\sigma_C - \sigma_D) \tag{3.25}$$

Area bounded by the second tangential line and σ_n-axial between interval $[\sigma_C$, $\sigma_E]$ is,

$$S_{T2} = \frac{1}{2}[2c_{t2} + \tan \phi_{t2}(\sigma_C + \sigma_E)] \cdot \ (\sigma_E - \sigma_C) \tag{3.26}$$

Area bounded by curves and σ_n-axial between interval $[\sigma_D\ ,\ \sigma_E]$ is,

$$S'_C = \int_{\sigma_D}^{\sigma_E} c_0(a + \sigma_n/\sigma_t)^{1/m} d\sigma_n \tag{3.27}$$

Search for the minimum of objective function S with condition $\sigma_D < \sigma_E$, $\sigma_{M1} < \sigma_{M2}$,

$$S = S_{T1} + S_{T2} - S'_C \tag{3.28}$$

Seeking for the minimum value of S consisting of $S_{T1} = (\tau_D + \tau_C)(\sigma_C - \sigma_D)/2$ and $S_{T2} = (\tau_E + \tau_C)(\sigma_E - \sigma_C)/2$ can be converted into seeking for the minimum values of S_{T1} and S_{T2} synchronously. By use of the demonstration of one-line mode, it could be concluded that the optimum values of σ_{M1} and σ_{M2} should be $(\sigma_C + \sigma_D)/2$ and $(\sigma_C + \sigma_E)/2$, respectively.

Then, $\sigma_{M2} - \sigma_{M1} = (\sigma_E - \sigma_D)/2$ can be easily obtained. We can conclude that the gap between two optimum tangency points always equals the half of the internal length. The two endpoints $\sigma_D\ ,\ \sigma_E$ are determined by the minimum and maximum normal stresses. The optimum value of σ_{M1} should be in the range $[\sigma_D, (\sigma_D + \sigma_E)/2]$ and the optimum value of σ_{M2} should be in the range $[(\sigma_D + \sigma_E)/2, \sigma_E]$. In order to determine the optimal value of σ_{M1} for producing the minimum value of the limit load, (take passive earth pressure as an example, the details are illustrated in Section 3.3.3) a graph should be plotted, as shown in Figure 3.5.

3.3.3 Application for soils obeying non-linear failure criterion

In order to verify the proposed multi-tangent non-linear method implemented in the platform of DLO procedure (the LimitState: GEO software is used and the nodal density adopts 2000 nodes), an example for passive smooth retaining wall problem (wall height $H = 5$ m and $q = 0$) is conducted to show how the calculated passive

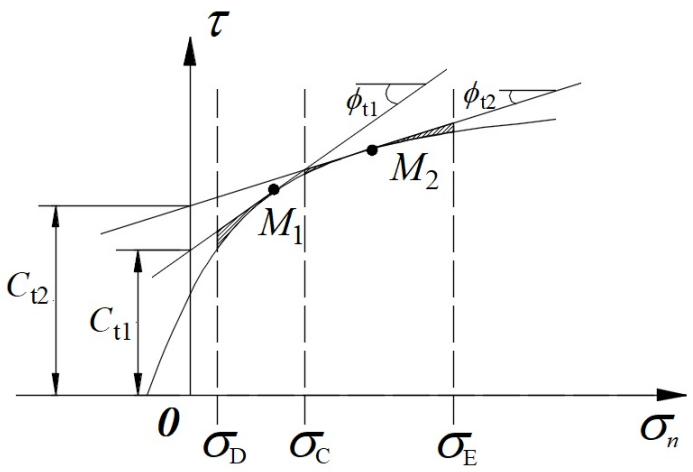

Figure 3.3: Two-tangent line mode for simplifying curve of strength function.

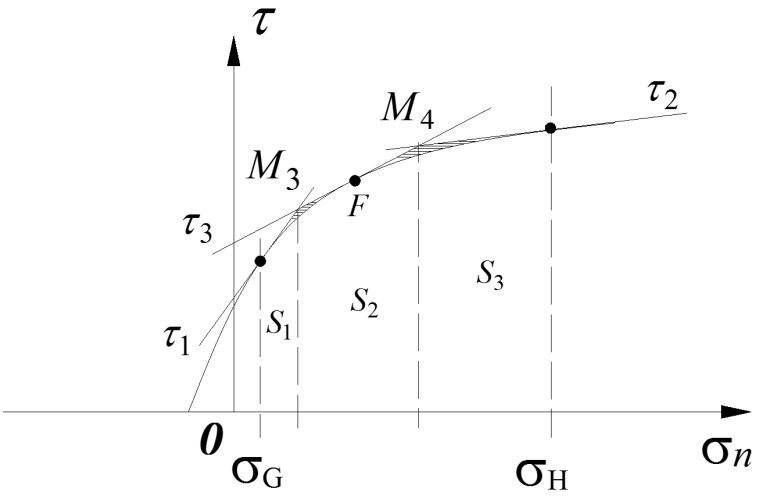

Figure 3.4: Three-tangent line mode for simplifying curve of strength function.

earth pressure varies with the change of the number of the tangents. For the multi-tangent technique, the normal stress distribution should be determined first. In this section, a straightforward way for determining the maximum and minimum normal stresses is adopted. For the passive smooth retaining wall analysis, a vertical stress distribution is found uniform and the minimum and maximum vertical stresses could be determined easily. For simplicity, $\sigma_A = q$ (minimum vertical stress) and $\sigma_B = q + \gamma H$ (maximum vertical stress) can be taken as minimum and maximum normal stresses, respectively. As shown in Table 3.1, the calculated earth pressures in dense sand case (the values of parameters in power-law failure criterion are

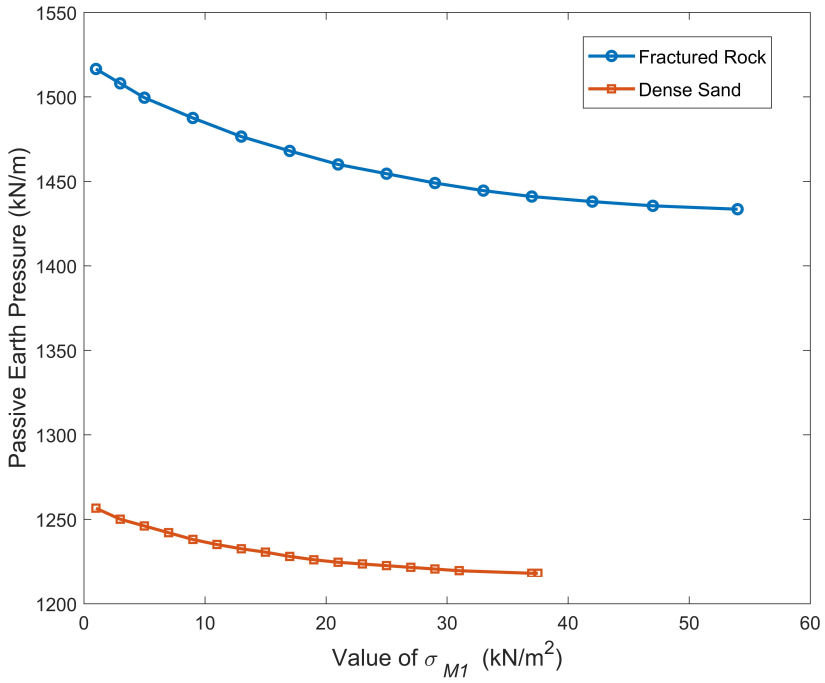

Figure 3.5: Passive earth pressure with varying value of σ_{M1}.

determined in Section 2.7) are illustrated and the optimal tangent points are shown in Table 3.2. For fractured rock case (the values of parameters in power-law failure criterion are determined in Section 2.7), the passive earth pressures with varying number of the tangents are shown in Table 3.3 and the optimal tangent points are shown in Table 3.4. When the number of tangents is bigger than two, the determination of the optimum locations of tangents is illustrated in **Appendix. A**.

From Table 3.1 and Table 3.3, it could be concluded that the limit load decreases with the increase of the number of the tangents. And the difference between the 2-tangent solution and 3-tangent solution is small, the optimal 2-tangent solution shows the optimal locations of tangency points are at the middle point and end point of the interval $[\sigma_D, \sigma_E]$ in both two cases, shown in Figure 3.5. The 'Minimum area' also provides an empirical method to determine the optimal locations of multiple tangents when the number of tangents is bigger than 2, shown in **Appendix. A**. The optimal 2-tangent solution should be determined by comparing

different solutions at different tangency points rigorously, which is time-consuming. To save the computation time, the empirical solution for 3-tangent mode can be considered. It could be concluded that there are no obvious gaps between the 3-tangent solution and 4-tangent solution for both cases. As we know, the more tangents are chosen, the more time will take for computation. Therefore, the 3-tangent solution is a better choice for the proposed multi-tangent technique applied for the passive retaining wall analysis in this chapter. The predicted passive retaining wall failure mechanisms for two cases in 3-tangent mode are shown in Figure 3.6 and Figure 3.7. However, for some cases, more tangents are needed to get more accurate results after comparisons using different number of tangents.

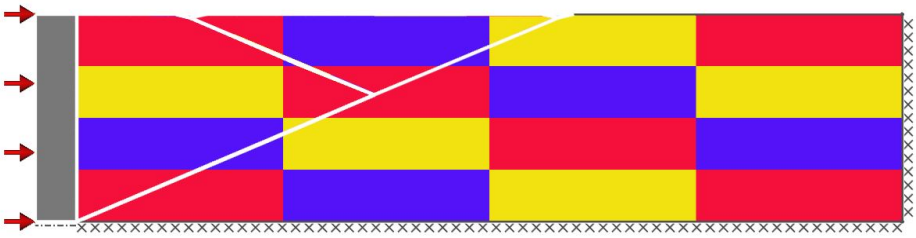

Figure 3.6: Failure mechanism prediction of smooth retaining wall problem by three-tangential line DLO method: dense sand case ($a = 0$, $c_0 = 1.697\text{kN/m}^2$, $\sigma_t = 1\text{kN/m}^2$, $m = 1.1182$, $\gamma = 15\text{kN/m}^3$).

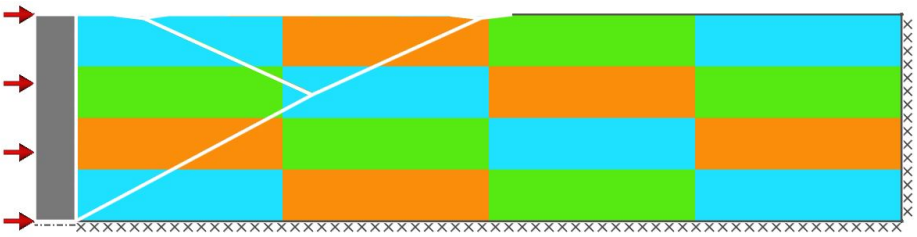

Figure 3.7: Failure mechanism prediction of smooth retaining wall problem by three-tangential line DLO method: fractured rock case ($a = 0$, $c_0 = 1.8242 \times 10^3\text{kN/m}^2$, $\sigma_t = 5 \times 10^3\text{kN/m}^2$, $m = 1.3155$, $\gamma = 22\text{kN/m}^3$).

3.4 Modelling rigid block problems

In order to predict the collapse load for a rigid block assembly for two and three dimensional structures, Livesley (1978) proposed a linear programming numerical

n	Passive earth pressure value (kN/m)	reduction (%)
1	1260.5	
2	1218	3.49
3	1216.5	0.12
4	1213.5	0.25
5	1213	0.04

Table 3.1: Passive earth pressure values versus number of tangents n: dense sand case.

Tangent number	Parameter sets
1	$c_t = 4.5859$kPa,$\phi_t = 45.9747°$
2	$c_t = 4.5859$kPa,$\phi_t = 45.9747°$ $c_t = 8.5239$kPa,$\phi_t = 43.8761°$
3	$c_t = 0.0229$kPa,$\phi_t = 62.6803°$ $c_t = 4.5859$kPa,$\phi_t = 45.9747°$ $c_t = 8.5239$kPa,$\phi_t = 43.8761°$
4	$c_t = 0.0229$kPa,$\phi_t = 62.6803°$ $c_t = 2.4967$kPa,$\phi_t = 48.0281°$ $c_t = 6.6165$kPa,$\phi_t = 44.7336°$ $c_t = 8.5239$kPa,$\phi_t = 43.8761°$
5	$c_t = 0.0229$kPa,$\phi_t = 62.6803°$ $c_t = 2.4673$kPa,$\phi_t = 48.0680°$ $c_t = 4.5859$kPa,$\phi_t = 45.9747°$ $c_t = 6.5903$kPa,$\phi_t = 44.7470°$ $c_t = 8.5239$kPa,$\phi_t = 43.8761°$

Table 3.2: The optimal locations of tangent points in the analysis in Table 3.1.

n	Passive earth pressure value (kN/m)	reduction (%)
1	1524	
2	1433	6.35
3	1433	0
4	1425	0.56
5	1424	0.07

Table 3.3: Passive earth pressure values versus number of tangents n: fractured rock case.

Tangent number	Parameter sets
1	$c_t = 14.1942$kPa,$\phi_t = 39.2829°$
2	$c_t = 14.1942$kPa,$\phi_t = 39.2829°$ $c_t = 24.0406$kPa,$\phi_t = 34.7108°$
3	$c_t = 0.1172$kPa,$\phi_t = 74.9349°$ $c_t = 14.1942$kPa,$\phi_t = 39.2829°$ $c_t = 24.0406$kPa,$\phi_t = 34.7108°$
4	$c_t = 0.1172$kPa,$\phi_t = 74.9349°$ $c_t = 5.8142$kPa,$\phi_t = 47.3091°$ $c_t = 17.4192$kPa,$\phi_t = 37.4819°$ $c_t = 24.0406$kPa,$\phi_t = 34.7108°$
5	$c_t = 0.1172$kPa,$\phi_t = 74.9349°$ $c_t = 8.3807$kPa,$\phi_t = 44.0072°$ $c_t = 14.1942$kPa,$\phi_t = 39.2829°$ $c_t = 19.3184$kPa,$\phi_t = 36.5826°$ $c_t = 24.0406$kPa,$\phi_t = 34.7108°$

Table 3.4: The optimal locations of tangent points in the analysis in Table 3.3.

method. On the basis of this approach, Gilbert & Melbourne (1994) put forward basic associative limit analysis formulations to be applied in rigid blocks problems. The formulation of rigid block problem is similar to basic DLO formulation which considers both the compatibility and flow rule, but the two formulations are not totally the same. For the DLO formulation applied in continuum problems, the discontinuities are not known in advance. A discretization step is initially required, before an optimum solution can be sought. But the discontinuities are predefined in the rigid block problem. So the number of failure mechanisms to develop is limited.

The basic assumption for the developed formulation of rigid block problem is: each block has three degrees of freedom around its centroid: horizontal displacement, vertical displacement and rotation. Correspondingly three forces act along the joints between blocks: shear force (S), normal force (N) and moment (M), as shown in Figure 3.8. Considering an assemblage of b blocks and c joints, the equilibrium form can be expressed as follows:

$$\max \lambda \tag{3.29}$$

subject to:

$$\mathbf{Bq} - \lambda \mathbf{f}_{\mathrm{L}} = \mathbf{f}_{\mathrm{D}} \tag{3.30}$$

$$\mathbf{N}^T \mathbf{q} \leq \mathbf{C}$$

(3.31)

where λ is the load factor, $\mathbf{B}$ is a suitable $(3b \times 3c)$ equilibrium matrix, enforcing horizontal,vertical and moment equilibrium, $\mathbf{N}$ is a suitable $(4c \times 3c)$ constraint matrix, $\mathbf{C}$ is a suitable $(4c \times 1)$ intercept matrix (the cohesion coefficient is assumed zero here), $\mathbf{q}$ and $\mathbf{f}$ are respectively vectors of joint forces and block loads. Thus matrix $\mathbf{q}^T = \{N_1, S_1, M_1, N_2, S_2, M_2, ...N_c, S_c, M_c\}$; where N_i,S_i and M_i represent respectively the normal and shear force and rotation moment acting on joint i $(i = 1...c)$. $\mathbf{f}_{\mathrm{D}}$ and $\mathbf{f}_{\mathrm{L}}$ are vectors containing respectively specified dead and live loads. The LP variables are therefore N_i, S_i, M_i and the live load factor λ. The objective is thus to maximize λ whilst ensuring that the yield condition is not violated along any joint between blocks $i = 1, ...c$..

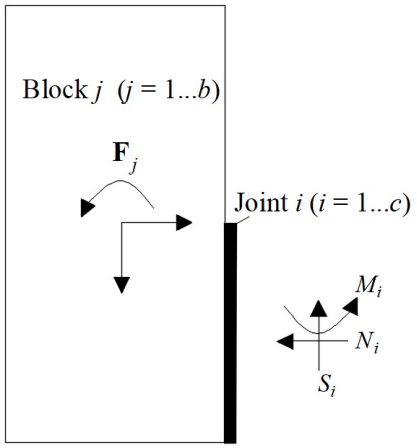

Figure 3.8: Blocks and joints in rigid block problem.

Duality theory means that whichever formulation is solved, the other is automatically solved too. Its associative kinematic form is,

$$\min \ -\mathbf{f}_{\mathrm{D}}^{T}\mathbf{d} + \mathbf{C}^{T}\mathbf{p} \tag{3.32}$$

subject to:

$$\mathbf{N}\mathbf{p} - \mathrm{B}^{\mathbf{T}}\mathbf{d} = \mathbf{0} \tag{3.33}$$

$$\mathbf{f}_{\mathrm{L}}^{T}\mathbf{d} = 1 \tag{3.34}$$

$$\mathbf{p} \geq \mathbf{0} \tag{3.35}$$

where $\mathbf{d}^{T}$ is a $3b-$ vector of nodal unconstrained displacement rates of the block centroids (corresponding to the nodal loads $\mathbf{f}$ in a virtual work sense). The displacement rates in $\mathbf{d}$ and the resultant displacement rates in $\mathbf{p}$ are the LP variables.

Furthermore, for the same contact interface, the displacement rates contained in u_i are related to the respective non-negative resultant displacement rates in p_i as follows:

$$\mathbf{u_i} = \mathbf{N}_i^0\mathbf{p}_i, \mathbf{p}_i \geq 0 \tag{3.36}$$

where now $\mathbf{u}$ contains displacements along the joints, $\mathbf{u}^{T} = \{\varepsilon_1, \gamma_1, \kappa_1, \varepsilon_2, \gamma_2, \kappa_2 ... \varepsilon_c, \gamma_c, \kappa_c\}$, where ε_i, γ_i and κ_i are the displacement rates between blocks at joints i describing joint separation, sliding and rotation (related to $\mathbf{q}$ in a virtual work sense); $\mathbf{p}$ is a $(4c)$ vector of resultant displacement rates. The normality rule is satisfied when $\mathbf{N}_i^0 = \mathbf{N}_i$, i.e. when dilation angle ψ_i equals friction angle ϕ_i (in associative formulation). The associative solution can be used to determine the global optimal solution (both upper and lower bound) for fixed boundaries and rigid blocks.

By considering the non-associative friction of the joints, some scholars attempted to predict the collapse load using non-linear mathematical programming, e.g., Baggio & Trovalusci (2000) and Ferris & Tin-Loi (2001). However, the non-linear formulation was found to be complex to implement and computationally expensive. By assuming the frictional interfaces described by a Mohr-Coulomb yield rule, Gilbert et al. (2006) put forward a method to solve non-associative rigid block problems using a series of linear programming problems with successively modified failure surfaces. Inspired by Gilbert et al.'s contribution, Babiker et al. (2014) proposed the non-associative iterative method to conduct a non-associative limit analysis of the toppling-sliding failure of rock slopes. By assuming that the flow and yield functions are separate, an iterative numerical method (NAIM stands for the Non-Associative Iterative Method) is used to obtain a valid kinematic solution by Babiker et al. (2014). The successive solution of the simple associative problem is obtained using a rotated linear yield surface. A 'Min-Max procedure' was also proposed to bracket the range of non-associative solutions since the solution is not unique based on the non-associative flow rule. Using this computational limit analysis procedure, the risk of non-convergence could not be avoided during the iterative process and different LP solvers may generate non-consistent results, which puts limitations on this procedure for producing non-associative solutions.

3.5 Conclusions

1. The DLO (Discontinuity layout optimization) formulation and the rigid block formulation are described. For continuum problem, the discontinuities are not known in the assumption. But the discontinuities are predefined in the rigid block problem.

2. The proposed DLO procedure using several linear yield surfaces to encompass the non-linear surface is used to predict the limit load for a smooth retaining wall problem. Best fit solutions have been derived for 1, 2 and 3

tangent models which may be generalized to different geotechnical problems (i.e. pseudo-static earth pressure problem and anchor problem.).

3. The developed rigid block formulation has been extended to solve non-associative block problems, but some limitations of the current published work could not be ignored. Therefore, a new method should be proposed to solve non-associative block problem.

Chapter 4

Limit analysis of material possess a non-linear yield surface: a variational approach

4.1 Introduction

In order to explore the effects of a non-linear yield surface on the stability of geotechnical problems, various methods have been developed. By extending the approach presented by Fraldi & Guarracino (2009), this study presents a new fully general form of the variational approach for analysing translational upper bound problems and this work has been published in the Canadian Geotechnical Journal (Zhang & Smith 2019).

Compared with the multi-tangent technique combined with the DLO procedure, the proposed variational method requires the solution to model a curved failure surface rigorously, instead of using several straight lines to approximate the curved failure surface.

In this chapter, examples are given for the upper bound analysis of active and passive cases of a smooth retaining wall and shown to match to within ∼1% of the corresponding simple non-linear lower bounds, thus for the first time giving almost

	Linear		Non-linear	
Parameter	Cohesive-frictional soil (CF) $c = 1$ kPa, $\phi = 30°$	Loose sand (LS) Bolton $I_D = 0$	Dense sand (DS) Bolton $I_D = 1$	Fractured rock (FR) Hoek-Brown
a(-)	1	0	0	0
c_0(kN/m^2)	1	1	1.697	1.8242×10^3
σ_t(kN/m^2)	$1/\tan 30°$	$1/\tan 33°$	1	5×10^3
m(-)	1.001	1.001	1.1182	1.3155
γ(kN/m^3)	15	15	15	22

Table 4.1: Exemplar linear and non-linear soil properties and unit weights.

exact plastic solutions for these cases. An intriguing aspect of the solutions is that they give exact values of shear and normal stresses along the slip-lines, which is not normally obtained from an upper bound analysis that can only return forces on wedge interfaces. The interpretation of such values is discussed in the context of the examples studied.

In this chapter two exemplar non-linear materials will be modelled, representing (i) a dense sand (based on the model by (Bolton 1986) using a relative density index $I_D = 1$) and (ii) a fractured rock mass (approximating a Hoek-Brown material with $\sigma_{ci} = 5$ MN/m^2, $m_i = 9.6$, $GSI = 20$, $m_b = 0.55$, Hoek & Brown 1997). The properties are given in Table 4.1. These were obtained by generating the relevant yield surface and carrying out a least squares best fit to Eq.2.8. For comparison, two linear soils were also modelled using (i) a simple $c = 1$ kN/m^2, $\phi = 30°$Mohr-Coulomb soil and (ii) a $c = 0$, $\phi = 33°$soil corresponding to the previous Bolton model at critical state. In both these cases, a value of $m = 1.001$ was adopted to model a closely linear system while still capable of adopting the non-linear solution methodology. It is shown in **Appendix B** that this leads to an error of $< 0.037\%$ in modelling the linear yield surface. As the aim of the study is to illustrate and verify the solution process and to contextualise it, specific engineering examples will be studied rather than undertaking parametric studies.

The assessment of pseudo-static active earth pressure as the result of an earthquake is also of practical significance in the design of retaining walls. Based on the

classical limit equilibrium theory, the seismic earth pressures are conventionally evaluated within the framework of Mononobe-Okabe method (Mononobe 1929) in the earthquake zones. The Mononobe-Okabe (Mononobe 1929) analysis of seismic earth pressures is a direct modification of the Coulomb wedge method where the earthquake effects are replaced by a quasi-static inertia force. Shukla (2015) derived a general expression of active earth pressure with considering effects of different practical aspects. However, most researchers analyzed the pseudo-static earth pressures without considering the assumption that backfills are governed by a non-linear failure criterion. In this chapter, the calculation of pseudo-static active earth pressure using the non-linear failure criterion is also put forward.

4.2 Analytical derivation

Consider a slip-line, which may be curved in the general case, connecting two points A and B whose secant is orientated at an angle θ to the positive x-axis and of length l. Further consider that there is a velocity jump of v across this slip-line orientated at a fixed angle ψ_s to its secant. This velocity will therefore be orientated at an angle α to the vertical where $\alpha = \pi/2 - \kappa\psi_s - \theta$ and $\kappa = \pm 1$ denotes clockwise or anticlockwise shear respectively across the slip-line. The aim is to determine the shape of the slip-surface joining A and B that will no longer be a secant, but will curve slightly above or below the secant depending on the relative movement as shown in Figure 4.1, such that the sum of the local dilation ψ and slip-line gradient at any point is constant and equal to the global slip-line dilation ψ_s. This preserves the assumption of rigid body movement of adjacent wedges. To maintain the work calculation for the general mechanism analysis similar to the linear case, a dissipation coefficient $\hat{C}$ for a non-linear material will be derived equivalent to the cohesion intercept term cl for a linear soil and where the self weight of the wedges delineated by the secants may still be used, but where the slip-line will also have its own additional self weight term $\hat{W}$ defined by the area of soil between the

curved slip-line and the secant. This may be negative or positive depending on the direction of relative shear.

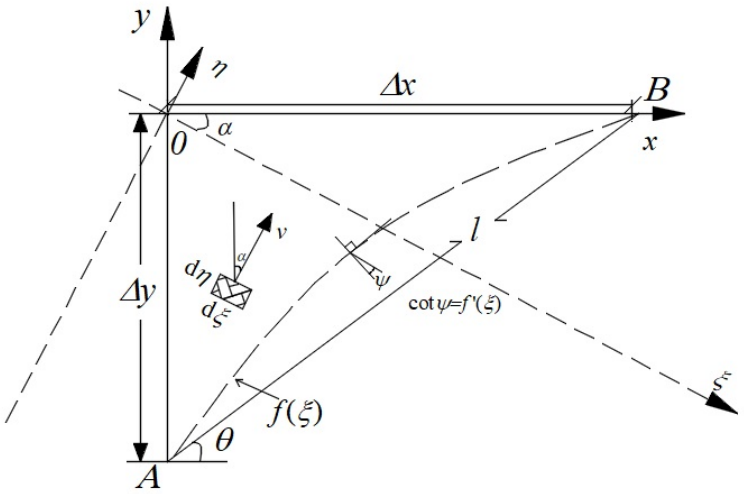

(a) Clockwise

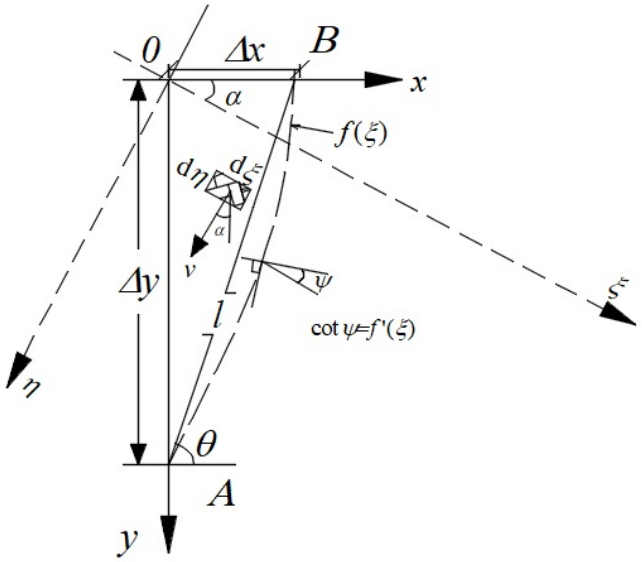

(b) Anticlockwise

Figure 4.1: Non-linear kinematics of a slip-line (long-dashed line between A and B). Relative shear across slip-line: (a) clockwise; (b) anticlockwise.

4.2.1 General analysis form for single slip-line

4.2.1.1 Compatibility

For a single slip-line as shown in Figure 4.1, the mass of soil above the slip-line moves as a rigid block at velocity v and at an angle α to the vertical relative to the soil below. Let $y = f(x)$ be the equation of the velocity discontinuity surface.

This can be expressed in a rotated coordinate system as $\eta = f(\xi)$, and

$$\begin{bmatrix} \xi \\ \eta \end{bmatrix} = \begin{bmatrix} \cos\alpha & -\sin\alpha \\ \sin\alpha & \cos\alpha \end{bmatrix} \begin{bmatrix} x \\ y \end{bmatrix} \tag{4.1}$$

Use of this new coordinate system simplifies the subsequent analysis by making the velocity v parallel to the η axis. By assuming the plastic potential, ς, to be coincident with the yield envelope and considering τ is positive, the following can be defined:

$$\varsigma = \tau - c_0(a + \sigma_n/\sigma_t)^{1/m} \tag{4.2}$$

Adapting the approach developed for a tunnel analysis in a Hoek-Brown material by Fraldi & Guarracino (2009), and assuming associative flow, the local angle of dilation ψ may be given by the following equation:

$$\tan\psi = \frac{d\tau}{d\sigma_n} = \frac{c_0(a + \sigma_n/\sigma_t)^{\frac{1-m}{m}}}{m\sigma_t} \tag{4.3}$$

and because relative movement of the block above the discontinuity is parallel to the η-axis, the following can also be written:

$$\tan\psi = \frac{1}{\kappa f'(\xi)}, \quad \cos\psi = \kappa f'(\xi)\left[1 + f'(\xi)^2\right]^{-\frac{1}{2}}, \quad \sin\psi = \left[1 + f'(\xi)^2\right]^{-\frac{1}{2}} \tag{4.4}$$

where $\kappa = 1$ for the clockwise relative shear case and $\kappa = -1$ for the anti-clockwise relative shear case.

Combining Eqs.4.3 and 4.4 gives

$$\sigma_n = -a \cdot \sigma_t + \sigma_t \left(\frac{c_0}{m\sigma_t} \right)^{\frac{m}{(m-1)}} [\kappa f'(\xi)]^{\frac{m}{(m-1)}} \tag{4.5}$$

and substitution in Eq. 2.8 gives,

$$\tau = c_0 \left(\frac{c_0}{m\sigma_t} \right)^{\frac{1}{(m-1)}} [\kappa f'(\xi)]^{\frac{1}{(m-1)}} \tag{4.6}$$

Now the plastic strain rates can be written as follows:

$$\dot{\varepsilon}_n = \lambda \frac{\partial \varsigma}{\partial \sigma} = -\lambda \frac{c_0}{m\sigma_t} (a + \sigma_n/\sigma_t)^{(1-m)/m} \tag{4.7}$$

$$\dot{\gamma} = \lambda \frac{\partial \varsigma}{\partial \tau} = \lambda \tag{4.8}$$

where λ is a scalar parameter, $\dot{\varepsilon}_n$ is the normal plastic strain rate and $\dot{\gamma}$ is the shear plastic strain rate. Based on the kinematics occurring on the slip-line, as shown in Figure 4.1, the plastic strain rate components can also be written in the form

$$\dot{\varepsilon}_n = v_n = -\frac{v}{w} \left[1 + f'(\xi)^2 \right]^{-\frac{1}{2}} \tag{4.9}$$

$$\dot{\gamma} = v_t = \frac{v}{w} \kappa f'(\xi) \left[1 + f'(\xi)^2 \right]^{-\frac{1}{2}} \tag{4.10}$$

where $\eta = f(\xi)$ is the function of velocity discontinuity surface and $f'(\xi)$ is the first derivative of $f(\xi)$. v is the velocity jump at the slip-line and w is the thickness of the plastic zone (assumed infinitesimal). An overdot denotes differentiation with respect to time and a prime with respect to ξ, i.e. $v = \partial u/\partial t$, $f'(\xi) = \partial f(\xi)/\partial \xi$.

In order to enforce compatibility, from Eq. 4.8 and Eq. 4.10 (or equivalently from Eq. 4.5, Eq. 4.7 and Eq. 4.9) it follows that:

$$\lambda = \frac{v}{w}\kappa f'(\xi)\left[1 + f'(\xi)^2\right]^{-\frac{1}{2}} \tag{4.11}$$

4.3 Upper bound analysis

4.3.1 Determination of internal energy dissipation and external work

Based on the plastic potential function Eq. 4.2, the plastic strain increment is proportional to the gradient of the plastic potential function through the associated flow rule. The dissipation energy associated with the internal forces at any point on the surface, $\dot{D}_i$ can therefore be obtained by combining Eq. 4.5, Eq. 4.6, Eq. 4.9 and Eq. 4.10:

$$\dot{D}_i = \sigma_n v_n + \tau v_t = \frac{v}{w}\left[1 + f'(\xi)^2\right]^{-\frac{1}{2}}\left[a \cdot \sigma_t + \sigma_t\left(\frac{c_0}{m\sigma_t}\right)^{\frac{m}{(m-1)}}(m-1)[\kappa f'(\xi)]^{\frac{m}{(m-1)}}\right] \tag{4.12}$$

By considering the profile of the failure surface for the single wedge, as shown in Figure 4.1, the energy dissipation along the velocity discontinuity surface can be obtained by integrating $\dot{D}_i$ over the interval $\xi = \Delta y \sin\alpha$ to $\Delta x \cos\alpha$ where $\Delta x = l\cos\theta$ and $\Delta y = l\sin\theta$.

Hence

$$\begin{aligned} D &= \int_{\Delta y \sin\alpha}^{\Delta x \cos\alpha} \dot{D}_i w \sqrt{1 + f'(\xi)^2}\, d\xi \\ &= v\int_{\Delta y \sin\alpha}^{\Delta x \cos\alpha}\left\{ a \cdot \sigma_t + \sigma_t\left(\frac{c_0}{m\sigma_t}\right)^{\frac{m}{(m-1)}}(m-1)[\kappa f'(\xi)]^{\frac{m}{(m-1)}}\right\} d\xi \end{aligned} \tag{4.13}$$

The work done (W_e) by the external force (gravity) on the area between the curve and the secant is given as follows (note that in the active case, the area is negative, but the integration is also negative.):

$$W_e = \kappa v \gamma \cos\alpha \left[\int_{\Delta y \sin\alpha}^{\Delta x \cos\alpha} f(\xi) d\xi + \Delta y \cos\alpha (\Delta x \cos\alpha - \Delta y \sin\alpha) - 0.5 l^2 \sin(\theta+\alpha)\cos(\theta+\alpha) \right] \tag{4.14}$$

4.3.2 Solution characterizing optimal slip-line geometry

In order to describe the optimal shape of the slip-line, it is necessary to obtain the explicit expression of $f(\xi)$ by constructing an objective function Λ consisting of the sum of the contribution of the slip-line to the external work rate and the rate of the internal energy dissipation,

$$\begin{aligned} \Lambda &= D - W_e \\ &= v \int_{\Delta y \sin\alpha}^{\Delta x \cos\alpha} \zeta[f(\xi), f'(\xi), \xi] d\xi \\ &\quad - v\kappa\gamma\cos\alpha \left[\Delta y \cos\alpha (\Delta x \cos\alpha - \Delta y \sin\alpha) - 0.5 l^2 \sin(\theta+\alpha)\cos(\theta+\alpha) \right] \end{aligned} \tag{4.15}$$

in which

$$\zeta[f(\xi), f'(\xi), \xi] = \sigma_t \left[a + \left(\frac{c_0}{m\sigma_t} \right)^{\frac{m}{(m-1)}} (m-1)[\kappa f'(\xi)]^{\frac{m}{(m-1)}} \right] - \kappa\gamma f(\xi)\cos\alpha \tag{4.16}$$

In order to obtain the effective failure surface for a given slip-line of angle θ and length l, it is necessary to search for the extremum value of objective function Λ using Euler's equation through the variational method. Inspired by a classical

calculus of variations proposed by Fraldi & Guarracino (2009), the expression of the variational equation of Λ for stationary conditions can be written as:

$$\frac{\partial \Lambda}{\partial f(\xi)} - \frac{\partial}{\partial \xi}\left[\frac{\partial \Lambda}{\partial f'(\xi)}\right] = 0 \tag{4.17}$$

and the explicit form of Euler's equation for the Eq. 4.16 can thus be obtained as:

$$\kappa\gamma\cos\alpha + \frac{m\sigma_t}{(m-1)}\left(\frac{c_0}{m\sigma_t}\right)^{\frac{m}{m-1}}[\kappa f'(\xi)]^{\frac{2-m}{m-1}}[f''(\xi)] = 0 \tag{4.18}$$

Eq. 4.18 is a non-linear second-order homogeneous differential equation. A first integration yields

$$m\sigma_t\left(\frac{c_0}{m\sigma_t}\right)^{\frac{m}{m-1}}[\kappa f'(\xi)]^{\frac{1}{m-1}} = -\kappa\gamma\cos\alpha\cdot\xi + n_0 \tag{4.19}$$

where n_0 is integration constant coefficient. Re-arrangement of this equation gives:

$$f'(\xi) = \kappa m k_0(\frac{n_0}{\gamma\cdot\cos\alpha} - \kappa\xi)^{m-1} \tag{4.20}$$

in which

$$k_0 = \frac{\sigma_t}{\gamma\cos\alpha}\left(\frac{\gamma\cdot\cos\alpha}{c_0}\right)^m = \frac{\sigma_t}{c_0}\left(\frac{\gamma\cdot\cos\alpha}{c_0}\right)^{m-1} = \frac{\sigma_t}{c_0^m}(\gamma\cos\alpha)^{m-1} \tag{4.21}$$

By a further integral calculation process, the equation for the velocity discontinuity surface is given by:

$$f(\xi) = -k_0(\frac{n_0}{\gamma\cdot\cos\alpha} - \kappa\xi)^m + n_1 \tag{4.22}$$

and an additional integration provides an expression required later for the weight correction term:

$$\int f(\xi).d\xi = \frac{\kappa k_0}{m+1}(\frac{n_0}{\gamma\cdot\cos\alpha} - \kappa\xi)^{m+1} + n_1\xi + \text{const} \tag{4.23}$$

where n_0 and n_1 are two unknowns representing the integration constant coefficients. These can be determined using the two boundary conditions:

$$f(\xi = \Delta y \sin\alpha) = -\Delta y \cos\alpha \tag{4.24}$$

$$f(\xi = \Delta x \cos\alpha) = \Delta x \sin\alpha \tag{4.25}$$

Hence:

$$-k_0(\frac{n_0}{\gamma\cos\alpha} - \kappa\Delta x\cos\alpha)^m + n_1 - \Delta x\sin\alpha = 0 \tag{4.26}$$

and

$$n_1 = -\Delta y\cdot\cos\alpha + k_0(\frac{n_0}{\gamma\cdot\cos\alpha} - \kappa\Delta y\cdot\sin\alpha)^m \tag{4.27}$$

It is not possible to derive closed form expressions for n_0 and n_1, however by substituting Eq. 4.27 into Eq. 4.26, these may be determined straightforwardly numerically using standard root finding algorithms. There is a small range of values of α and hence ψ_s that will give valid solutions.

The standard root finding algorithms can be demonstrated as following.

$$(\frac{n_0}{\gamma\cdot\cos\alpha} - \kappa\Delta y\cdot\sin\alpha)^m - (\frac{n_0}{\gamma\cos\alpha} - \kappa\Delta x\cos\alpha)^m = \frac{\Delta x\sin\alpha + \Delta y\cdot\cos\alpha}{k_0} \tag{4.28}$$

Let

$$p = \frac{n_0}{\gamma\cos\alpha} \tag{4.29}$$

$$A = \kappa\Delta y\cdot\sin\alpha \tag{4.30}$$

$$B = \kappa \Delta x \cos \alpha \tag{4.31}$$

and

$$C = \frac{\Delta x \sin \alpha + \Delta y \cdot \cos \alpha}{k_0} \tag{4.32}$$

Then we need to solve:

$$(p - A)^m - (p - B)^m = C \tag{4.33}$$

For non-integer m this only has solutions if the following conditions are satisfied:

$(p - A) > 0$, and $(p - B) > 0$ and

1. If $A > B$:

   a) $p \geq A$

   b) in special case where $p = A$, then $-(A - B)^m = C$,

      in special case where $p = A + \epsilon$, where ϵ is +ve, then $\epsilon^m - (A - B + \epsilon)^m = C$.

      Hence as p increases above A and so $\epsilon > 0$. If $\epsilon > 0$ then $\epsilon^m - (A - B + \epsilon)^m < -(A - B)^m$

      Hence $C \leq -(A - B)^m$.

2. If $B > A$:

   a) $p \geq B$

   b) in special case where $p = B$, then $(B - A)^m = C$,

      in special case where $p = B + \epsilon$, where ϵ is +ve, then $(B - A + \epsilon)^m - \epsilon^m = C$

      Hence as p increases above B and so $\epsilon > 0$. If $\epsilon > 0$ then $(B - A + \epsilon)^m - \epsilon^m > (B - A)^m$

      Hence $C \geq (B - A)^m$

Looking at the form of the equations, as p increases, $(p-A)^m-(p-B)^m$ increases. Therefore there can be only one real root. In the special case of $m=2$

$$(p-A)^2-(p-B)^2=C \tag{4.34}$$

$$p^2+A^2-2Ap-p^2-B^2+2Bp=C \tag{4.35}$$

$$p=\frac{C+B^2-A^2}{2(B-A)} \tag{4.36}$$

which still has only one root. In order to obtain the root p, the process for solving non-linear function is carried out numerically using MATLAB's built in function $fzero$.

Using the proposed algorithms, the values of α and ψ_s can be obtained.

This solution may be expressed as a dilation (relative to the secant) of $\psi_s=\kappa(\pi/2-\alpha-\theta)$, a coefficient of dissipation $\hat{C}(\psi_s,\theta,l)$ based on Eq. 4.13 and a correction to the wedge weight above the slip-line $\hat{W}(\psi_s,\theta,l)$ based on Eq. 4.14. $\hat{C}$ is equivalent to the term cl for the linear case. Thus $\hat{C}$ is multiplied by $s=v\cos\psi_s$ to give the full dissipation. Hence expressions for $\hat{C}$ and $\hat{W}$ can be written in terms of the derived function f:

From Eq. 4.13:

$$\begin{aligned}\hat{C}(\psi_s,\theta,l)=\frac{\kappa\sigma_t}{\cos\psi_s}\left(\frac{m-1}{m+1}\right)\left(\frac{\gamma\cos\alpha}{c_0}\right)^m[(\frac{n_0}{\gamma\cos\alpha}-\kappa\Delta y\sin\alpha)^{m+1}-(\frac{n_0}{\gamma\cos\alpha}-\kappa\Delta x\cos\alpha)^{m+1}]\\ +a\cdot\frac{\sigma_t}{\cos\psi_s}(\Delta x\cos\alpha-\Delta y\sin\alpha)\end{aligned} \tag{4.37}$$

and from Eq. 4.14 and Eq. 4.23:

$$\frac{\hat{W}(\psi_s,\theta,l)}{\kappa\gamma} = \frac{\kappa k_0}{m+1}[(\frac{n_0}{\gamma\cos\alpha} - \kappa\Delta x\cos\alpha)^{m+1} - (\frac{n_0}{\gamma\cos\alpha} - \kappa\Delta y\sin\alpha)^{m+1}] + n_1(\Delta x\cos\alpha - \Delta y\sin\alpha) + \Delta y\cos\alpha(\Delta x\cos\alpha - \Delta y\sin\alpha) - 0.5l^2\sin(\theta+\alpha)\cos(\theta+\alpha) \tag{4.38}$$

These functions are straightforward to compute using a spreadsheet or computer program.

4.3.3 General solution procedure

The following outlines a typical hand solution process following the standard form of linear upper bound wedge analysis.

1. Postulate an appropriate multi-wedge failure mechanism, involving a series of nodes linking slip-lines that delineate each wedge, allocating an appropriate value of global dilation ψ_s to each slip-line. ψ_s must be chosen to generate real values of n_0 and n_1 for each slip-line.

2. Based on the straight lines joining each node and the values of ψ_s, draw the corresponding hodograph.

3. Determine the acting weight W of each wedge based on the area of the wedge delineated by straight lines joining each node, and adjusted according to the term $\hat{W}$ for each slip-line edge of the wedge.

4. Determine the external work done using the velocities from the hodograph and the weight of each wedge, and the external live and dead loads.

5. Determine the internal energy dissipation $\hat{C}v\cos\psi_s$ based on the relative velocities v across each slip-line.

6. Equate external work and internal energy dissipation to determine the live load.

4.4 Smooth retaining wall

Having derived a generic solution process, its application will be illustrated through a range of specific geotechnical problem types: active and passive smooth retaining walls. This may be done by deriving the full energy equation for the specific problem and then minimising the energy by varying the assumed values of wedge angle and dilation angle ψ_s for each slip-line, to give the optimal upper bound for the slip-line mechanism. In this thesis, the optimization of the upper bound solution is carried out numerically using MATLAB's built-in multi-parameter minimisation function $fminsearch$. The start point can be selected by iterative process.

4.4.1 Upper bound analysis

Consider a frictionless vertical wall of height H with horizontal active or passive load F, and a surface surcharge q with a single wedge at angle θ to the horizontal and area of $0.5H^2/\tan\theta$ as shown in Figure 4.2 together with the hodograph. The slip-line secant length $l = H/\sin\theta$.

If the dilation is assumed to be ψ_s, the wedge moves at a velocity v_0 at an angle $\theta + \kappa\psi_s$ to the horizontal and the full energy equation may be expressed as:

$$F\kappa v_0 \cos(\theta+\kappa\psi_s) = \left[\frac{H^2\gamma}{2\tan\theta} - \kappa\hat{W}(\psi_s,\theta,l) + \frac{qH}{\tan\theta}\right]\kappa v_0 \sin(\theta+\kappa\psi_s) + \hat{C}(\psi_s,\theta,l)v_0\cos\psi_s \tag{4.39}$$

where $\kappa = 1$ for the passive case and $\kappa = -1$ for the active case.

This is identical to a conventional linear analysis with the addition of the $\hat{W}$ term and the replacement of the cl term by $\hat{C}$. To find the optimal upper bound, it is

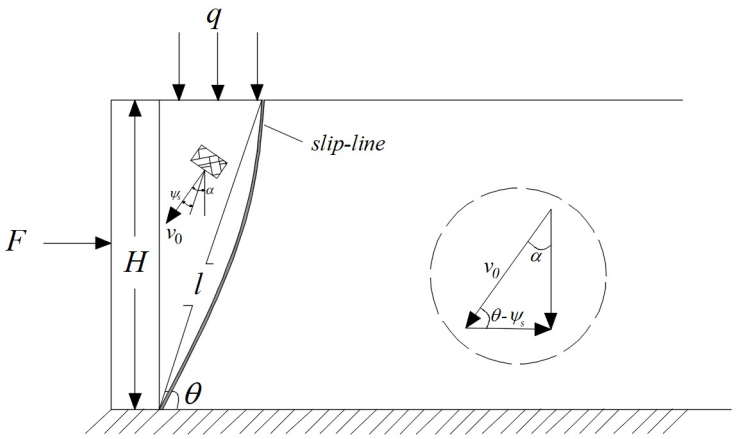

(a) Active

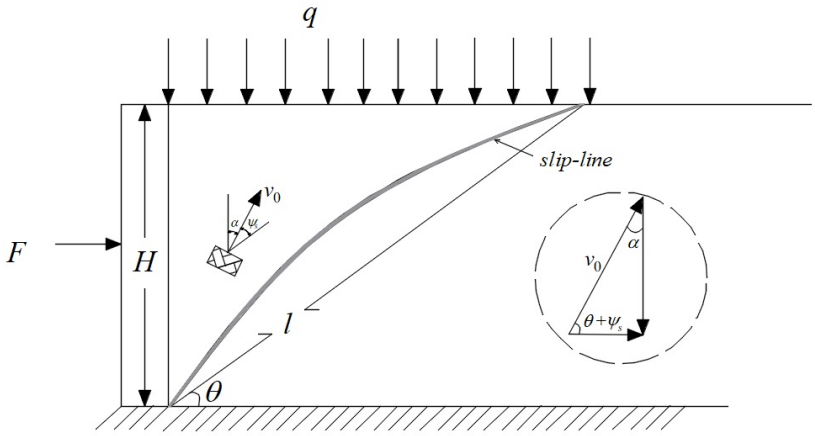

(b) Passive

Figure 4.2: Failure mechanism analysis for smooth retaining wall with surcharge load.

necessary to find max $F(\psi_s, \theta)$ for the active case and min $F(\psi_s, \theta)$ for the passive case.

The optimization must thus be done in two parameters rather than the one (θ) for the linear problem and is straightforward to carry out numerically using Eq. 4.39. Solutions using the example parameter sets (given in Table 4.1), are given in Table 4.2. A single maximum/minimum exists in each case as shown in Figure 4.3 for the fractured rock material. Note that the solutions assume that tensile stresses are sustainable on the back of the wall for the cohesive-frictional soil.

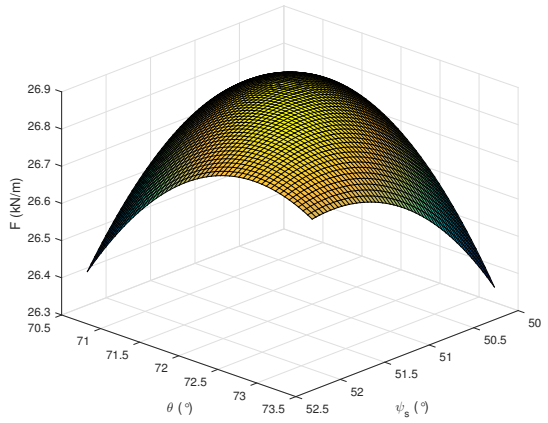

(a) Active

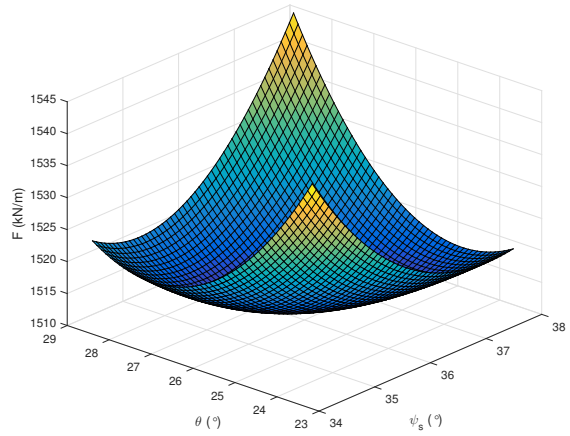

(b) Passive

Figure 4.3: Variation of thrust F with θ and ψ_s for a smooth retaining wall with surcharge load for the fractured rock material (properties given in Table 4.1) and $q = 5$ kN/m^2, and $H = 5$m.

Failure mode	Parameter set	θ_{opt}	$\psi_{s,opt}$	n_0	F_{upper} (kN/m)	F_{lower} (kN/m)	% difference	F_{linear} (kN/m)
Active	CF	59.96°	29.92°	-8.927	65.2573	65.2573	0.000	65.05983
	LS	61.46°	32.91°	-7.836	62.8278	62.8278	0.000	62.6451
	DS	70.90°	50.78°	-1.5629	23.8231	23.8633	0.169	-
	FR	71.99°	51.24°	-2.791	26.8704	27.3218	1.680	-
Passive	CF	30.05°	29.89°	102.93	652.3262	652.3262	0.000	654.8205
	LS	28.56°	32.88°	111.32	717.7809	717.7809	0.000	720.8255
	DS	22.38°	44.39°	168.81	1349.0075	1347.7533	0.093	-
	FR	26.18°	36.10°	201.42	1511.5016	1506.3272	0.342	-

Table 4.2: Retaining wall solutions for the case $q = 5$ kN/m^2, and $H = 5$m, using material properties from Table 4.1. The values of F_{linear} are computed using conventional Rankine equations for a smooth retaining wall where $\sigma'_h = K_a\sigma'_v - K_{ac}c'$, $K_a = \tan^2(\pi/4 - \phi/2)$ and $K_{ac} = 2\sqrt{K_a}$, and similarly for the passive case.

Each model was checked against a simple Rankine lower bound based on the non-linear yield surface. Very close matches were found for the approximately linear materials as expected, and matches within ∼1% for the non-linear materials. The values thus bracket the true solution very closely. Comparison of the lower bound solutions to the known linear solution for the first two materials show they are close. Further checks show that they do converge as would be expected as m is reduced towards 1.0.

4.4.2 Lower bound analysis

For a smooth wall with a vertical soil-wall interface, the same simple stress state configuration may be used for a non-linear soil as for a linear soil; namely, the assumption that principal stresses are horizontal and vertical. The vertical stresses may thus be predicted by the following simple equation:

$$\sigma_v = q + \gamma z \tag{4.40}$$

where q is the surface surcharge and z is the depth below the surface. Hence drawing the largest or smallest Mohr's circle through this point that touches the non-linear yield surface will determine the passive or active lateral earth pressures, respectively. Depending on the nature of the yield surface, the circle may be limited

by a tangent to the main curve or by the apex of the yield surface when $\tau = 0$. Given that:

$$\tau = c_0(a + \sigma_n/\sigma_t)^{1/m} \tag{4.41}$$

the lowest value of σ_n is when $\tau = 0$:

$$\sigma_{n,min} = -a\sigma_t \tag{4.42}$$

At any point the gradient is given by:

$$\tan\psi_t = \frac{d\tau}{d\sigma_n} = \frac{c_0}{m\sigma_t}(a + \sigma_n/\sigma_t)^{(1-m)/m} \tag{4.43}$$

where ψ_t is the angle of the tangent to the yield surface measured relative to the horizontal.

$$\frac{d^2\tau}{d\sigma_n^2} = \frac{c_0(1-m)}{m^2\sigma_t^2}(a + \sigma_n/\sigma_t)^{(1-2m)/m} \tag{4.44}$$

Hence curvature given by:

$$k = \frac{\frac{c_0(1-m)}{m^2\sigma_t^2}(a + \sigma_n/\sigma_t)^{(1-2m)/m}}{[1 + \frac{c_0^2}{m^2\sigma_t^2}(a + \sigma_n/\sigma_t)^{2(1-m)/m}]^{\frac{3}{2}}} \tag{4.45}$$

$$k = \frac{\frac{c_0(1-m)}{m^2\sigma_t^2}(a + \sigma_n/\sigma_t)^{(1-2m)/m}\frac{m^3\sigma_t^3}{c_0^3}(a + \sigma_n/\sigma_t)^{(3m-3)/m}}{(\frac{m^2\sigma_t^2}{c_0^2}(a + \sigma_n/\sigma_t)^{2(m-1)/m} + 1)^{\frac{3}{2}}} \tag{4.46}$$

$$k = \frac{\frac{m(1-m)\sigma_t}{c_0^2}(a + \sigma_n/\sigma_t)^{(m-2)/m}}{[\frac{m^2\sigma_t^2}{c_0^2}(a + \sigma_n/\sigma_t)^{2(m-1)/m} + 1]^{\frac{3}{2}}} \tag{4.47}$$

when $\tau = 0$, $k = 0$

$$k = \frac{\frac{c_0(1-m)}{m^2\sigma_t^2}(a + \sigma_n/\sigma_t)^{(1-2m)/m}}{[1 + \frac{c_0^2}{m^2\sigma_t^2}(a + \sigma_n/\sigma_t)^{2(1-m)/m}]^{\frac{3}{2}}} \tag{4.48}$$

Referring to Figure 4.4,

$$s - \sigma_n = \tau \tan \psi_t = \frac{c_0^2}{m\sigma_t}(a + \sigma_n/\sigma_t)^{(2-m)/m} \tag{4.49}$$

$$s = \sigma_n + \frac{c_0^2}{m\sigma_t}(a + \sigma_n/\sigma_t)^{(2-m)/m} \tag{4.50}$$

$$\frac{ds}{d\sigma_n} = 1 + \frac{(2-m)c_0^2}{m^2\sigma_t^2}(a + \sigma_n/\sigma_t)^{(2-2m)/m} \tag{4.51}$$

Eq. 4.51 is always positive if $m < 2$ and indicates a switch of sign at:

$$a + \sigma_n/\sigma_t = \left[\frac{(m-2)c_0^2}{m^2\sigma_t^2}\right]^{\frac{m}{2(m-1)}} \tag{4.52}$$

$$\sigma_{n0} = -a \cdot \sigma_t + \sigma_t \left[\frac{(m-2)c_0^2}{m^2\sigma_t^2}\right]^{\frac{m}{2(m-1)}} \tag{4.53}$$

which corresponds to a value of s at:

$$s_0 = \sigma_{n0} + \frac{c_0^2}{m\sigma_t}\left[\frac{(m-2)c_0^2}{m^2\sigma_t^2}\right]^{\frac{2-m}{2(m-1)}} \tag{4.54}$$

It is thus necessary to work with Mohr's circles from $s = 0$ to s_0 that touch $\sigma_{n,min}$. Above s_0 the circles are tangential to the yield surface (as shown in Figure 4.4) and of radius t given as follows:

$$t = \sqrt{\tau^2 + (s-\sigma)^2} = \tau\sqrt{1 + \tan^2\phi} = \tau \sec^2 \phi \tag{4.55}$$

For active conditions

$$\sigma_v = s + t \tag{4.56}$$

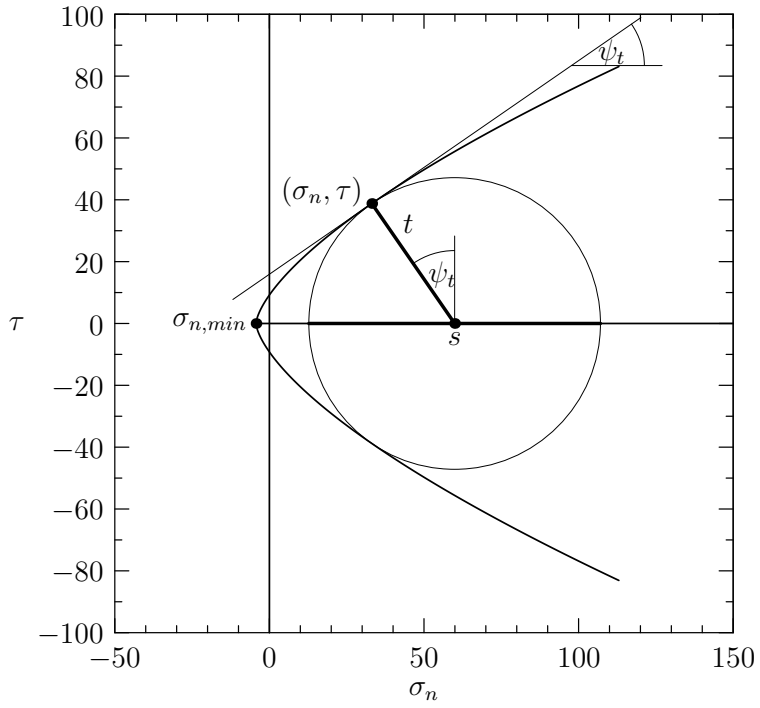

Figure 4.4: Mohr's circle for non-linear yield surface, $c_0 = 5$, $a = 2.5$, $\sigma_t = 1.0/\tan(30°)$, $m = 1.5$.

$$\sigma_h = s - t \tag{4.57}$$

For passive conditions

$$\sigma_v = s - t \tag{4.58}$$

$$\sigma_h = s + t \tag{4.59}$$

The condition that the Mohr's circle does not touch yield surface to left side.

$$1.0/k > t \tag{4.60}$$

and

$$s - t > \sigma_{n,min} \tag{4.61}$$

For high values of m, e.g. 2.5, the Mohr's circle is not tangential to the yield surface at low stresses, but limited by $\sigma_{n,min}$.

On the basis of active/passive conditions above, combining Eq. 4.50 and Eq. 4.55, and substituting Eq. 4.40 into it, we can obtain the following expressions:

$$\sigma_h = 2\sigma_n - \sigma_v + \frac{2c_0^2}{m\sigma_t}(a + \sigma_n/\sigma_t)^{(2-m)/m} \tag{4.62}$$

$$\sigma_h = \sigma_v - 2\sqrt{(c_0(a + \sigma_n/\sigma_t)^{1/m})^2 + (\frac{2c_0^2}{m\sigma_t}(a + \sigma_n/\sigma_t)^{(2-m)/m})^2} \tag{4.63}$$

If the parameters m, γ, c_0, σ_t, a, q are given, there are two variables and two equations. Using different z (different depth), the values of σ_n and σ_h could be obtained (the process for solving non-linear function system is carried out numerically using MATLAB's built-in function $fsolve$). The normal and shear stress distributions along failure surface could be predicted and plotted by the proposed lower bound analysis.

4.4.3 Discussion and comparison

The solution assumed that the shape of the non-linear slip-line could be described by a function $y = f(x)$. This assumption gives a relatively simple solution. There may be scope to achieve higher degrees of freedom in the solutions by adopting a parametric curve $f_p(x, y) = 0$, however this is beyond the scope of the present work.

Figure 4.5 shows the feasible range of optimal slip-lines for the passive wall fractured rock case for different values of θ with the optimum value of ψ_s in each case annotated on each line.

To put the results into context in comparison with a conventional linear analysis, a simple conservative analysis of the fractured rock problem could be carried out using a secant angle of friction across a suitable stress range. The non-linear lower bound analysis predicts a horizontal stress of $\sim$ 450 kN/m^2 at the wall base for the fractured rock parameters. Thus, selecting a range of 0 to 450 kN/m^2, which roughly spans the range of stresses expected in the problem, gives a secant angle of 33° (almost the same as the loose sand material). This gives a passive load of 1017 kN/m using a simple Rankine analysis (using the fractured rock self weight of 22 kN/m^3, and the linear angle of shearing resistance of 33°). This is about 2/3 of the non-linear result.

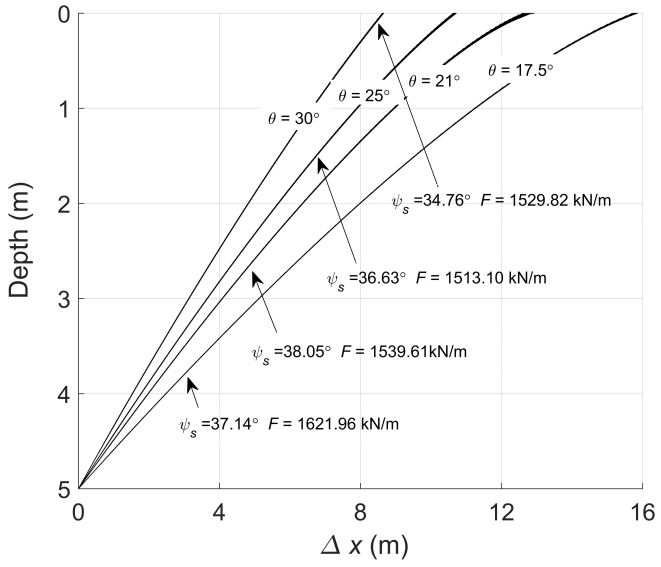

Figure 4.5: Sample set of possible passive slip-lines for fractured rock case for different values of θ and with ψ_s optimized for this value of θ (actual feasible range of values for θ ranges between 0.1° and 84°).

One intriguing aspect of the analysis as pointed out by Baker & Frydman (1983) and Chen (1975) is that the upper bound solution not only identifies the slip-line geometry, but also part of the stress state at every point along the line, using Eq. 4.5 and Eq. 4.6, since each point has a unique gradient. It is thus possible to plot

the shear stress and/or normal stress on the line with depth as shown in Figure 4.6 and Figure 4.7. For the active and passive walls, these values match reasonably closely to the values predicted by the lower bound approach (as would be expected). Note that the plotted lower bound values are those corresponding to the yield condition predicted by the lower bound at the relevant depth.

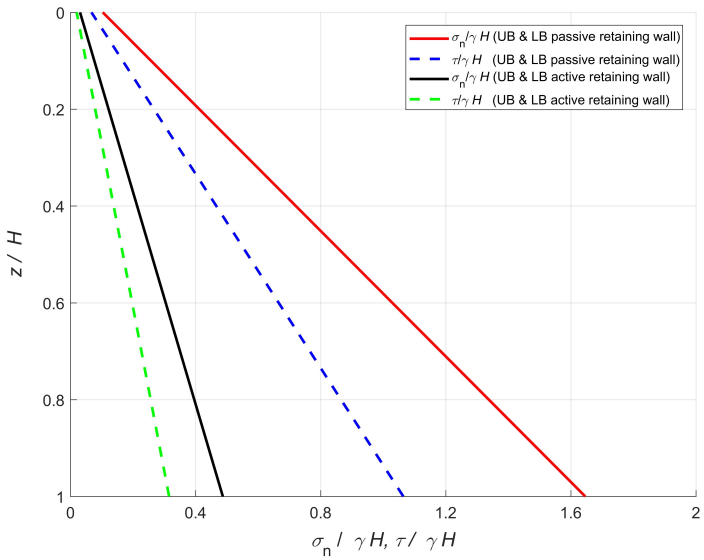

Figure 4.6: Predicted upper bound (UB) and lower bound (LB) normalised normal and shear stresses for active and passive retaining wall cases ($q = 5\text{kN/m}^2$ and $H = 5\text{m}$): loose sand case. Wall UB and LB solutions are coincident.

4.5 Pseudo static active earth pressure

In this section, the proposed method is extended to predict the pseudo-static active earth pressure. In a pseudo-static analysis, the imposition of horizontal and vertical seismic accelerations within the system results in additional work terms in the governing equation that are analogous to that for self-weight (Smith & Cubrinovski 2011). In order to include the external work caused by the horizontal and vertical seismic accelerations, the horizontal and vertical pseudo-static acceleration coefficients k_h and k_v are introduced in this study, as shown in Figure 4.8.

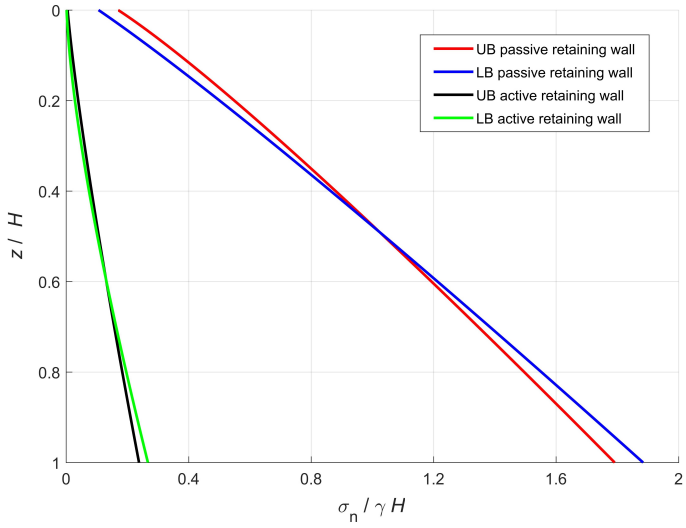

Figure 4.7: Predicted upper bound (UB) and lower bound (LB) normalised normal stresses for active and passive retaining wall cases ($q = 5\text{kN/m}^2$ and $H = 5\text{m}$): fractured rock case.

4.5.1 Extension of variational method to pseudo-static analysis

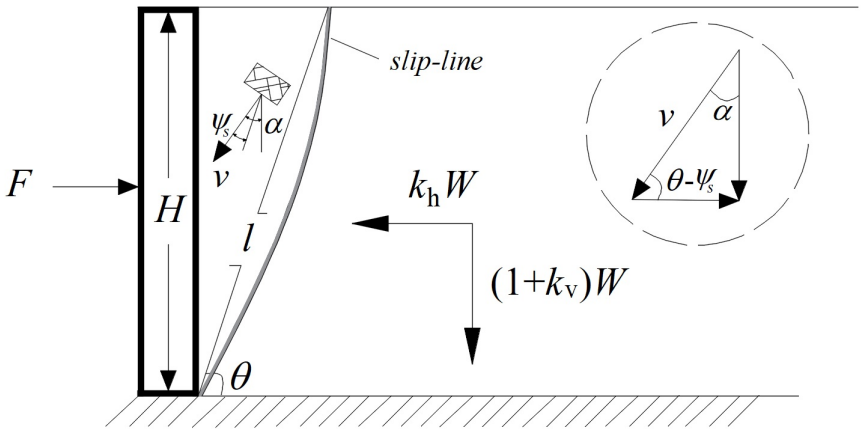

Figure 4.8: Non-linear active failure mechanism: pseudo-static analysis of retaining walls.

The work done (W_e) by the gravity under the influences of both horizontal and vertical acceleration coefficients on the area between the curve and the secant is given as follows (note that in the active case, the area is negative, the integration

is also negative.):

$$\begin{aligned} W_e = & -v\gamma[(1+k_v)\cos\alpha + k_h\sin\alpha]\int_{\Delta y\sin\alpha}^{\Delta x\cos\alpha} f(\xi)d\xi \\ & - v\gamma[(1+k_v)\cos\alpha + k_h\sin\alpha]\,[\Delta y\cos\alpha(\Delta x\cos\alpha - \Delta y\sin\alpha) \\ & - 0.5l^2\sin(\theta+\alpha)\cos(\theta+\alpha)] \end{aligned} \tag{4.64}$$

where γ is the weight per unit volume of the soils. $k_h[\rightarrow -/\leftarrow +]$ stands for horizontal acceleration coefficient; $k_v[\downarrow +/\uparrow -]$ stands for vertical acceleration coefficient.

By the similar variational calculation used for static earth pressure case, the equation for the velocity discontinuity surface is given by:

$$f(\xi) = -k_0\left(\frac{n_0}{\gamma((1+k_v)\cos\alpha + k_h\sin\alpha)} + \xi\right)^m + n_1 \tag{4.65}$$

in which

$$k_0 = \frac{\sigma_t\gamma^{m-1}}{c_0^m}[(1+k_v)\cos\alpha + k_h\sin\alpha]^{m-1} \tag{4.66}$$

In terms of the smooth retaining wall, if the dilation is assumed to be ψ_s, the wedge moves at a velocity v at an angle $\theta - \psi_s$ to the horizontal and the full energy equation may be expressed as:

$$\begin{aligned} Fv = & \left[\frac{H^2\gamma}{2\tan\theta} + \hat{W}(\psi_s,\theta,l)\right] v\,[\tan(\theta-\psi_s)(1+k_v) + k_h] \\ & - \frac{\hat{C}(\psi_s,\theta,l)v\cos\psi_s}{\cos(\theta-\psi_s)} \end{aligned} \tag{4.67}$$

in which

$$\begin{aligned}\hat{C}(\psi_s,\theta,l) = {} & \frac{-\sigma_t}{\cos\psi_s}\left(\frac{m-1}{m+1}\right)\left(\frac{\gamma((1+k_v)\cos\alpha+k_h\sin\alpha)}{c_0}\right)^m \\ & \times[(\frac{n_0}{\gamma((1+k_v)\cos\alpha+k_h\sin\alpha)}+\Delta y\sin\alpha)^{m+1} \\ & -(\frac{n_0}{\gamma((1+k_v)\cos\alpha+k_h\sin\alpha)}+\Delta x\cos\alpha)^{m+1}] \\ & +a\cdot\frac{\sigma_t}{\cos\psi_s}(\Delta x\cos\alpha-\Delta y\sin\alpha)\end{aligned} \tag{4.68}$$

$$\begin{aligned}\frac{\hat{W}(\psi_s,\theta,l)}{\gamma} = {} & -n_1(\Delta x\cos\alpha-\Delta y\sin\alpha)+\frac{k_0}{m+1} \\ & \times\ [(\frac{n_0}{\gamma((1+k_v)\cos\alpha+k_h\sin\alpha)}+\Delta x\cos\alpha)^{m+1} \\ & -(\frac{n_0}{\gamma((1+k_v)\cos\alpha+k_h\sin\alpha)}+\Delta y\sin\alpha)^{m+1}] \\ & -\Delta y\cos\alpha(\Delta x\cos\alpha-\Delta y\sin\alpha)+0.5l^2\sin(\theta+\alpha)\cos(\theta+\alpha)\end{aligned} \tag{4.69}$$

These functions are straightforward to compute using a spreadsheet or computer program.

For linear mechanism analysis, considering $m = 1$, the non-linear yield function can be converted to the linear Mohr-Coulomb yield function. Especially, when $a = 0$, the backfill is cohesionless. The failure mechanism of cohesionless backfill is shown in Figure 4.9.

4.5.2 Comparison

To part evaluate the validity of the present method, comparisons are made between this work and the classic Mononobe-Okabe (Mononobe 1929) analysis. In order to get the closely linear solution with the current method, the non-linear coefficient m is assumed as 1.001 to represent the linear case. As shown in Table 4.3, it can be concluded the numerical results using the proposed method in this study are close to those of Mononobe-Okabe analysis, which gives confidence in the proposed method.

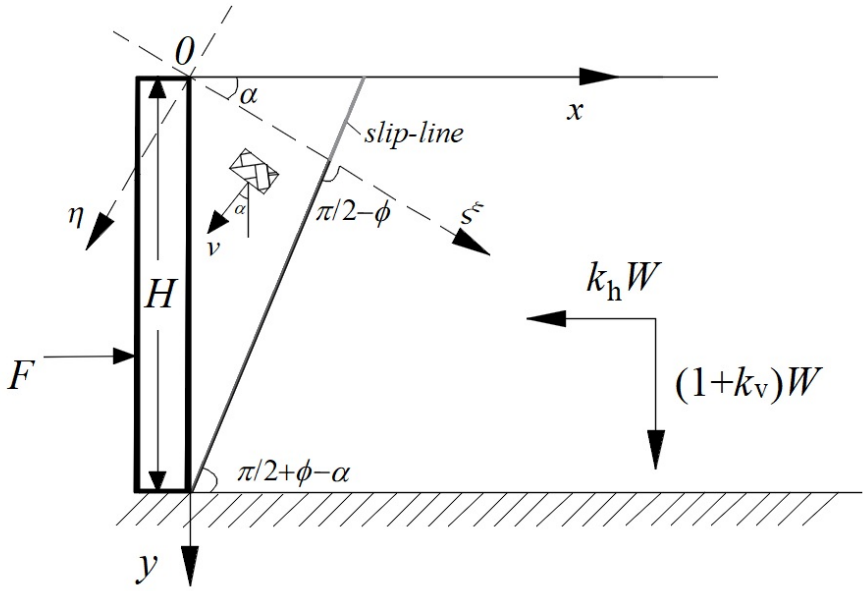

Figure 4.9: Linear active failure mechanism: pseudo-static analysis of retaining walls.

The present method based on non-linear power-law failure criterion should be verified by the existing research findings in this thesis. Table 4.4 presents values of seismic ($k_h = 0.1$) active earth pressures for $a = 1$, $\gamma = 18$ kN/m^3, $H = 4.0$ m, $c_0 = 9$ kPa and $\sigma_t = 20$ kPa, with the non-linear coefficient m varying from 1.2 to 2.0. The results calculated by Sun & Song (2016) and by Yang (2007) are also listed for comparison. It can be seen from Table 4.4 that the calculated pseudo-static active pressures are almost consistent with Sun and Song's and Yang's solutions and the absolute differences are small. This provides additional confidence that the present method is reliable for evaluating pseudo-static active pressures for soils with power-law failure criterion.

Furthermore, taking dense sand backfill as an example (properties given in Table 4.1), the results from the proposed variational method can be compared with those derived using the multi-tangent technique. Through the upper bound analysis in the previous section (Section 4.4.3), the normal stress distribution along failure surface can be predicted. Therefore, the minimum and maximum normal stresses can be determined (as the minimum and maximum normal stresses along failure

surface) in multi-tangent non-linear DLO analysis. For DLO analysis, the nodal density adopts 2000 nodes to generate a sufficiently accurate solution. From Table 4.5 and Table 4.6, it could be concluded that the results by different approaches are almost consistent. The failure mechanisms for dense sand predicted by different approaches are plotted, shown from Figure 4.10 to Figure 4.19. By comparisons in limit loads and failure mechanisms, it can be concluded that the multi-tangent non-linear DLO method using three-tangent analysis can generate similar results to those by variational method. The adopted tangents in the failure mechanism analysis are listed in Table 4.7.

It is well known that a one-wedge analysis of a pseudo static passive retaining wall problem (especially when the retaining wall is not smooth) gives very inaccurate results, therefore further study should be considered for multi-wedge analysis of a passive retaining wall. In the following chapter, a very simple case study for the passive failure analysis of retaining wall is conducted using multi-wedge analysis.

	ϕ	20°			30°		
	k_h	0	0.1	0.2	0	0.1	0.2
This study		0.490	0.568	0.671	0.333	0.396	0.473
Mononobe-Olabe (1929)		0.490	0.569	0.672	0.333	0.397	0.473

Table 4.3: Comparison in pseudo static active earth pressure coefficient with previous work ($m = 1.001$, $c_0 = 1$ kPa and $\sigma_t = (1/\tan\phi)$ kPa).

Coefficient m	1.2	1.4	1.6	1.8	2.0
This study (kN/m)	33.02	40.71	46.83	51.71	55.64
Sun and Song (2016) (kN/m)	34.35	42.04	49.32	55.13	59.96
Yang (2007) (kN/m)	32.66	39.78	45.61	50.39	54.32

Table 4.4: Comparison in pseudo static active earth pressure with previous work ($k_h = 0.1$, $k_v = 0$, $a = 1$, $\gamma = 18$ kN/m^3, $H = 4.0$ m, $c_0 = 9$ kPa and $\sigma_t = 20$ kPa).

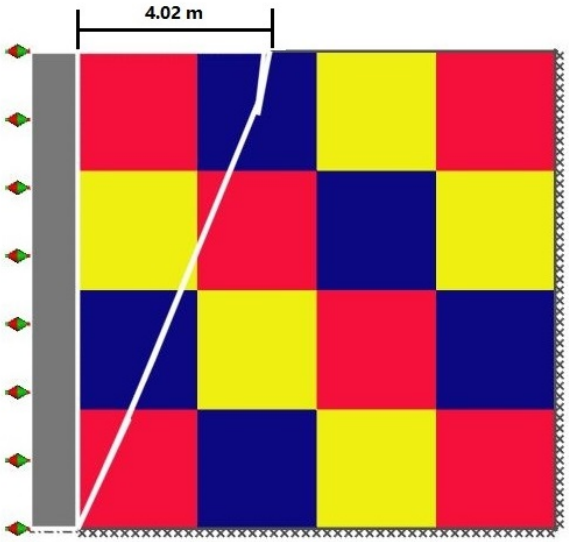

(a)

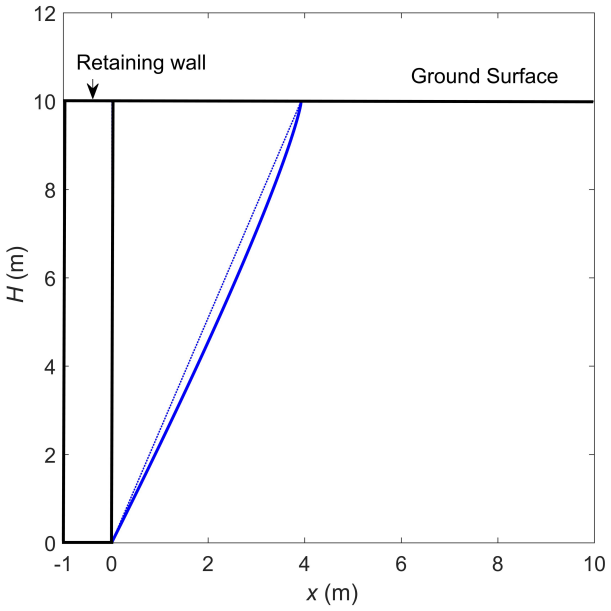

(b)

Figure 4.10: Case study for dense sand ($H = 10$ m, $q = 0$, $k_h = 0.05$, $k_v = 0$): (a) failure mechanism predicted by non-linear DLO method; (b) failure mechanism predicted by variational method.

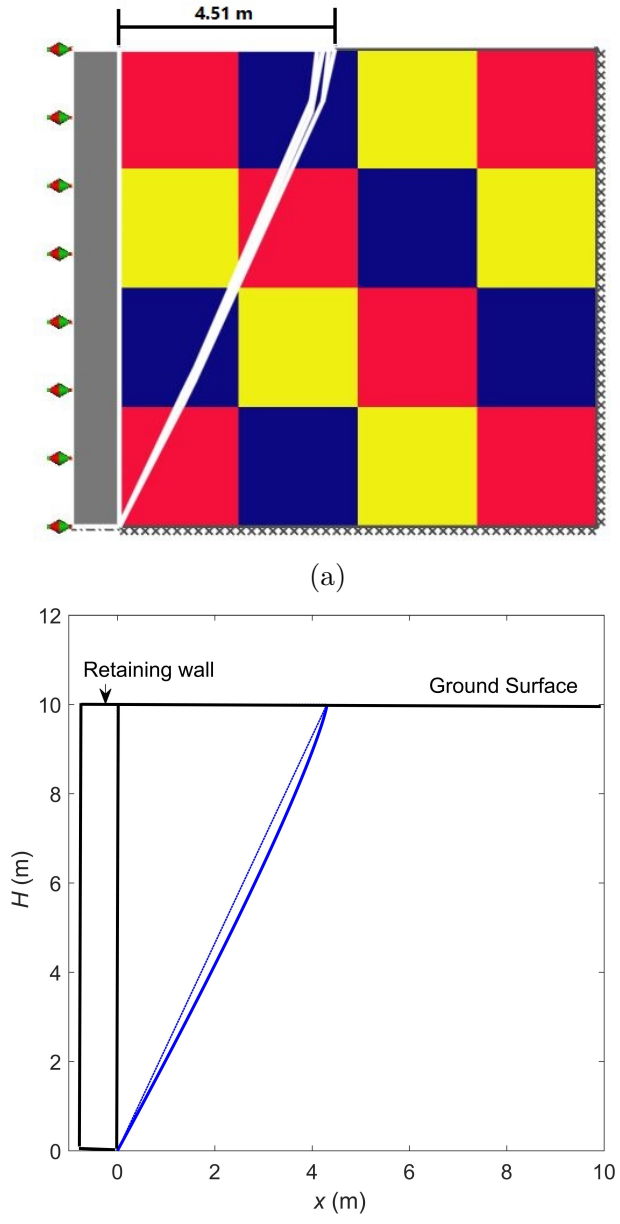

(a)

(b)

Figure 4.11: Case study for dense sand ($H = 10$ m, $q = 0$, $k_h = 0.1$, $k_v = 0$): (a) failure mechanism predicted by non-linear DLO method; (b) failure mechanism predicted by variational method.

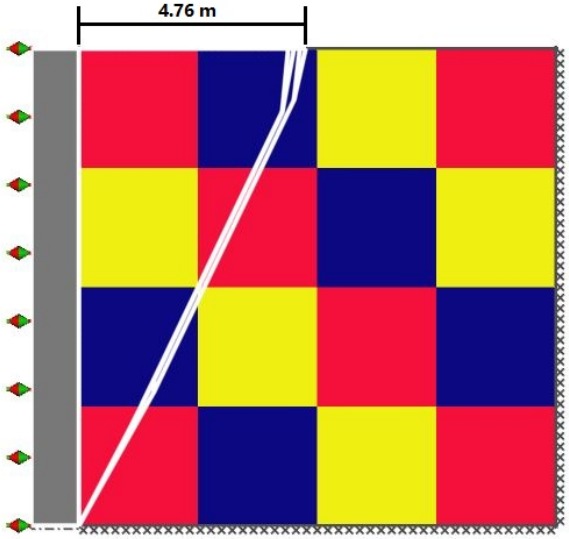

(a)

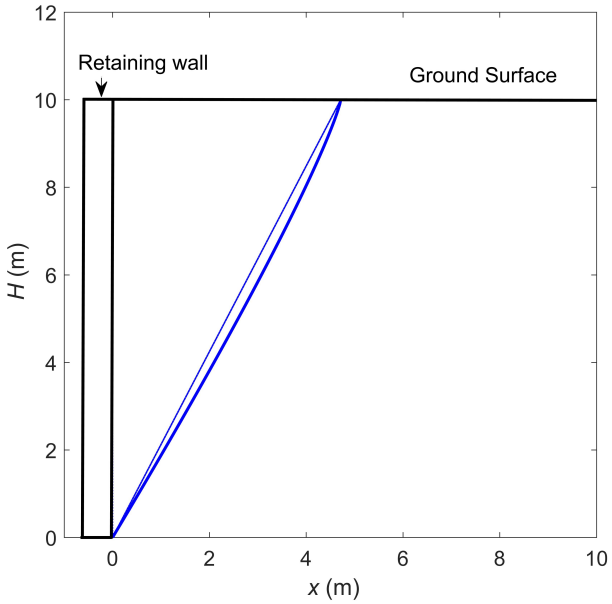

(b)

Figure 4.12: Case study for dense sand ($H = 10$ m, $q = 0$, $k_h = 0.15$, $k_v = 0$): (a) failure mechanism predicted by non-linear DLO method; (b) failure mechanism predicted by variational method.

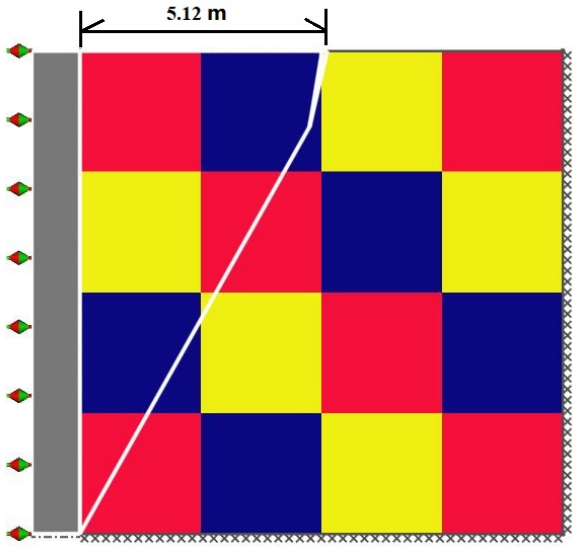

(a)

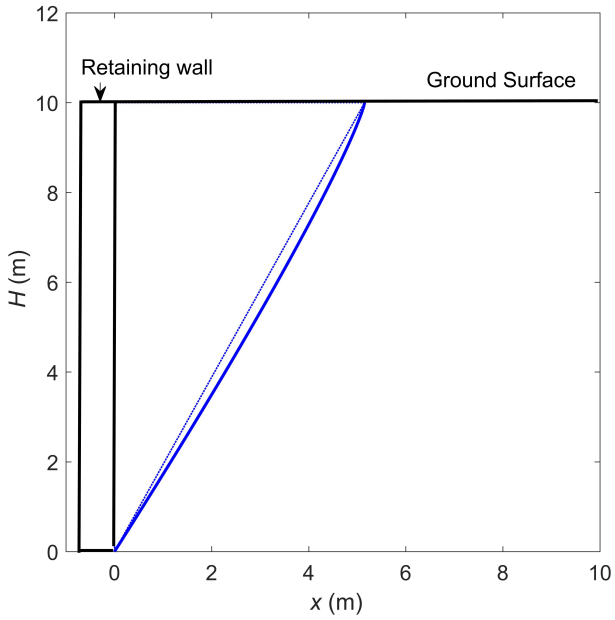

(b)

Figure 4.13: Case study for dense sand ($H = 10$ m, $q = 0$, $k_h = 0.2$, $k_v = 0$): (a) failure mechanism predicted by non-linear DLO method; (b) failure mechanism predicted by variational method.

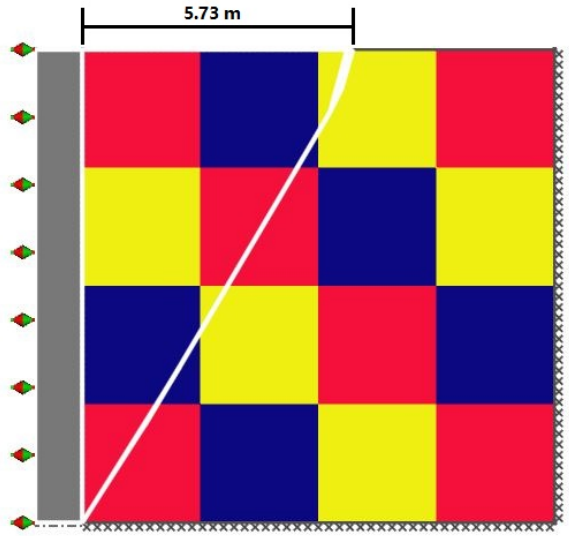

(a)

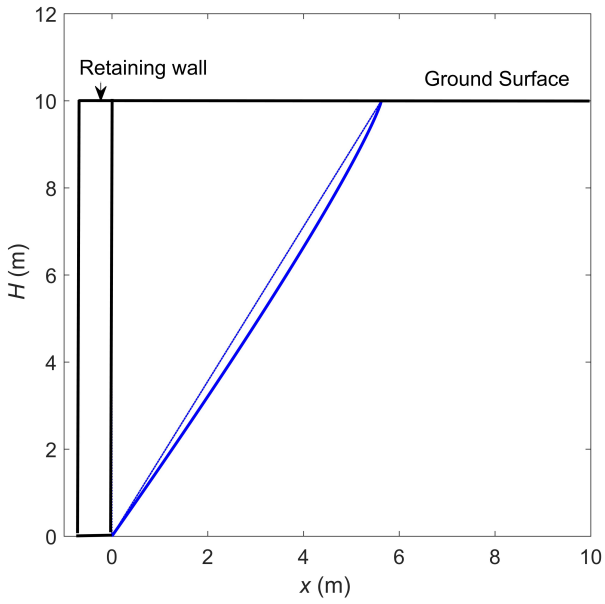

(b)

Figure 4.14: Case study for dense sand ($H = 10$ m, $q = 0$, $k_h = 0.25$, $k_v = 0$): (a) failure mechanism predicted by non-linear DLO method; (b) failure mechanism predicted by variational method.

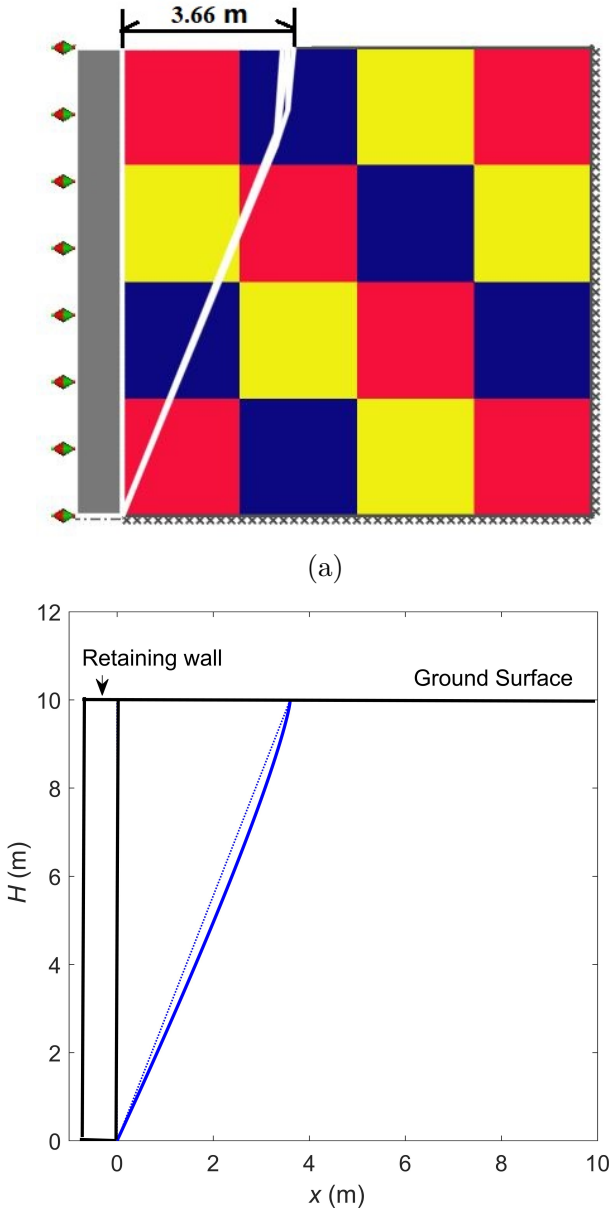

Figure 4.15: Case study for dense sand ($H = 10$ m, $q = 0$, $k_v = 0.1$, $k_h = 0$): (a) failure mechanism predicted by non-linear DLO method; (b) failure mechanism predicted by variational method.

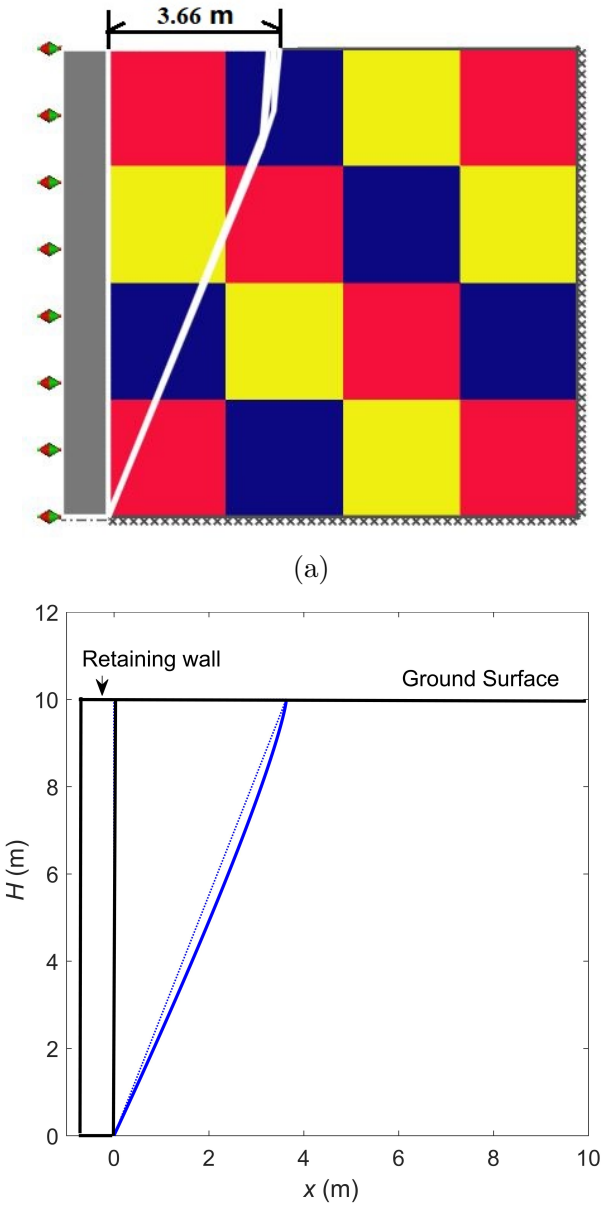

Figure 4.16: Case study for dense sand ($H = 10$ m, $q = 0$, $k_v = 0.2$, $k_h = 0$): (a) failure mechanism predicted by non-linear DLO method; (b) failure mechanism predicted by variational method.

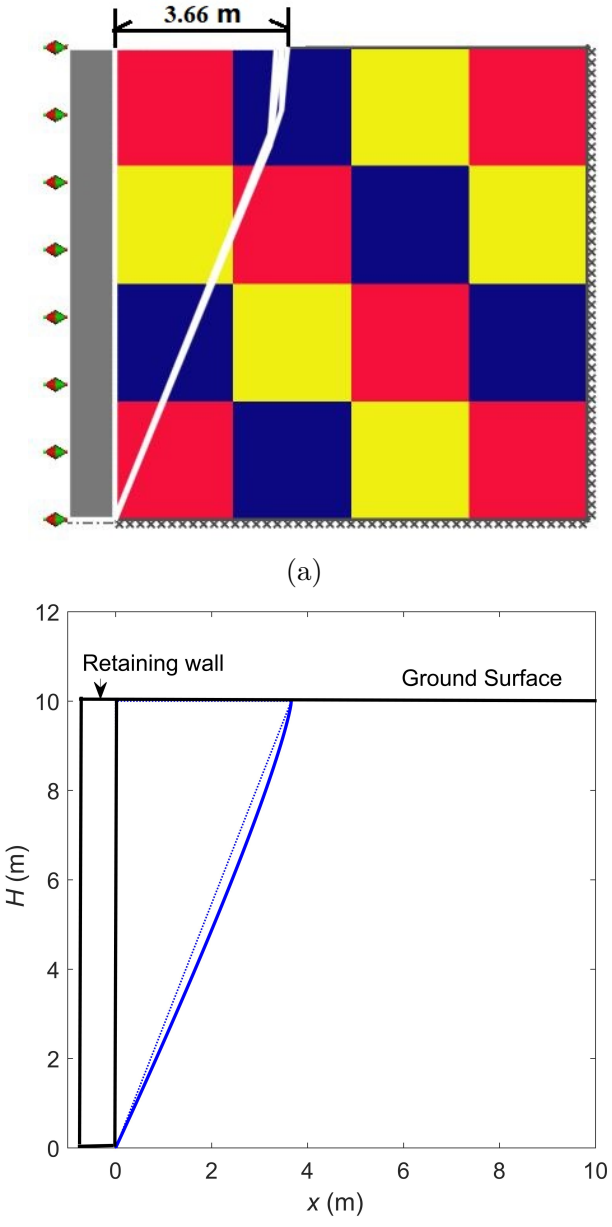

Figure 4.17: Case study for dense sand ($H = 10$ m, $q = 0$, $k_v = 0.3$, $k_h = 0$): (a) failure mechanism predicted by non-linear DLO method; (b) failure mechanism predicted by variational method.

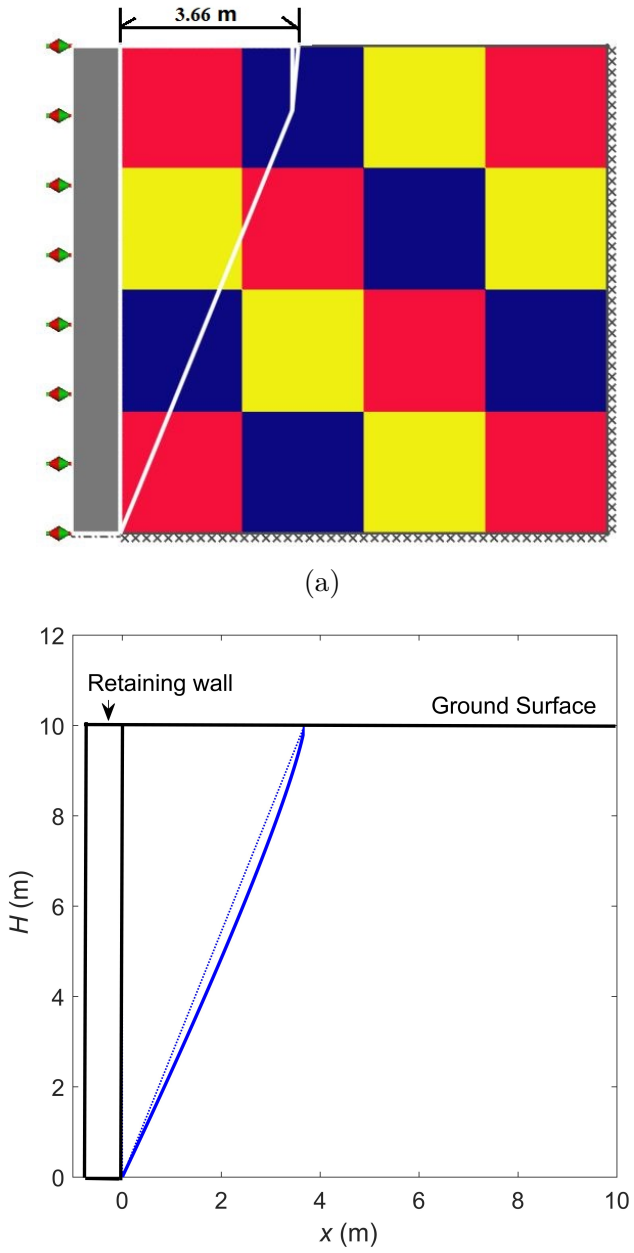

Figure 4.18: Case study for dense sand ($H = 10$ m, $q = 0$, $k_v = 0.4$, $k_h = 0$): (a) failure mechanism predicted by non-linear DLO method; (b) failure mechanism predicted by variational method.

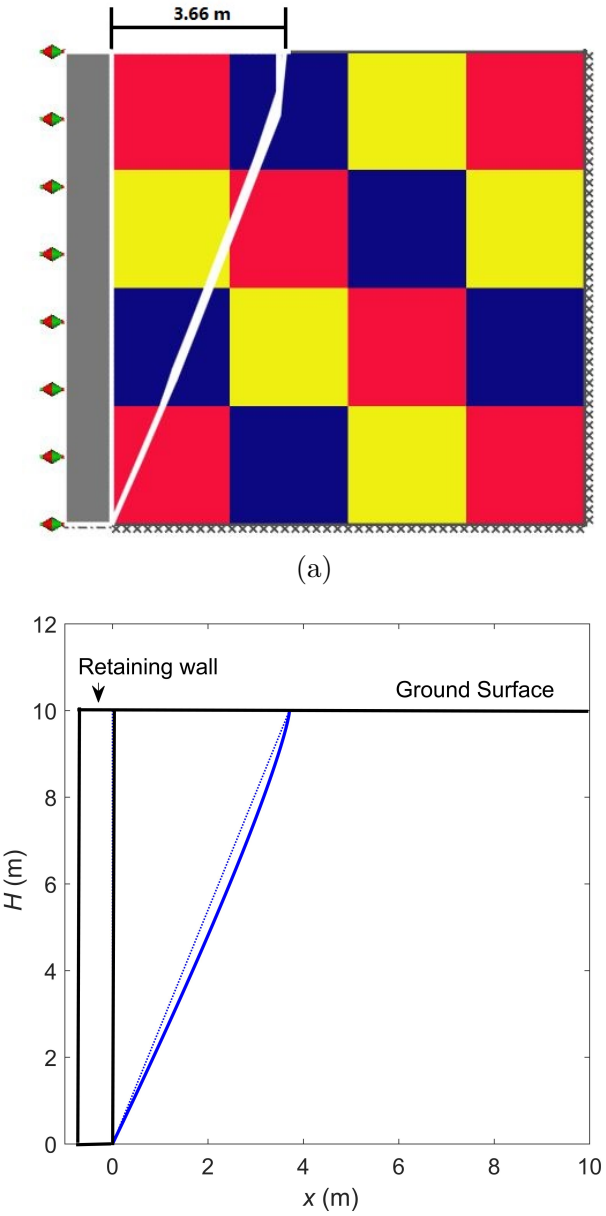

Figure 4.19: Case study for dense sand ($H = 10$ m, $q = 0$, $k_v = 0.5$, $k_h = 0$): (a) failure mechanism predicted by non-linear DLO method; (b) failure mechanism predicted by variational method.

Horizontal acceleration coefficients k_h	0.05	0.1	0.15	0.2	0.25
This study (kN/m)	110.07	126.72	144.87	164.66	186.20
Non-linear DLO method (kN/m)	108.00	125.00	143.00	162.00	184.00

Table 4.5: Comparison in pseudo static active earth pressure with different horizontal acceleration coefficients: dense sand case ($H = 10$ m, $q = 0$).

Vertical acceleration coefficients k_v	0.1	0.2	0.3	0.4	0.5
This study (kN/m)	106.23	117.81	129.57	141.49	153.56
Non-linear DLO method (kN/m)	104.00	116.00	127.00	139.00	151.00

Table 4.6: Comparison in pseudo static active earth pressure with different vertical acceleration coefficients: dense sand case ($H = 10$ m, $q = 0$).

4.6 Sensitivity Analysis

To investigate the influences of seismicity and parameters in the non-linear failure criterion on the active pressure, parametric studies are conducted with one example (the parameter set is from Yang (2007)): active earth pressure of soils (corresponding to $a = 1$, $\gamma = 18$ kN/m^3, $c_0 = 9$ kPa and $\sigma_t = 20$ kPa) on a vertical retaining wall ($H = 4.0$ m) with a horizontal backfill surface. For convenience, the case of the inclined backfill and retaining wall is not considered here. But there is no difficulty in principle in extending this methodology to deal with the case considering the variation of the inclined angle for backfill and retaining wall.

4.6.1 Effects of seismic acceleration coefficients

To investigate the influence of seismicity on the active pressure, more details of the effects of the seismic acceleration coefficients should be discussed. The values of normalized active thrust with non-linear coefficient m varying from 1.0 to 2.0 for $k_h = 0, 0.05, 0.1$ and $k_v = 0, 0.05, 0.1$ are illustrated in Figure 4.20 and Figure 4.21. Obviously, the increase of the value of horizontal seismic acceleration coefficient k_h leads to the increase of active pressure, which verifies the fact that the earthquakes have the unfavorable effect of increasing active pressure.

k_h	k_v	Parameter sets
0.05	0	$c_t = 0.0229$kPa,$\phi_t = 62.6803°$
		$c_t = 2.6466$kPa,$\phi_t = 47.8317°$
		$c_t = 4.9193$kPa,$\phi_t = 45.7372°$
0.10	0	$c_t = 0.0229$kPa,$\phi_t = 62.6803°$
		$c_t = 2.8185$kPa,$\phi_t = 47.6195°$
		$c_t = 5.2388$kPa,$\phi_t = 45.5241°$
0.15	0	$c_t = 0.0229$kPa,$\phi_t = 62.6803°$
		$c_t = 2.9939$kPa,$\phi_t = 47.4159°$
		$c_t = 5.5647$kPa,$\phi_t = 45.3198°$
0.20	0	$c_t = 0.0229$kPa,$\phi_t = 62.6803°$
		$c_t = 3.1731$kPa,$\phi_t = 47.2196°$
		$c_t = 5.8979$kPa,$\phi_t = 45.1229°$
0.25	0	$c_t = 0.0229$kPa,$\phi_t = 62.6803°$
		$c_t = 3.3569$kPa,$\phi_t = 47.0295°$
		$c_t = 6.2395$kPa,$\phi_t = 44.9322°$
0	0.10	$c_t = 0.0229$kPa,$\phi_t = 62.6803°$
		$c_t = 2.7348$kPa,$\phi_t = 47.7211°$
		$c_t = 5.0832$kPa,$\phi_t = 45.6262°$
0	0.20	$c_t = 0.0229$kPa,$\phi_t = 62.6803°$
		$c_t = 2.9926$kPa,$\phi_t = 47.4174°$
		$c_t = 5.5624$kPa,$\phi_t = 45.3212°$
0	0.30	$c_t = 0.0229$kPa,$\phi_t = 62.6803°$
		$c_t = 3.2509$kPa,$\phi_t = 47.1380°$
		$c_t = 6.0424$kPa,$\phi_t = 45.0409°$
0	0.40	$c_t = 0.0229$kPa,$\phi_t = 62.6803°$
		$c_t = 3.5095$kPa,$\phi_t = 46.8793°$
		$c_t = 6.5232$kPa,$\phi_t = 44.7817°$
0	0.50	$c_t = 0.0229$kPa,$\phi_t = 62.6803°$
		$c_t = 3.7686$kPa,$\phi_t = 46.6386°$
		$c_t = 7.0047$kPa,$\phi_t = 44.5405°$

Table 4.7: The optimal locations of tangent points in the failure mechanism analysis from Figure 4.10 to Figure 4.19.

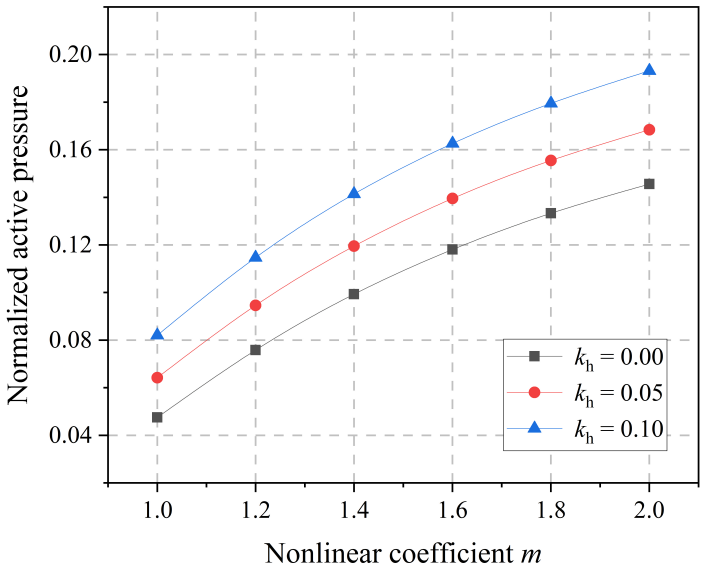

Figure 4.20: Influences of horizontal seismic acceleration coefficient k_h on normalized active pressures ($k_v = 0$, $a = 1$, $c_0 = 9$ kPa and $\sigma_t = 20$ kPa).

4.6.2 Effects of non-linear coefficient m

To explore how the earth pressures considering non-linear failure criterion will be different from those obtained by using MC criterion (i.e. $m = 1$), the effects of non-linear coefficient m on the active pressures are analyzed. The values of the seismic active pressures with non-linear coefficient m varying from 1.0 to 2.0 are illustrated in Figure 4.20 and Figure 4.21. It can be concluded that with increase of the non-linear coefficient m, the active thrust will increase.

4.6.3 Effects of normalisation stress c_0

To investigate the effects of normalisation stress c_0 on the active pressure, the values of the seismic active pressures with c_0 varying from 4 kPa to 12 kPa are illustrated in Figure 4.22. It can be concluded that with increase of the normalisation stress c_0, the active thrust will decrease.

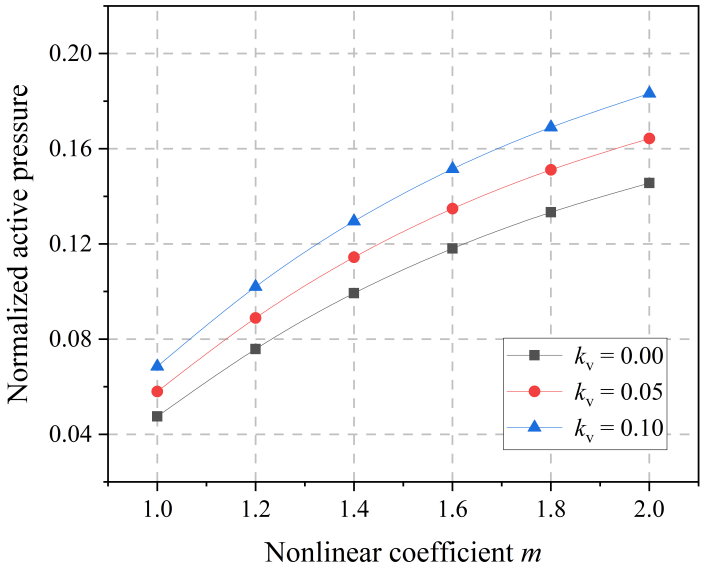

Figure 4.21: Influences of vertical seismic acceleration coefficient k_v on normalized active pressures ($k_h = 0$, $a = 1$, $c_0 = 9$ kPa and $\sigma_t = 20$ kPa).

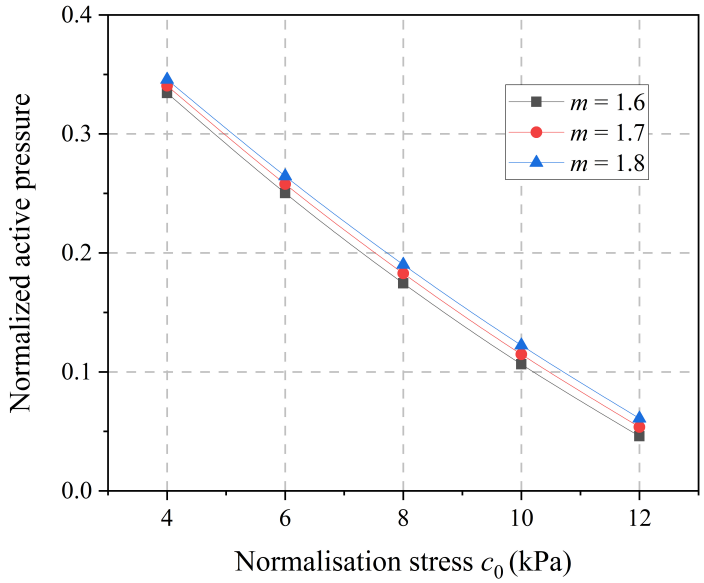

Figure 4.22: Influences of normalisation stress c_0 on normalized active pressures ($k_h = 0.05$, $k_v = 0$, $a = 1$ and $\sigma_t = 20$ kPa).

4.6.4 Effects of normalisation stress σ_t

The normalisation stress σ_t plays a key role in determination of the active pressure, the values of the seismic active pressures with σ_t varying from 20 kPa to 100 kPa are illustrated in Figure 4.23. It can be concluded that with increase of the normalisation stress σ_t, the active thrust will increase.

In order to explain the results in sensitivity analysis, the related yield surfaces should be plotted. The reason why the calculated active pressures with different non-linear coefficient m in Figure 4.22 (with the same value of c_0) and Figure 4.23 (with the same value of σ_t) are close can be explained by the related yield surfaces, as shown in Figure 4.24 and Figure 4.25. In Figure 4.24, it can be found that the difference between yield surfaces with different values of m but the same value of c_0 is small. In Figure 4.25, it can be found that the difference between yield surfaces with different values of m but the same value of σ_t is small.

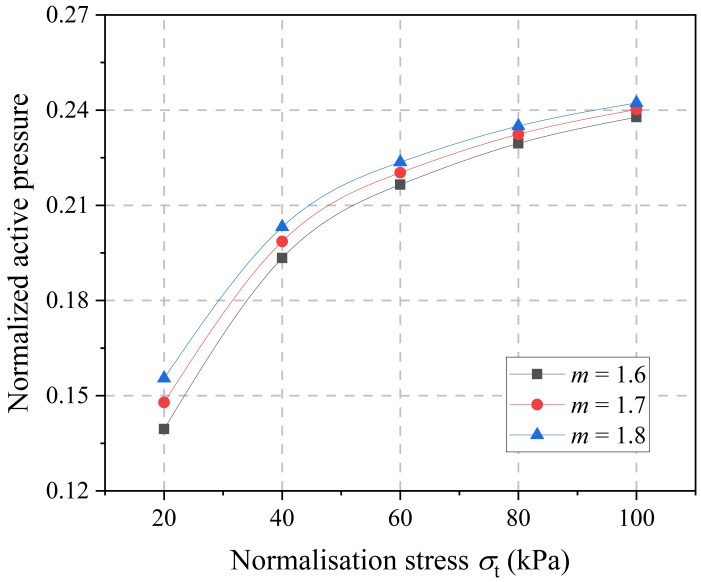

Figure 4.23: Influences of normalisation stress σ_t on normalized active pressures ($k_h = 0.05$, $k_v = 0$, $a = 1$, and $c_0 = 9$ kPa).

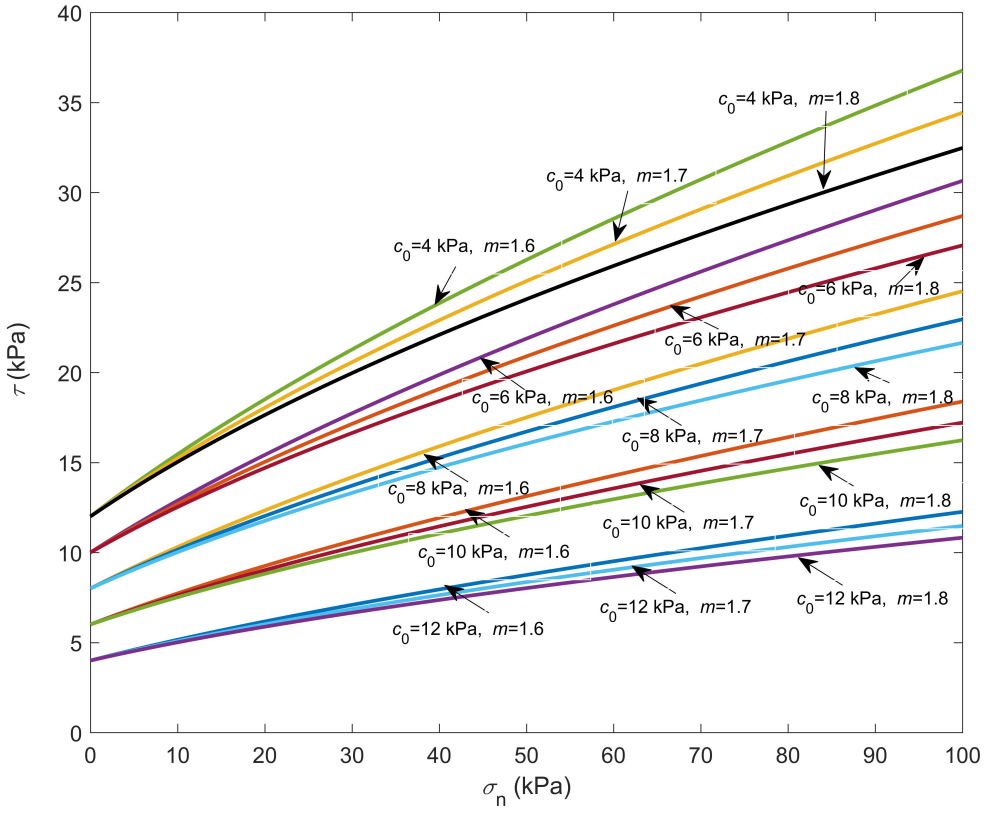

Figure 4.24: Influences of normalisation stress c_0 on yield surfaces ($k_h = 0.05$, $k_v = 0$, $a = 1$ and $\sigma_t = 20$ kPa).

4.7 Conclusions

1. A fully general variational approach for the upper bound analysis of geotechnical collapse mechanisms in non-linear soils has been presented.

2. The approach presented has significantly extended a methodology developed previously for the special case of deep tunnels and the anchor/trapdoor problem, and used full energy optimisation of the solution, rather than adopting a special boundary condition.

3. Application of the method to the analysis of active and passive earth pressures acting on a smooth retaining wall demonstrated that the single wedge solutions obtained gave results very close to a simple lower bound analysis and thus established a close bracket to the true plastic solution for this case.

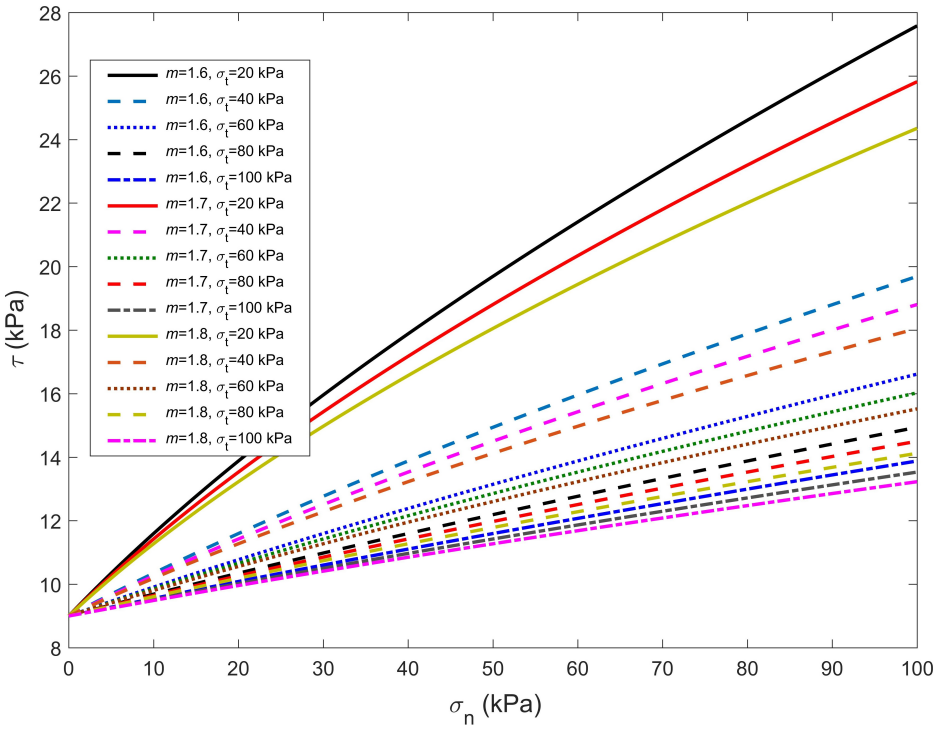

Figure 4.25: Influences of normalisation stress σ_t on yield surfaces ($k_h = 0.05$, $k_v = 0$, $a = 1$, and $c_0 = 9$ kPa).

4. Due to the non-linearity of the yield surface, for the simple types of solution utilised here, it is possible to determine the normal and shear stresses at any point on the slip-line. This is not normally available for upper bound problems. The validity of these stresses has been investigated and shows strong consistency with related lower bound solutions, but further work is required in this area to establish the validity of the values generated.

5. A further example addressing the retaining wall problem demonstrated that the proposed method can be applied considering the effects of horizontal and vertical acceleration coefficients by adjusting the external work rate.

6. The results from the proposed seismic variational procedure are validated by the existing published literature and the proposed multi-tangent non-linear DLO method.

Chapter 5

Application to multi-wedge problem

5.1 Introduction

In this chapter examples of how the proposed approach can deal with a multi-wedge analysis are given for (1) an anchor uplift problem and (2) a passive earth pressure against cohesive backfill problem. This work presents application of the variational approach for analysing translational upper bound problems using the classic multi-wedge rigid block upper bound kinematic method, based on curved slip-lines defined by closed form equations.

5.2 Two-wedge anchor problem

5.2.1 Linear analysis

A simple linear two-wedge example for an anchor pullout problem (after e.g., Murray & Geddes 1987) is shown in Figure 5.1.

The essence of the method is to determine the angle of dilation and energy dis-

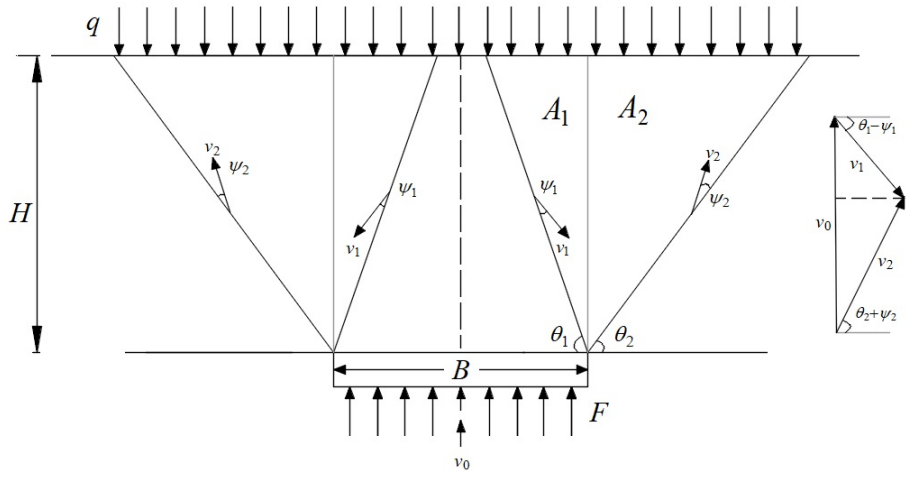

Figure 5.1: Simple two-wedge anchor analysis for a linear soil showing mechanism and hodograph.

sipation function for each slip-line. For a linear Mohr-Coulomb (c, ϕ) material of unit weight γ, the angle of dilation ψ is equal to the angle of friction ϕ for an upper bound analysis. The dissipation function for relative slip s parallel to the slip-line is cls where l is the slip-line length and $s = v\cos\psi$ where v is the relative velocity jump across the slip-line. The self weight external work for each wedge is computed by determining the dot product of the absolute velocity of a wedge and its self weight. This together with the hodograph leads to the following equations for the two-wedge anchor analysis.

$$\frac{v_0}{\sin(\theta_1 + \theta_2 - \psi_1 + \psi_2)} = \frac{v_1}{\sin(\pi/2 - \theta_2 - \psi_2)} = \frac{v_2}{\sin(\pi/2 - \theta_1 + \psi_1)} \tag{5.1}$$

$$v_{01} = v_1 \cdot \sin(\theta_1 - \psi_1) \tag{5.2}$$

$$v_{02} = v_2 \cdot \sin(\theta_2 + \psi_2) \tag{5.3}$$

where v_{01} and v_{02} are the values of v_1 and v_2 resolved parallel to v_0 with constraints

$$\psi_1 \geq \theta_1 - \pi/2 \tag{5.4}$$

$$\psi_2 \leq \pi/2 - \theta_2 \tag{5.5}$$

The force on the anchor can be determined from the following energy balance equation.

$$\begin{aligned} Fv_0 =& 2\left[W_{A2}v_{02} + (qHv_0/\tan\theta_2) - W_{A1}v_{01} + cl_2v_2\cos\psi_2 + cl_1v_1\cos\psi_1\right] \\ &+ \gamma HBv_0 + qBv_0 \end{aligned} \tag{5.6}$$

where W_{A1} and W_{A2} are the self-weight of the triangle wedges A_1 and A_2.

For a linear soil, the optimal solution is one for which $v_1 = 0$ and $\theta_2 = 90 - \phi$, giving the following equation for F:

$$\frac{F}{\gamma HB} = 1 + \frac{H}{B}\tan\phi + \frac{q}{\gamma H} + \frac{2q}{\gamma B}\tan\phi + \frac{2c}{\gamma B} \tag{5.7}$$

The aim of this section is to demonstrate how this form of mechanism analysis for linear Mohr-Coulomb materials can be extended to a material possessing a non-linear yield surface for translational mechanisms in a fully general way.

5.2.2 Non-linear analysis

Consider a two-wedge analysis for an anchor/trapdoor following the geometry shown in Figure 5.1 and adopting an anchor width $B = 5$m.

There are now four variables to be optimised, which are θ_1, θ_2, ψ_{s1} and ψ_{s2} . The hodograph and corresponding Eqs. (5.1) - (5.5) remain the same as for the linear case and Eq.(5.6) is extended to the following:

$$\begin{aligned} Fv_0 =& \gamma HBv_0 + qBv_0 + 2qHv_0/\tan\theta_2 + 2[W_{A2}\cdot v_{02} - \hat{W}(\psi_{s2},\theta_2,l_2)\cdot v_2 - W_{A1}\cdot v_{01} \\ &- \hat{W}(\psi_{s1},\theta_1,l_1)\cdot v_1 + \hat{C}(\psi_{s2},\theta_2,l_2)v_2\cos\psi_{s2} + \hat{C}(\psi_{s1},\theta_1,l_1)v_1\cos\psi_{s1}] \end{aligned} \tag{5.8}$$

where $l_1 = H/\sin\theta_1$ and $l_2 = H/\sin\theta_2$. W_{A1} and W_{A2} are the self-weight of the triangle wedges A_1 and A_2. $\hat{W}(\psi_{s1}, \theta_1, l_1)$ and $\hat{W}(\psi_{s2}, \theta_2, l_2)$ represent the corrections to the wedge weights above the slip-line 1 and slip-line 2, respectively. $\hat{C}(\psi_{s1}, \theta_1, l_1)$ and $\hat{C}(\psi_{s2}, \theta_2, l_2)$ represent the dissipation coefficients along the slip-line 1 and slip-line 2, respectively.

Parameter set	θ_1	ψ_{s1}	θ_2	ψ_{s2}	F_{upper}(kN/m)	F_{prev} (kN/m)
Cohesive frictional	any	any	60.00°	29.99°	655.28	655.29
Loose sand	any	any	57.00°	32.99°	675.05	675.05
Dense sand	any	any	43.78°	46.22°	878.51	879.45
Fractured rock	any	any	49.45°	40.55°	1188.40	1190.00

Table 5.1: Two-wedge anchor solutions for the case $q = 5$ kN/m^2, and $H = 5$m, using material properties from Table 4.1. F_{prev} are values computed using the approach of Fraldi & Guarracino (2009), for the non-linear soils and using Eq. 5.6 for the linear soils.

To illustrate the general behaviour, first a solution where all four parameters θ_1, θ_2, ψ_{s1} and ψ_{s2} are fixed is shown in Figure 5.2. Solutions were then investigated where the solution was optimised for all four parameters. However, it was found that the optimal solution was always that for which $\theta_2 + \psi_{s2} = \pi/2$, independent of the values of θ_1 and ψ_{s1} as shown in Table 5.1 for each of the soil types in Table 4.1. From the hodograph in Figure 5.1, v_1 must be zero if $\theta_2 + \psi_{s2} = \pi/2$ and $\theta_1 - \psi_{s1}$ can take any value. This agrees well with the linear case (e.g., Murray & Geddes 1987). There are no known non-linear lower bound solutions to the anchor problem. A linear lower bound solution was derived by Smith (1998) and gives an almost identical answer as the upper bound result in Eq. 5.6.

An illustration of the variation of the results for fixed $\theta_1 = 63.43°$and $\psi_{s1} = 20.0°$ with θ_2 and ψ_{s2} allowed to vary, is shown graphically in Figure 5.3 for the fractured rock case and shows there is one minimum solution. In Figure 5.3 the magenta dot represents the solution for $\theta_2 = 50°$ and $\psi_{s2} = 25°$ for fixed $\theta_1 = 63.43°$ and $\psi_{s1} = 20.0°$ corresponding to the mechanism in Figure 5.2.

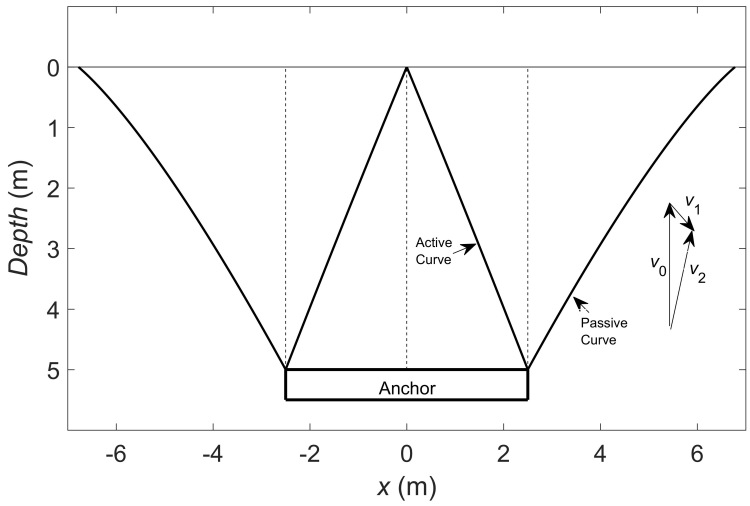

Figure 5.2: Example results of non-linear analysis showing mechanism and hodograph for two-wedge anchor embedded in fractured rock (properties given in Table 4.1) with $q = 5$ kN/m^2 and $H = 5$m. Active curves were selected to meet at the surface on the symmetry line and use a specified dilation angle: $\theta_1 = 63.43°$, $\psi_{s1} = 20°$. The passive curve used values $\theta_2 = 50°$ and $\psi_{s2} = 25°$. Predicted upper bound load $F = 2323.0$ kN/m^2.

The above examples clearly illustrate how the method may be applied to a general multiple-wedge rigid-block analysis, giving it a very broad applicability, and has verified it against lower bound and other solutions in the literature. Essentially, the method replicates the nature of a conventional linear soil analysis, but doubles the number of variables to be optimised (slip-line orientation and equivalent dilation on the slip-line), in cases where optimization is required. The examples shown that were of anchor uplift display similar characteristics to its linear counterpart. The optimal two-wedge anchor solution reduces to a single wedge solution.

The approach presented in this study determined the optimal upper bound by full application of the conventional energy minimisation approach. This is in contrast to some previous authors (e.g., Fraldi & Guarracino 2009, Fraldi & Guarracino 2010, Yang & Huang 2011) who adopted a partial optimization of energy minimisation to obtain a variational form of the slip-line, but then used a stress boundary condition

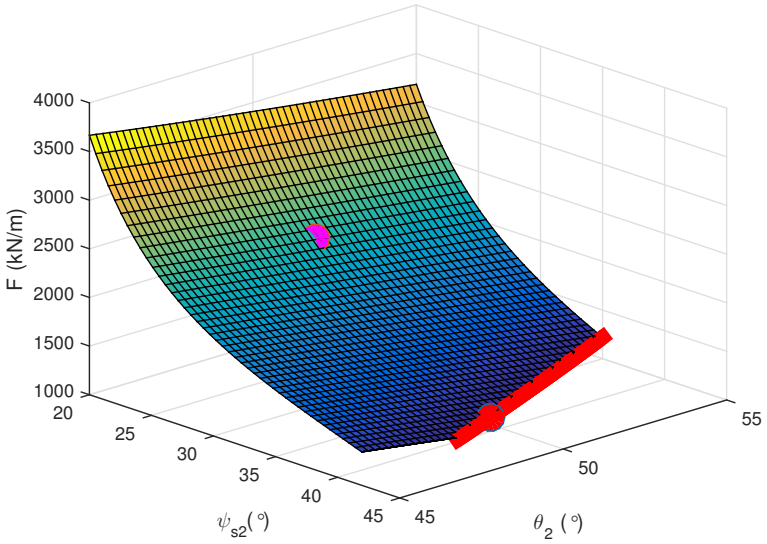

Figure 5.3: Variation of limit load F with fixed values of $\theta_1 = 63.43°$ and $\psi_{s1} = 20.0°$ for fractured rock case (properties given in Table 4.1) with $q = 5$ kN/m^2, $H = 5$m and $B = 5$m. The red line represents the kinematic limits of feasibility for the problem (Eq. 5.5). The optimal solution (red dot) lies on this line. At lower values of θ_2, the solution is limited by feasibility of the non-linear solution. The magenta dot represents the solution depicted in Figure 5.2 for $\theta_2 = 50°$ and $\psi_{s2} = 25°$.

.

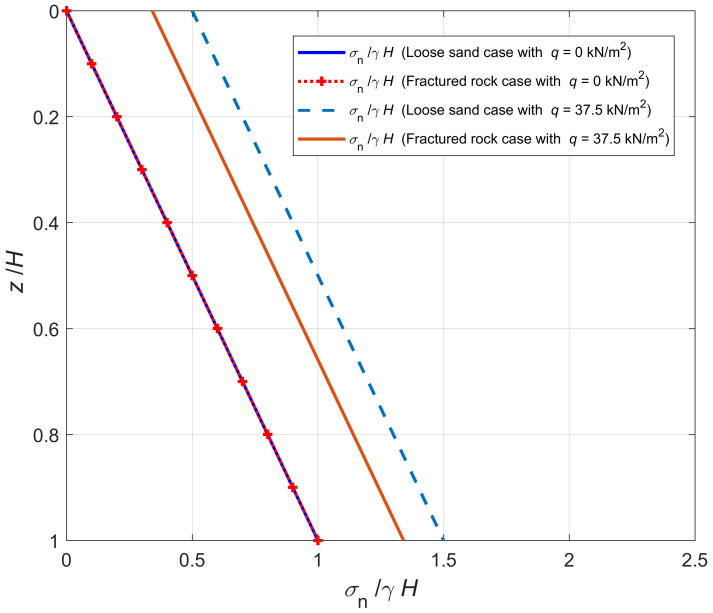

Figure 5.4: Predicted upper bound (UB) normalised normal stress for anchor with different surcharge loads ($H = 5$m).

at the soil surface to complete the solution. This assumed that the slip-line had to meet the (horizontal) surface at an angle consistent with a simple active or passive Rankine stress state at the surface. Solutions invoking such a boundary condition are still valid upper bounds, but were found to give collapse loads approx. 0.3% higher than the full minimization approach used in this study as shown in Table 5.1. While this boundary condition assumption may be valid for the smooth retaining wall problem, it does not hold universally. The proposed upper bound approach (discussed in Section 4.4.3) also shows the ability to predict the normal stress along the failure slip-line for the anchor problem. As shown in Figure 5.4, the predicted normal stress distribution along the failure slip-line (by the proposed upper bound approach) follows a value $\sigma_n = q + 1.0\gamma z$ (z is the depth), and the result provides a feasible normal stress distribution prediction for the multi-tangent non-linear analysis in the following section.

5.2.3 Verification of DLO results against the variational solutions

In order to validate the variational approach mentioned above, the limit loads predicted by the proposed variational method are compared with those by the multi-tangent non-linear DLO method. For convenience, the limit load is used in its dimensionless form: $F/\gamma HB$. With reference to non-linear failure criterion, analysis is conducted by comparing 3-line DLO solution (modelling by three tangents) and 4-line DLO solution (modelling by four tangents) to explore the optimum solutions. The effects of embedment ratio (H/B) and surcharge load ratio ($q/B\gamma$) on limit load are discussed for two examples: dense sand and fractured rock. It can be concluded that the gap between 3-line DLO solution and 4-line DLO solution is small (the difference is less than 1%). The solution by the proposed multi-tangent non-linear DLO solution is close to the variational solution, as shown in Figure 5.5 and Figure 5.6. As demonstrated in the previous section, the 3-line DLO solution is an efficient and accurate result.

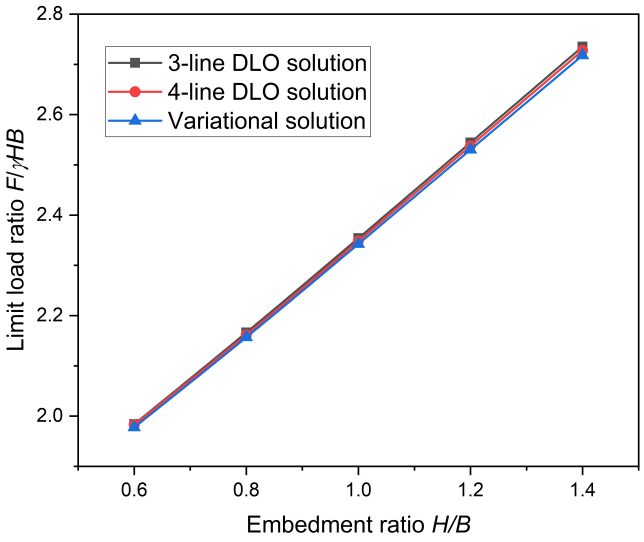

(a)

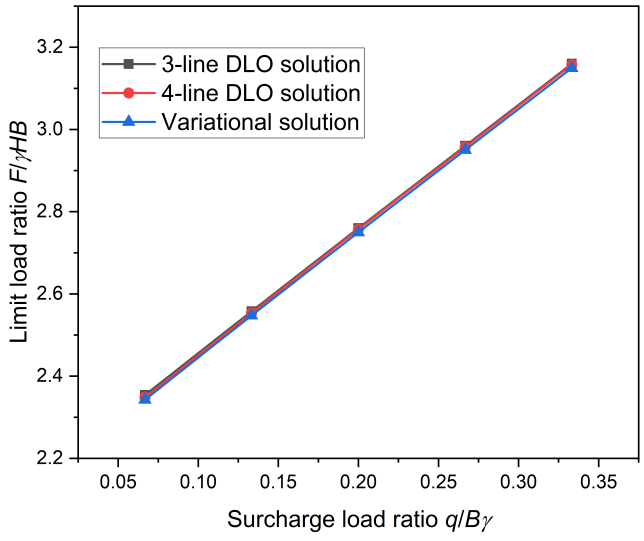

(b)

Figure 5.5: Case study for dense sand: (a) influence of embedment ratio on limit load ratio with non-linear failure criterion; (b) influence of surcharge load ratio on limit load ratio with non-linear failure criterion.

The failure mechanism of an anchor embedded in fractured rock (for the case $q = 5$ kN/m^2 and $H = 5$m) is shown in Figure 5.7: the failure slip-line tends to be slightly curved. For this modelling, the non-linear yield function used in DLO analysis was represented by three linear bounding surfaces.

5.3 Passive earth pressure against a cohesive backfill

5.3.1 Failure mechanism analysis based on variational method

The passive earth pressure problem against a cohesive backfill is analyzed in this section. In this case two slip-lines were modelled using a non-linear yield function, the wall interface as an almost linear frictionless interface and the slip-line through the backfill as an almost linear cohesive soil. The aim is to investigate the predicted stress distributions along the slip-lines. The hodograph is shown in Figure 5.8 and corresponding equations are extended to the following:

$$\frac{v_0}{\cos(\theta_2 + \psi_{s2} - \psi_{s1})} = \frac{v_{ac}}{\sin(\theta_2 + \psi_{s2})} = \frac{v_{bc}}{\cos\psi_{s1}} \tag{5.9}$$

$$\begin{aligned} Fv_0 =& W_{B1} \cdot v_{ac}\cos\psi_{s1} + \hat{W}(\psi_{s1}, \theta_1, l_1) \cdot v_{ac}\cos\psi_{s1} - \hat{W}(\psi_{s2}, \theta_2, l_2) \cdot v_{ac}\cos\psi_{s1} \\ &+ W_{B2} \cdot v_{ac}\cos\psi_{s1} - \hat{C}(\psi_{s1}, \theta_1, l_1)v_{ac}\cos\psi_{s1} + \hat{C}(\psi_{s2}, \theta_2, l_2)v_{bc}\cos\psi_{s2} \end{aligned} \tag{5.10}$$

where $l_1 = H/\sin\theta_1$ and $l_2 = H/\sin\theta_2$. W_{B1} and W_{B2} are the self-weight of the wedge between the secant of slip-line 1 and wall interface and wedge Δabc, respectively. $\hat{W}(\psi_{s1}, \theta_1, l_1)$ and $\hat{W}(\psi_{s2}, \theta_2, l_2)$ represent the corrections to the wedge weights above the slip-line 1 and slip-line 2, respectively. $\hat{C}(\psi_{s1}, \theta_1, l_1)$ and $\hat{C}(\psi_{s2}, \theta_2, l_2)$ represent the dissipation coefficients along the slip-line 1 and slip-line 2, respectively.

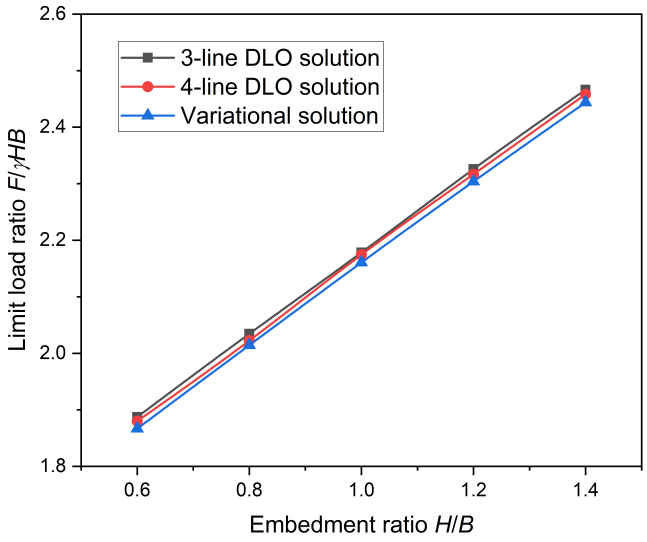

(a)

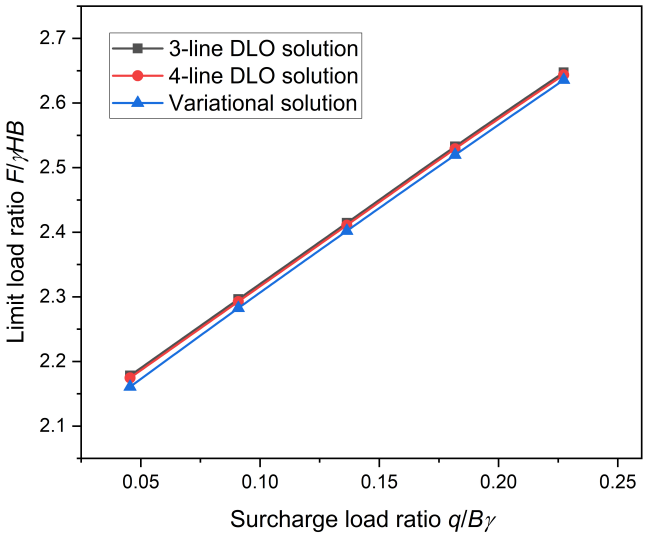

(b)

Figure 5.6: Case study for fractured rock: (a) influence of embedment ratio on limit load ratio with non-linear failure criterion; (b) influence of surcharge load ratio on limit load ratio with non-linear failure criterion.

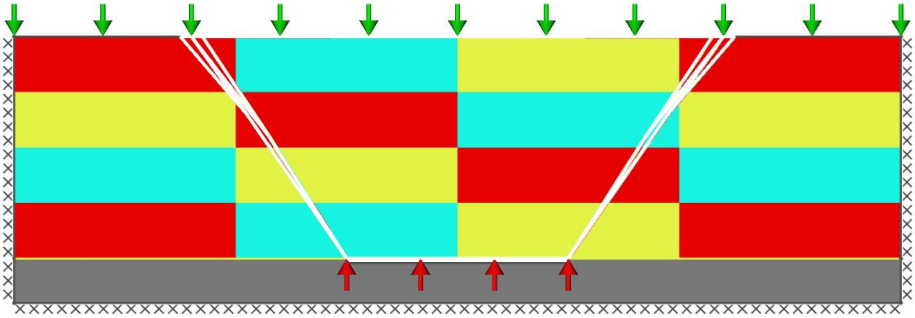

Figure 5.7: Predicted DLO failure mechanism for anchor ($q = 5\text{kN/m}^2$ and $H = 5\text{m}$): fractured rock case.

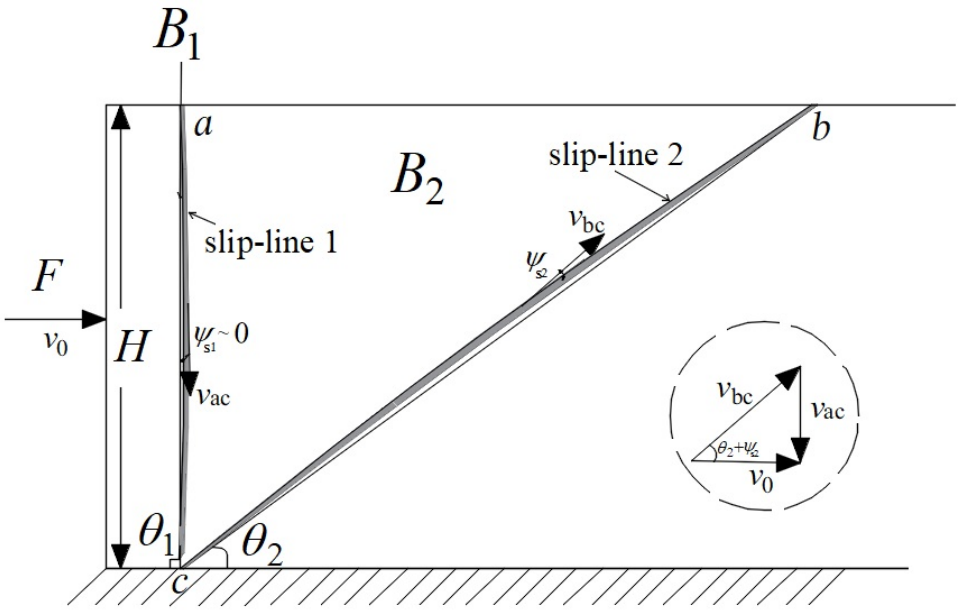

Figure 5.8: Passive failure mechanism and hodograph.

In order to model the smooth retaining wall against a cohesive backfill, the properties of the slip-lines should be determined first. Slip-line 1 is used to represent the vertical smooth retaining wall interface, shown in Figure 5.8. Based on initial assumptions, θ_1 can be taken as $\pi/2$ and the global dilation for slip-line 1 should be slightly higher than zero ($\psi_{s1} = 0.1°$) due to the non-linear approximation. For simplicity, take $\gamma_1 = 0$ kN/m^3 (γ_1 is the unit weight of wedge B_1) since area between wall interface and slip-line 1 is negligible. The frictionless wall interface is represented by a cohesive material with a low cohesion ($c_{01} \cdot a_1 = 0.1$ kN/m^2): $c_{01} = 0.1$ kN/m^2, $\sigma_{t1} = 100$ kN/m^2, $m_1 = 1.001$, $a_1 = 1$, $H = 5$ m. Therefore,

the terms W_{B1} and $\hat{W}(\psi_{s1}, \theta_1, l_1)$ in Eq. (5.10) should be zero. And the term $\hat{C}(\psi_{s1}, \theta_1, l_1) = -a_1 \cdot \sigma_{t1} H \tan \psi_{s1}$.

From Eq. 4.13:

$$\hat{C}(\psi_{s2}, \theta_2, l_2) = \frac{k_{02}\gamma_2 \cos\alpha_2}{\cos\psi_{s2}} \left(\frac{m_2 - 1}{m_2 + 1}\right) [(\frac{n_{02}}{\gamma_2 \cos\alpha_2} - \Delta y_2 \sin\alpha_2)^{m_2+1} - (\frac{n_{02}}{\gamma_2 \cos\alpha_2} - \Delta x_2 \cos\alpha_2)^{m_2+1}] + a_2 \cdot \frac{\sigma_{t2}}{\cos\psi_{s2}} (\Delta x_2 \cos\alpha_2 - \Delta y_2 \sin\alpha_2) \tag{5.11}$$

in which

$$k_{02} = \frac{\sigma_{t2}}{c_{02}^{m_2}} (\gamma_2 \cos\alpha_2)^{m_2 - 1} \tag{5.12}$$

$$\Delta x_2 = l_2 \cos\theta_2 \tag{5.13}$$

$$\Delta y_2 = l_2 \sin\theta_2 \tag{5.14}$$

$$\alpha_2 = \pi/2 - \theta_2 - \psi_{s2} \tag{5.15}$$

From Eq. 4.14 and Eq. 4.23:

$$\frac{\hat{W}(\psi_{s2}, \theta_2, l_2)}{\gamma_2} = \frac{k_{02}}{m_2 + 1} [(\frac{n_{02}}{\gamma_2 \cos\alpha_2} - \Delta x_2 \cos\alpha_2)^{m_2+1} - (\frac{n_{02}}{\gamma_2 \cos\alpha_2} - \Delta y_2 \sin\alpha_2)^{m_2+1}] + n_{12}(\Delta x_2 \cos\alpha_2 - \Delta y_2 \sin\alpha_2) + \Delta y_2 \cos\alpha_2 (\Delta x_2 \cos\alpha_2 - \Delta y_2 \sin\alpha_2) - 0.5 {l_2}^2 \sin\psi_{s2} \cos\psi_{s2} \tag{5.16}$$

The functions are straightforward to compute using a spreadsheet or computer program. The variables n_{02} and n_{12} can be determined straightforwardly numerically using standard root finding algorithms developed in the previous chapter.

5.3.2 Sensitivity analysis for the cohesive backfills

The property of slip-line 1 can be easily determined based on the assumption for smooth retaining wall problem. But the property of slip-line 2 can be explored since the different parameter sets lead to different results. The effects of non-linear coefficient m_2, normalisation stress c_{02} and σ_{t2} on the lateral earth pressure are investigated first. The parametric study is conducted to demonstrate how to choose the parameters to represent the property of the cohesive backfill in the proposed multi-wedge variational method. A linear analysis by the DLO method was used to validate the proposed two-wedge analysis. For convenience, the cohesion of the backfill c_u in DLO analysis is equal to c_{02} in the non-linear multi-wedge analysis. The other geometric parameter ($H = 5$ m) and backfill properties (i.e., $\gamma_2 = 20$ kN/m^3) are the same. Figure 5.9 shows the comparison in lateral earth pressure between two-wedge variational solution and the DLO solution. It can be concluded that the solutions using non-linear coefficient $m_2 = 1.001$ are almost consistent with those using $m_2 = 1.0001$. When c_{02} is fixed, the two-wedge variational solution will decrease with increase of σ_{t2}. When σ_{t2} is fixed, the two-wedge variational solution will increase with increase of c_{02}, shown in Figure 5.10. The differences between solutions using non-linear coefficient $m_2 = 1.001$ and those using $m_2 = 1.0001$ are very small. It can be concluded that the smaller value of c_{02}/σ_{t2}, the predicted earth pressure is closer to the DLO solution. This can be explained by the adopted yield surfaces determined by different groups of parameters used in Figure 5.9. As shown in Figure 5.11, if the yield surface described by power-law failure criterion is closer to the yield surface of cohesive soil, the predicted earth pressure is closer to the DLO solution based on the true linear yield surface. Due to the efficiency of the proposed standard root finding algorithms, the computation time will be longer if the m_2 is smaller since the feasible range for searching optimal solution is narrower. Therefore, the proposed variational approach adopts $m_2 = 1.001$ for the multi-wedge smooth retaining wall problem in this thesis. As shown in Figure 5.12, the predicted yield surfaces with $c_{02}/\sigma_{t2} = 1/500$ and $c_{02}/\sigma_{t2} = 1/600$ are

quite close to the linear yield surface when $m_2 = 1.001$. Therefore, the non-linear analysis adopts $c_{02}/\sigma_{t2} = 1/500$ and $c_{02}/\sigma_{t2} = 1/600$ for the multi-wedge smooth retaining wall problem in this thesis.

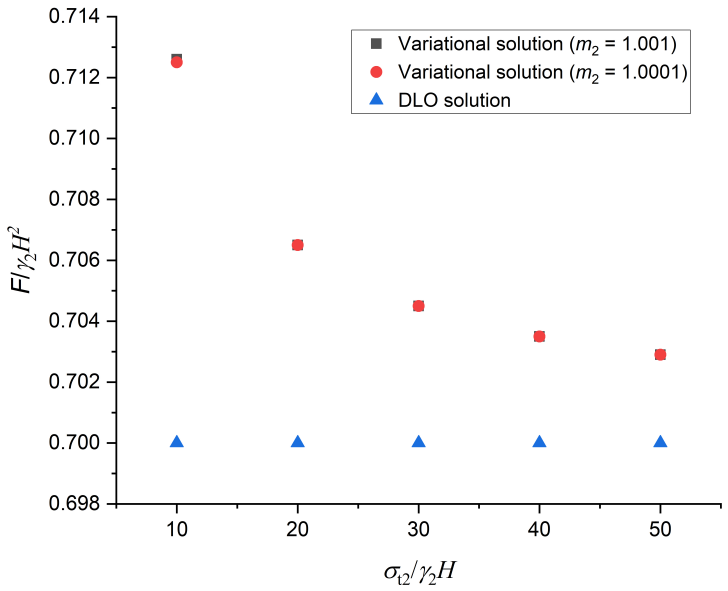

Figure 5.9: Comparison in lateral earth pressure with varying σ_{t2} ($c_{02}/\gamma_2 H = 0.1$, $a_2 = 1$).

5.3.3 Comparison

Based on the sensitivity analysis, one group of parameters describing cohesive backfill is adopted for the prediction of lateral earth pressure and stress distributions: $c_{02} = 50$ kN/m^2, $\sigma_{t2} = 30000$ kN/m^2, $\gamma_2 = 20$ kN/m^3, $m_2 = 1.001$, $a_2 = 1$. The predicted stresses along the two slip-lines are given in Figure 5.13. Since the slip-line 1 can be taken as the interface between the vertical wall and the cohesive backfill, the normal stress distribution should be consistent with the horizontal stress distribution along the smooth retaining wall.

According to the Rankine's theory, the effective minimum principal stress σ_3 is vertical stress σ_v and the effective maximum principal stress σ_1 is horizontal stress

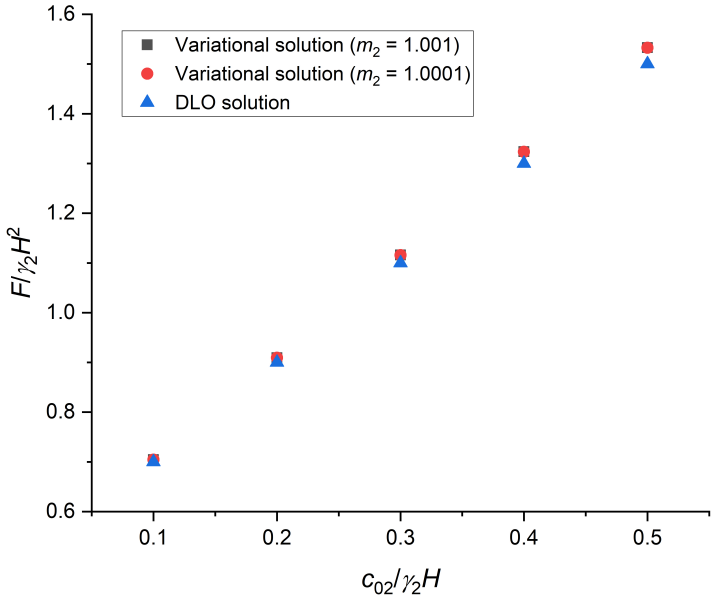

Figure 5.10: Comparison in lateral earth pressure with varying c_{02} ($\sigma_{t2}/\gamma_2 H = 30$, $a_2 = 1$).

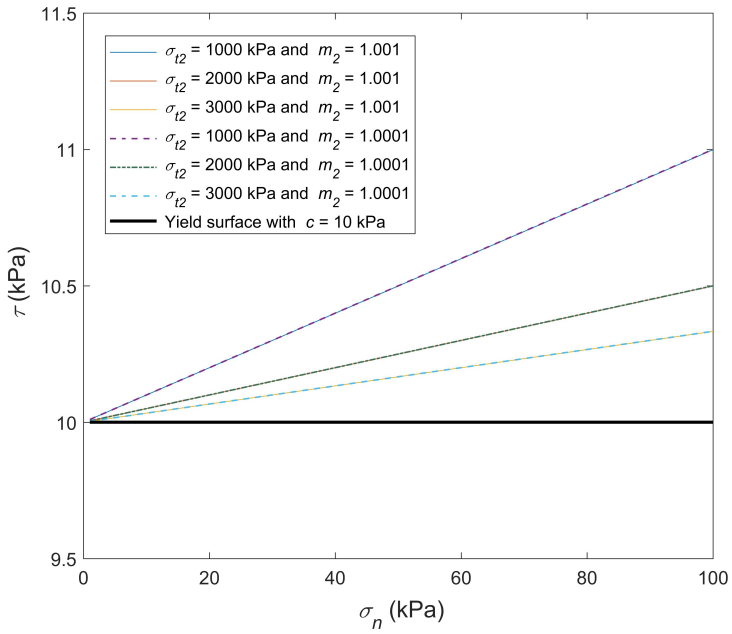

Figure 5.11: The yield surfaces determined by the parameter sets used in Figure 5.9 ($c_{02} = 10$ kN/m^2, $a_2 = 1$).

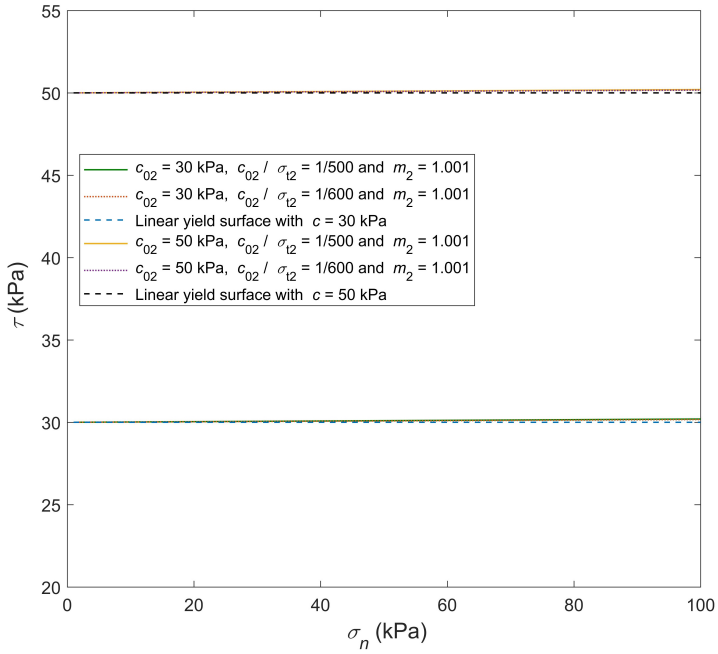

Figure 5.12: The yield surfaces determined by the parameter sets with varying c_{02}/σ_{t2}.

σ_h in passive case, shown in Figure 5.14.

In passive case, the horizontal stress distribution along the wall interface could be expressed as following:

$$\sigma_1 = \sigma_h = \gamma z + 2c \tag{5.17}$$

where γ is the unit weight, z is the depth and c is the cohesion of the backfill.
The vertical stress distribution along the wall interface could be expressed as following:

$$\sigma_3 = \sigma_v = \gamma z \tag{5.18}$$

Referring to Figure 5.14, the point where the Mohr's circle touches the failure surface is the yielding point and its normal stress value should be around $(\sigma_1+\sigma_3)/2$

(at failure state). Hence the normal stress distribution along the failure slip-line (slip-line 2) could be stated as:

$$\sigma_n = \gamma z + c \tag{5.19}$$

The overall lateral earth pressure is:

$$F = 0.5\gamma H^2 + 2cH \tag{5.20}$$

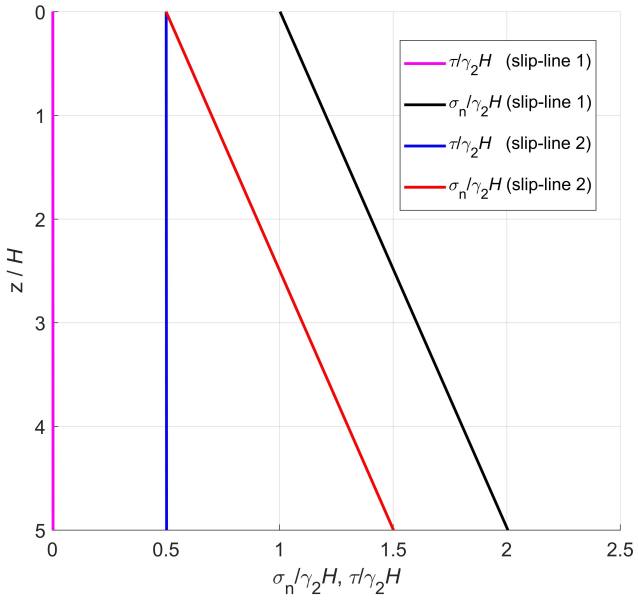

Figure 5.13: Predicted normalised normal and shear stresses with depth z on two non-linear slip-lines for the passive retaining wall problem. The passive failure slip-line used values $\theta_2 = 44.9774°$ and $\psi_{s2} = 0.0954°$. The predicted upper bound load $F = 751.23$ kN/m^2. The load by Rankine theory is $F = 750.00$ kN/m^2.

It could be concluded that the predicted stress distributions along failure slip-line by the proposed two-wedge analysis agree well with Rankine theory. For real clay soils, the strength varies from 10 kPa to 150 kPa, the unit weight γ_2 can vary

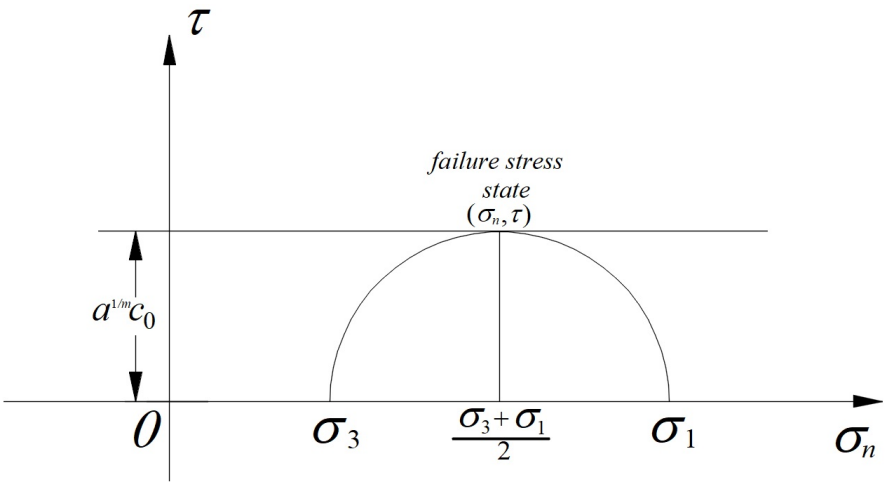

Figure 5.14: Passive stress state behind a smooth retaining wall.

Cohesion of backfill $c_{02}/\gamma_2 H$	$F/\gamma_2 H^2$ (this work)	$F/\gamma_2 H^2$ (Rankine theory)	$F/\gamma_2 H^2$ (DLO)
0.1	0.7029	0.7000	0.7000
0.2	0.9030	0.9000	0.9000
0.3	1.1030	1.1000	1.1000
0.4	1.3031	1.3000	1.3000
0.5	1.5031	1.5000	1.5000
1.0	2.5034	2.5000	2.5000
4.0	8.5080	8.5000	8.5000

Table 5.2: Two-wedge normalized lateral earth pressure solutions for the case $c_{02}/\sigma_{t2} = 1/500$, $m_2 = 1.001$.

from 18 kN/m^2 to 21 kN/m^2. The gravity wall height always varies from 2 m to 5 m. Therefore, the feasible magnitude of the parameter $c_{02}/\gamma_2 H$ might vary from 0.1 to 4 in real engineering problems. The comparisons in earth pressures among different approaches are shown in Table 5.2. When $c_{02}/\sigma_{t2} = 1/500$, the differences in the results between different methods are very small. Based on the conclusions from sensitivity analysis, the numerical results are more accurate when the value of c_{02}/σ_{t2} is smaller.

5.4 Discussion

The kinematic analysis of the anchor and passive retaining wall problem in the previous section has shown how to extend the one-wedge analysis to a two-wedge analysis and to determine the stress distribution along the slip-lines. For example, the case study for a cohesive soil backfill against retaining structure is discussed in this section. Figure 5.13 shows that shear stresses along the soil/wall interface and failure surface are both constant. The prediction satisfies the failure criterion for a cohesive soil since the properties of two slip-lines (given in the previous section) are represented by the cohesive materials (the shear strength τ is only determined by the cohesion and is a constant). The normal stress distribution along the soil/wall interface agrees well with the existing classic Rankine theory for the passive smooth retaining wall problem. As shown in Figure 5.13, the normal and shear stresses distributions along the failure surface indicate $\theta_2 = 44.98^\circ$ and $\psi_{s2} = 0.1^\circ$. The predicted failure mechanism is similar to that by classic Coulomb theory ($\theta_2 = 45^\circ$) and DLO solution. An illustration of the variation of the results for fixed θ_1 and ψ_{s1} with θ_2 and ψ_{s2} allowed to vary, are shown graphically in Figure 5.15 for the backfill and shows there is one minimum solution. If the values of θ_2 and ψ_{s2} get bigger (compared with the minimum solution), no feasible solutions can be found by the proposed method.

For the multi-wedge analysis of the passive wall problem, the choice of parameters to represent a cohesive backfill is a key problem for the engineer who wants to use the proposed method. On the basis of the sensitivity analysis above and the demonstrations of the yield surfaces determined by different parameter sets, it can be concluded that the non-linear coefficient $m_2 = 1.001$ gives a good balance for saving computation time while not affecting the accuracy of the solutions. When $c_{02}/\sigma_{t2} = 1/500$ the yield surface used in non-linear analysis is very close to the related linear yield surface. In practical engineering, $m_2 = 1.001$, $a_2 = 1$, $c_{02}/\sigma_{t2} = 1/500$ can be taken as an effective parameters group to represent cohesive backfills

on the basis of the analysis in this thesis. However the numerical results are more accurate when the value of c_{02}/σ_{t2} is smaller.

This analysis could also be applied in the similar metal cutting problem and has been published in "Use of non-linear failure criteria to extract stress data from upper bound plasticity solutions." (Conference: UKACM London, 2019).

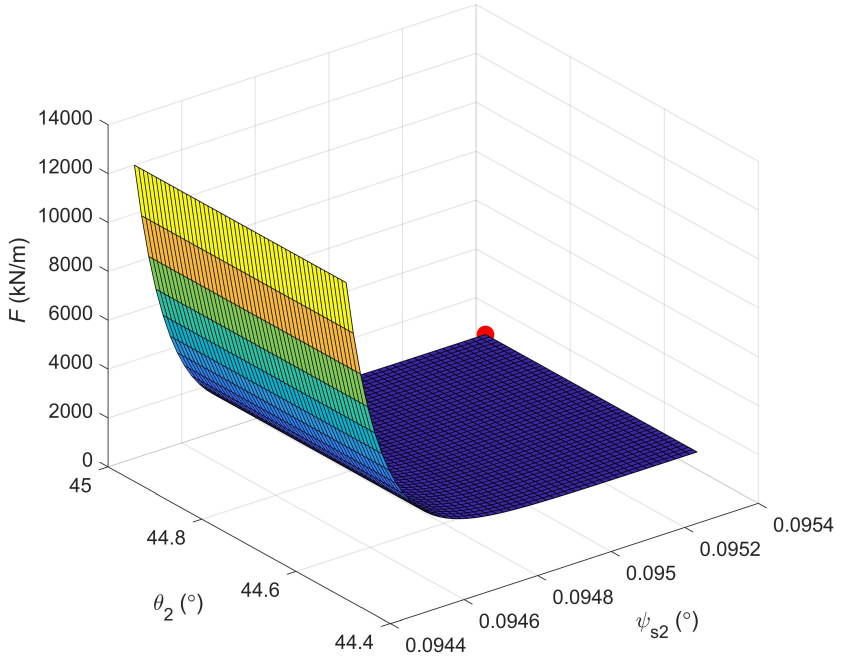

Figure 5.15: Variation of limit load F with fixed values of $\theta_1 = 90°$ and $\psi_{s1} = 0.1°$ for the case: $\gamma_2 = 20$ kN/m^3 and $H = 5$ m. The red dot represents the optimal solution depicted in Figure 5.13.

.

5.5 Conclusions

1. An example addressing the anchor uplift problem demonstrated the solution process for multi-wedges and showed that the solution behaviour follows a similar pattern to that for linear soils. More accurate solutions for this problem were obtained compared to previous work in the literature.

2. Using the proposed multi-tangent non-linear DLO method, the predicted limit loads for anchor problem are almost consistent with those by the variational multi-wedge analysis. The differences between 3-line DLO solutions and 4-line DLO solutions are very small for the anchor problems.

3. Analysis of a smooth retaining wall against a cohesive backfill using two non-linear slip-lines demonstrated that the upper bound solutions can generate good predictions of shear and normal stresses along multiple slip-lines.

4. Discussion of the choice of parameters to give good representations of linear materials was made and the solutions by the determined parameters sets are almost consistent with the DLO solutions and theoretical solutions.

Chapter 6

Non-associative permutation analysis of toppling block problems

6.1 Introduction

The toppling-sliding failure mechanism is a common mode of instability in rock slopes, which may be modelled by a range of different methods. In this chapter, the determination of the load factor triggering toppling-sliding failures is explored in detail by linear programming within the framework of limit analysis theory. A conventional limit analysis approach employing the associative flow rule typically overestimates stability because of the assumption of excessive dilatancy at the joints (Babiker 2013). To overcome this problem, this study examines in detail the non-associative (abbreviated as NA) analysis of a classic toppling block problem considering a low dilation model. A permutation method is used to benchmark the problem solution space by establishing every possible non-associative solution for a series of rock toppling problems. Within this method, all possible permutations of relative joint movements are solved by the developed LP formulation.

6.2 Problem specification

Toppling movement occurs in slopes where a repeated spaced set of joints or bedding planes strike parallel, or nearly parallel, to the slope face and dip at a steep angle into the face. According to Babiker (2013), for toppling-sliding failure, the toppling rock blocks force the rock near the toe of the slope to fail by sliding through intact material, shown in Figure 6.1 (a). Toppling involves the block rotating around a pivot point which is often taken to be at the lowest corner point of the rigid block, shown in Figure 6.1 (b). On the other hand, shown in Figure 6.1 (c), sliding occurs when the tangential component of the weight (W sinα) is greater than the shear resistance at the base (μW cosα), where W is the weight of the block, α is the slope tilt angle and $\mu =$ tanϕ is the friction coefficient. For multiple blocks interacting forces complicate the analysis.

For a stability assessment, a triggering failure load factorλ is introduced to initiate collapse. In this study, failure is identified by the tilt angle (α) at which collapse occurs. In some physical experiments a tilting table is used to initiate collapse: as the tilt angle of the base is increased, the horizontal components of the weight driving sliding or rotation increase. This is analogous to applying a horizontal force equal in magnitude to the self weight of each rigid block multiplied by the triggering failure load factorλ , as shown in Figure 6.2. The tilt angle can then be obtained from the following relation:

$$\tan\alpha = \frac{\lambda W}{W} \tag{6.1}$$

And hence:

$$\alpha = \tan^{-1}\lambda \tag{6.2}$$

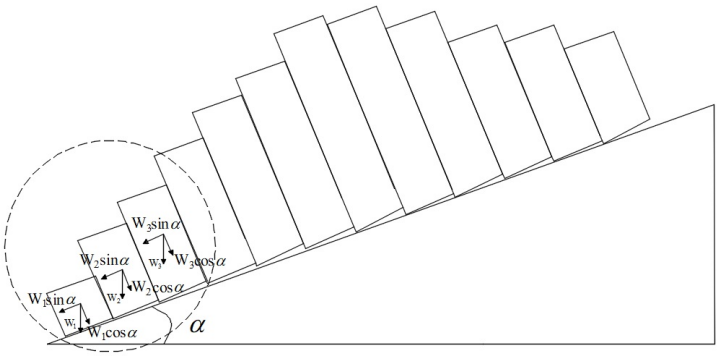

(a)

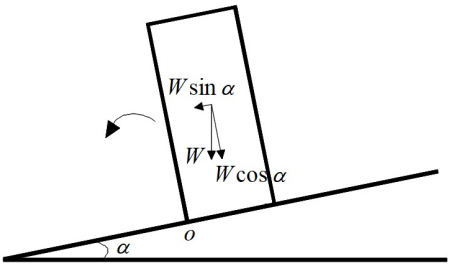

(b)

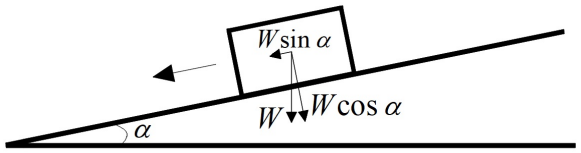

(c)

Figure 6.1: Slope failure: (a) toppling-sliding failure; (b) toppling for single block; (c) sliding for single block.

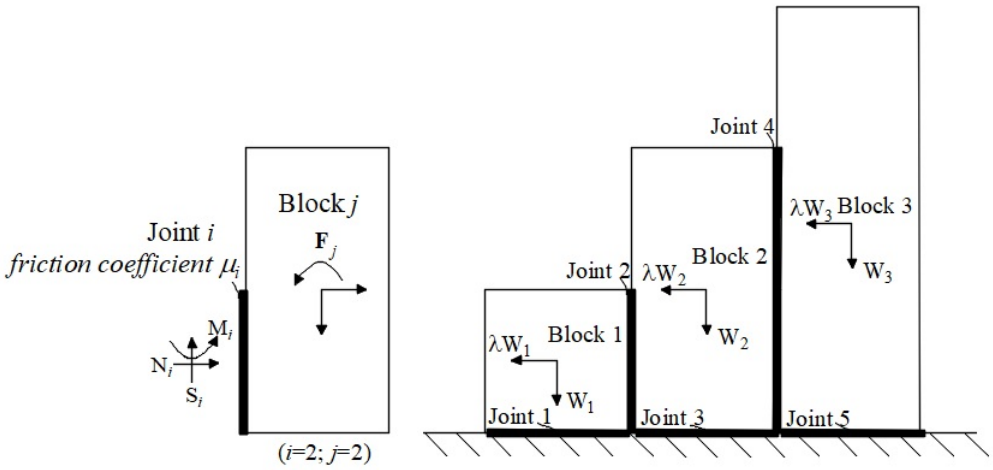

Figure 6.2: Analogous illustration for toppling-sliding slope failure: block j and contact forces for joint i.

Since the specific pattern of rock discontinuities often influences the failure mechanism and triggering failure load factorλ, there is some justification for modelling the rock mass with regularly spaced fractures as assemblages of discrete rigid blocks. Some assumptions should be made for simplicity of calculation: (1) No tension may be transmitted across the joints between different rigid and infinitely strong blocks; (2) Distinct blocks may slide and/or topple relative to each other; (3) Contact is assumed at joint interfaces.

This problem can be solved using linear optimization programming. The basic formulation for modelling rigid block problems has been introduced in Chapter 3. Assuming each block has three degrees of freedom around its centroid: horizontal displacement, vertical displacement and rotation, the three forces act along the joints between blocks can be expressed as: shear force, normal force and moment, as shown in Figure 6.2. The rigid block formulation (Gilbert & Melbourne 1994) is based on the associative flow rule and yield conditions govern the yield surface along each joint between blocks for both slip and rotation, shown in Figure 6.3. However, the effect of non-associativity on frictional joints cannot be ignored. To demonstrate the difference between associative and non-associative results, a simple

multi-block problem will be considered analytically.

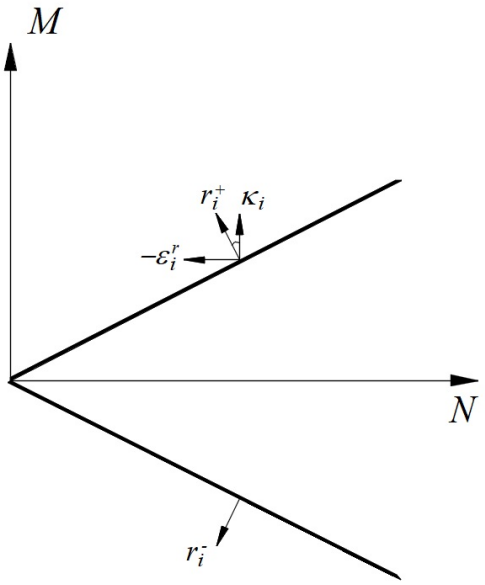

(a) Toppling

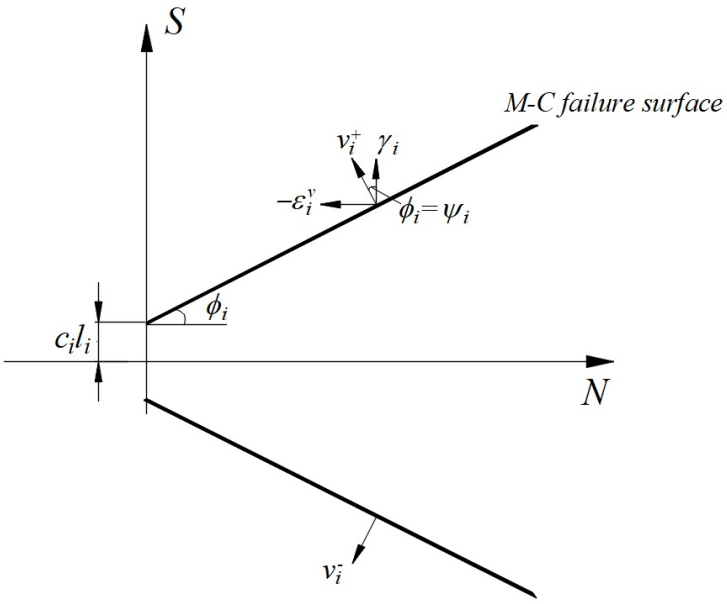

(b) Sliding

Figure 6.3: Yield domains (obeying associative rule): (a) toppling and (b) sliding.

6.3 Non-associative analysis of a specific collapse mode

6.3.1 Analysis for simple systems

In general, a rock slope is composed of a number of blocks that may slide and/or topple, and which will invariably interact with each other in a statically indeterminate way. In order to solve the statically indeterminate problem, the effects of non-associativity and the kinematics of the problem should be considered (Babiker 2013). This can be illustrated by the two-block system shown in Figure 6.4, toppling failure can occur when the larger of the two blocks rotates while the smaller block slides. In this system it will be shown that the movement of the second joint (which connects two rigid blocks) governs the range and value of collapse load factor λ. For the associative case, shown in Figure 6.4 (a), the joint connecting two rigid blocks both rotates and slides. However, for the non-associative zero dilation case shown in Figure 6.4 (b), the joint mentioned above will only rotate about the pivot point for small displacements. A worked example illustrating the effects of non-associativity is given below.

Figure 6.5 shows the free body diagram for the two-block system. To simplify the model, a cohesionless material interface is considered. It is assumed that both of the two blocks have the same width (one unit), and the height of the taller block (two units) is twice that of the shorter block (one unit). The unit weight of the block is assumed one unit. For two-block problem, the yield condition should be considered first.

As shown in Figure 6.5, sliding at the base of Block 1 requires full mobilization of

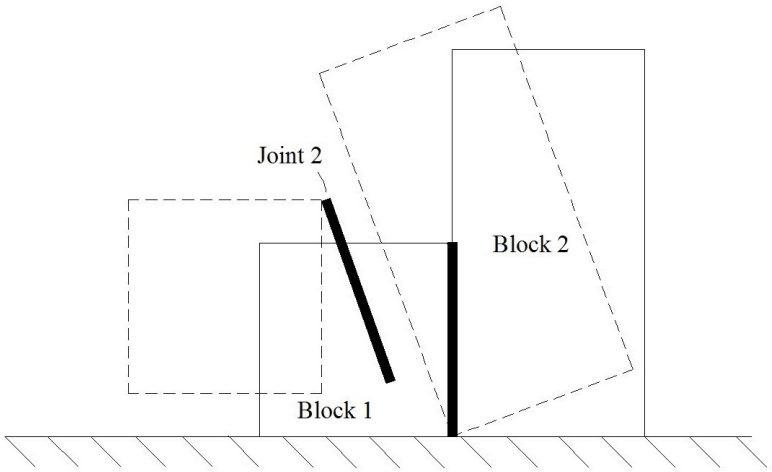

(a) Associative mechanism

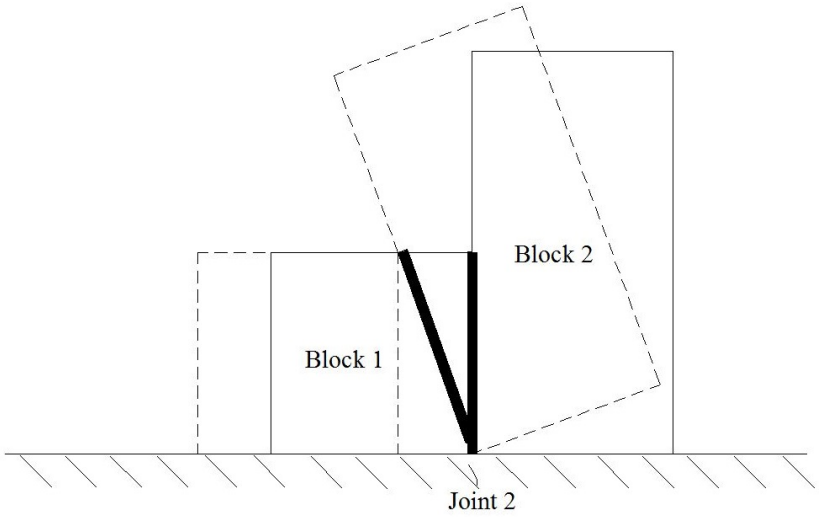

(b) Non-associative mechanism

Figure 6.4: Two-block analysis.

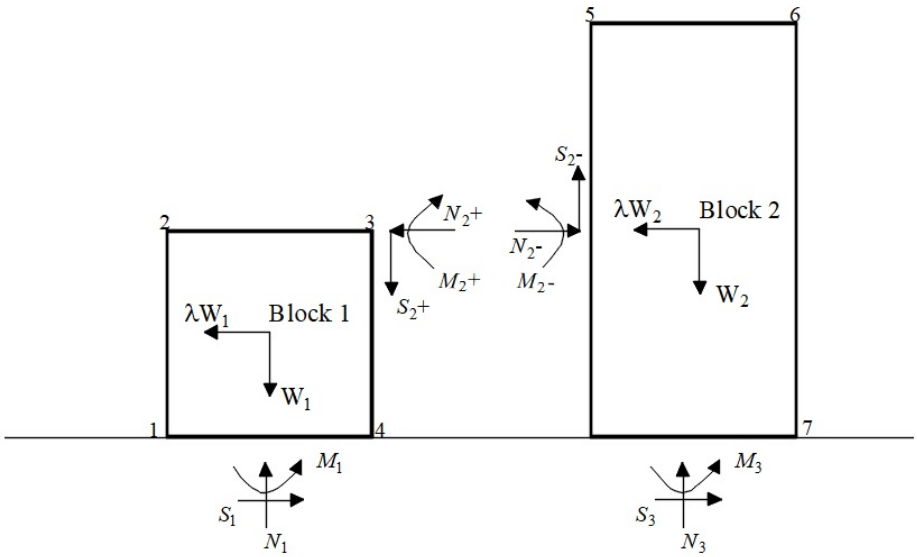

Figure 6.5: Two-block failure: free body diagrams.

friction:

$$S_1 = N_1 \tan \phi \tag{6.3}$$

For rotation of Block 2 (shown in Figure 6.5) about its lower left corner, the following condition must hold:

$$0 < S_3 < N_3 \tan \phi \tag{6.4}$$

The joint between two blocks will mobilize a strength m_{bs}, such that:

$$S_2 = m_{bs} \cdot N_2 \tan \phi \tag{6.5}$$

where $-1 \leq m_{bs} \leq 1$.

Based on the equilibrium, according to Babiker (2013), the mobilized strength m_{bs} can be determined for various values of λ, and the yield conditions above should be satisfied when the solution is found. It is interesting to find that the minimum non-

associative solution ($\lambda = 0.5559$) is for $m_{bs} = -1$ and the maximum ($\lambda = 0.6165$) is for $m_{bs} = 1$. Therefore, it is important to consider non-associative flow.

6.3.2 Limit analysis formulation based on permutation analysis

When toppling-sliding failure occurs within a rock slope, the relative movement on joints between rigid blocks will have specific types: 1) rotation only; 2) rotation and sliding; 3) sliding only; 4) no relative movement. In general, the movement could act in either direction. If the direction of movement for each joint (or 'permutation' of movements) is known in advance, then a modified equilibrium form of the associative case can be written with the known movement 'forced' in the equation.

Considering an assemblage of b blocks and c joints, the equilibrium form can be expressed as follows:

$$\min \lambda \tag{6.6}$$

subject to:

$$\mathbf{Bq} - \lambda \mathbf{f}_{\mathrm{L}} = \mathbf{f}_{\mathrm{D}} \tag{6.7}$$

$$\mathbf{N}_{unc}^{T} \mathbf{q}_{unc} \leq \mathbf{C}_{unc} \tag{6.8}$$

$$\mathbf{N}_{for}^{T} \mathbf{q}_{for} = \mathbf{C}_{for} \tag{6.9}$$

where $\mathbf{N}$ is a modified suitable ($4c \times 3c$) constraint matrix ($\mathbf{N}_{unc}$ is unconstrained part; $\mathbf{N}_{for}$ is forced part) , $\mathbf{C}$ is a suitable ($4c \times 1$) intercept matrix ($\mathbf{C}_{unc}$ is unconstrained part; $\mathbf{C}_{for}$ is forced part), and $\mathbf{q}$ ($\mathbf{q}_{unc}$ is unconstrained part; $\mathbf{q}_{for}$ is forced part) and $\mathbf{f}$ are respectively vectors of joint forces and block loads. The objective is thus to minimize λ whilst ensuring that the yield condition is not violated

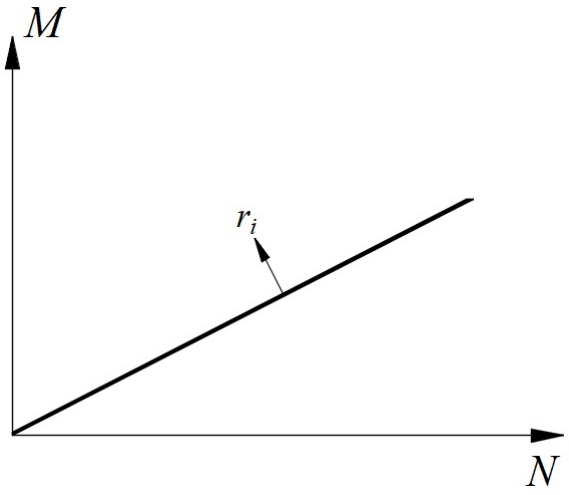

(a) Toppling

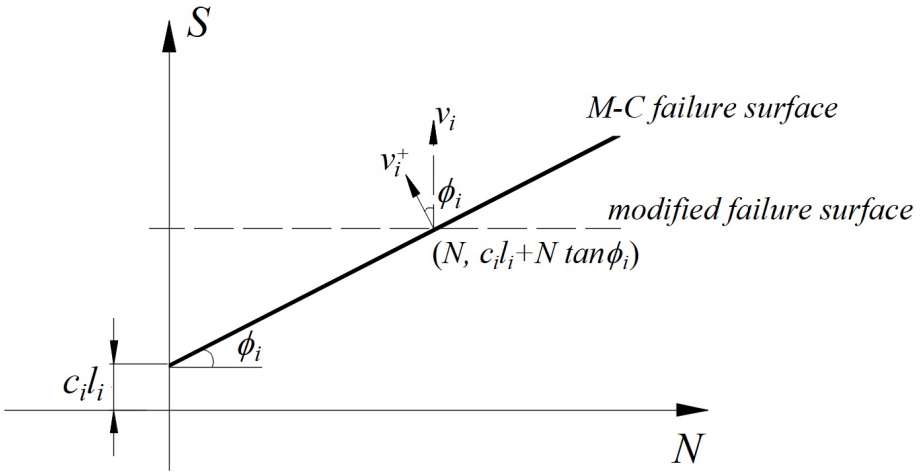

(b) Sliding

Figure 6.6: Yield domains (obeying modified non-associative rule): (a) toppling and (b) sliding.

along any unconstrained joint but is satisfied along any forced joint between blocks $i = 1, ...c..$ Yield conditions in the *N-S-M* domain govern the failure criterion along each joint i between blocks by both sliding and toppling, as shown in Figure 6.6. For completeness the derivation for its 'true' dual kinematic form is illustrated in **Appendix C** and **Appendix D**. For the non-associative toppling block problem in this thesis, the dilation angle ψ will be taken as zero (pure-friction case), whose kinematics are similar to those for cohesive material. The lowest non-associative load for the defined pattern is thus found. Replacing $\min \lambda$ with $\max \lambda$ will find the maximum non-associative load thus bracketing the NA load for this configuration. This method is called the 'max-min method' in this thesis. To complete the analysis, it remains to demonstrate that there exists a compatible NA set of kinematics consistent with these relative movements.

According to the associative flow rule, which is based on the normality rule ($\phi = \psi$), the plastic potential is the same as the yield function. But for non-associative flow, the plastic potential and yield function are separate, they intersect (Lade 2002). As shown in Figure 6.6 (b), the non-associative solution is graphically represented by the intersection of the two lines representing the yield and plastic flow functions respectively. Developed from the associative kinematic formulation, a 'forced' kinematic formulation can be expressed as follows:

$$\min \ -\mathbf{f}_{\mathrm{D}}^{T}\mathbf{d} + \hat{\mathbf{C}}^{T}\mathbf{p^0} \tag{6.10}$$

subject to:

$$\mathbf{Dp^0} - \mathrm{B}^{\mathbf{T}}\mathbf{d} = \mathbf{0} \tag{6.11}$$

$$\mathbf{f}_{\mathrm{L}}^{T}\mathbf{d} = -1 \tag{6.12}$$

The $\mathbf{p^0}$ variables are constrained so that on each joint the movement matches that specified in the equilibrium permutation, i.e. if the permutation required sliding

for one joint, then for the joint one of the $\mathbf{p^0}$ values is zero and the other is ≥ 0, depending on the sign convention. This needs to be enforced for the constraints on all $\mathbf{p^0}$ variables. If there is no yielding on a joint then both $\mathbf{p^0}$ variables are equal to zero.

Since the sign of the $\mathbf{p^0}$ variable is always known due to the permutation, then it should be possible to simplify the $\mathbf{Dp^0}$ and $\hat{\mathbf{C}}^T\mathbf{p^0}$ terms and only use one $\mathbf{p^0}$ variable per joint rather than two.

In this analysis each term in $\hat{\mathbf{C}}$ needs to be equal to $cl + Ntan\phi$, where the normal force N is obtained from the equilibrium analysis. The $\mathbf{D}$ matrix needs to be changed to assume zero dilation i.e. assume $\psi_i = 0$ for this matrix. Furthermore, for the same contact interface, the displacement rates contained in $\mathbf{u}_i$ are related to the respective non-negative resultant displacement rates in $\mathbf{p}_i^0$ as follows:

$$\mathbf{u}_i = \mathbf{D}_i\mathbf{p}_i^0, \mathbf{p}_i^0 \geq 0 \tag{6.13}$$

or in explicit form:

$$\begin{bmatrix} \varepsilon_i \\ \gamma_i \\ \kappa_i \end{bmatrix} = \begin{bmatrix} -l_i/2 & -\tan\psi_i \\ 0 & 1 \\ 1 & 0 \end{bmatrix} \begin{bmatrix} r_i \\ v_i \end{bmatrix}, \begin{bmatrix} r_i \\ v_i \end{bmatrix} \geq \begin{bmatrix} 0 \\ 0 \end{bmatrix} \tag{6.14}$$

where now $\mathbf{p^0}$ is a $(2c)$ vector of the resultant displacement rates. In this thesis, the dilation angle ψ_i is assumed as zero, shown in Figure 6.6 (b).

For different cases of movement of the joint i, Eq. 6.14 has different forms:

(1) If the joint i only rotates, Eq. 6.14 should be converted to:

$$\begin{bmatrix} \varepsilon_i \\ \gamma_i \\ \kappa_i \end{bmatrix} = \begin{bmatrix} -l_i/2 & -\tan\psi_i \\ 0 & 1 \\ 1 & 0 \end{bmatrix} \begin{bmatrix} r_i \\ v_i \end{bmatrix}, r_i \geq 0 \text{ and } v_i = 0; \tag{6.15}$$

(2) If the joint i both rotates and slides, Eq. 6.14 should be converted to:

$$\begin{bmatrix} \varepsilon_i \\ \gamma_i \\ \kappa_i \end{bmatrix} = \begin{bmatrix} -l_i/2 & -\tan\psi_i \\ 0 & 1 \\ 1 & 0 \end{bmatrix} \begin{bmatrix} r_i \\ v_i \end{bmatrix}, \begin{bmatrix} r_i \\ v_i \end{bmatrix} \geq \begin{bmatrix} 0 \\ 0 \end{bmatrix} \tag{6.16}$$

(3) If the joint i only slides, Eq. 6.14 should be converted to:

$$\begin{bmatrix} \varepsilon_i \\ \gamma_i \\ \kappa_i \end{bmatrix} = \begin{bmatrix} -l_i/2 & -\tan\psi_i \\ 0 & 1 \\ 1 & 0 \end{bmatrix} \begin{bmatrix} r_i \\ v_i \end{bmatrix}, r_i = 0 \text{ and } v_i \geq 0. \tag{6.17}$$

This form can be used to describe the kinematics caused by zero dilation and the solution from the formulation also satisfies the predefined yielding condition ('forced' condition) for each joint since the normal force used in intercept matrix is obtained by the proposed non-associative equilibrium formulation. This means the solution can be graphically taken as the intersection of plastic flow and yield surface (shown in Figure 6.6(b)), which follows the assumption of non-associative flow rule proposed in this thesis. In other words, this formulation is developed to make sure that the plastic potential will cross the yield surface at the stress point that guarantees kinematic admissibility.

By introducing the permutation analysis there will be up to 4^n(for n joints) failure mechanisms theoretically. Among these cases, only one case will occur obeying the associative flow rule in limit analysis. Other feasible cases will be the so-called non-associative failure mechanisms. Obviously non-associative results are not unique and there will be a range of solutions all lower than the associative solutions. The proposed permutation method combined with 'max-min method' allows evaluation of all solutions, which is illustrated in detail below.

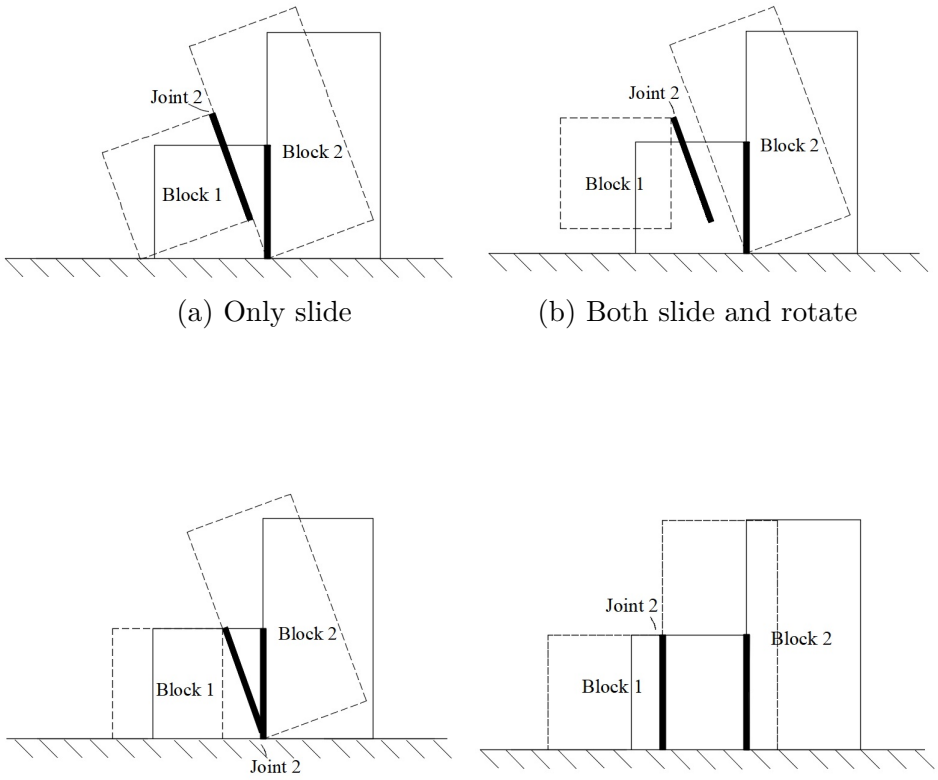

(a) Only slide (b) Both slide and rotate

(c) Only rotate (d) No relative movement

Figure 6.7: Possibilities of the movement of the vertical joint in two-block system.

6.4 Permutation analysis of simple multi-block problem

In order to obtain all possible non-associative solutions for the toppling block problem, a procedure may be conducted considering all possible permutations of relative joint movements. An example is presented for the simple two-block problem in Figure 6.7. As shown there are only 4 credible possible modes. Due to the combined physical effects, base horizontal joints will slide (down slope) and/or rotate (anti-clockwise) in one direction when the tilt table rotates anti-clockwise. If the movements of the adjacent horizontal joints are set, it should be possible to work out what the vertical joint must do according to the relative positions of two blocks. Especially, when both of the adjacent horizontal joints slide at the same velocity, there will be no relative movements for the vertical joints connecting two adjacent

Serial	Joint 1	Joint 2	Joint 3	λ_{max}	λ_{min}	Failure mechanism
1	R	S	R	0	0	Invalid
2	R	C	R	0	0	Invalid
3	S	S	R	0.6165	0.5000	Invalid
4	S	C	R	0.6165	0.6165	Valid
5	S	R	R	0.6165	0.5559	Valid
6	S	N	S	0	0	Invalid

Table 6.1: Permutation procedure result : for joint i (i=1,2,3), 'R' means the joint will only rotate down the slope, 'C' means the joint will both rotate and slide down the slope, 'S' means the joint will only slide down the slope, 'N' means the joint will have no relative movement. If $\lambda = 0$, the hypothetical case is infeasible.

blocks. This reduces the number of permutations to be considered.

Although the movement of central joint can be determined by the movements of the other joints, a permutation analysis could generate all possible combination cases to find the feasible non-associative solutions.

6.4.1 Analysis of two-block problem

Assuming $\phi = 36°$, all possible combinations of joint movements can be listed to find the feasible range of the non-associative results, as shown in **Appendix E**. According to Figure 6.5 and the movement analysis shown in Figure 6.7, the movement of Joint 2 is determined by those of other joints, the possible failure mechanisms are shown in Table 6.1.

From Table 6.1 it can be concluded that one feasible minimum non-associative solution (obtained by the proposed permutation procedure) is 0.6165, which equals the associative load factor. Using the 'true' dual kinematic formulation (shown in **Appendix D**), the kinematic mechanism is as the same as the associative mechanism, as shown in Figure 6.8 (a). The other feasible minimum non-associative solution (obtained by the proposed permutation procedure) is 0.5559, whose kinematic mechanism (obtained by Eq. 6.14) is shown in Figure 6.8 (b). It can be concluded from Figure 6.8 (b) that the non-associative kinematic mechanism is

caused by zero dilation. The influence of the angle of friction on the associative load and the minimum non-associative load by this permutation approach is shown in Figure 6.9 for the two-block system.

The comparison with Babiker's NAIM (short for Non-associative Iterative Method) outcomes is also shown in Figure 6.9, which shows a good agreement. According to the proposed permutation procedure, if the objective function is changed to seek for the maximum λ, the maximum non-associative solution for load factor will be obtained as λ_{max} shown in Table 6.1.

However for $\phi \leq 26.5°$, the vertical joint connecting two blocks will have no relative movement (two horizontal joints will only slide; Joint2 will have no relative movements) when $\phi = \alpha$. The kinematic mechanism is shown in Figure 6.10 (when $\phi = \alpha = 26°$). This can be explained by the toppling yield condition for a single block toppling (Ashby 1971): if the width of the block b is bigger than $h{\cdot}\tan\alpha$ (h is the height of the block), the toppling won't happen. For this case, the critical angle for single block toppling is arctan(0.5), which is around 26.5°. It can be concluded that if the frictional angle of the contact interfaces is small, the two-block system can be taken as two separate single sliding blocks when the tilt angle α is increased to the frictional angle ϕ.

Thus, the feasible range of non-associative solutions for two-block problem can be predicted by permutation method with a reduced, more realistic, level of dilation within a limit analysis framework.

6.4.2 Extension to multiple-block problems

By applying the proposed permutation method and 'max-min method', the maximum and minimum load factor λ can be obtained to bracket the range of possible non-associative solutions. The multi-block problem shows the ability of the permutation analysis to pick out distinctive mechanisms, as shown for 3 blocks in

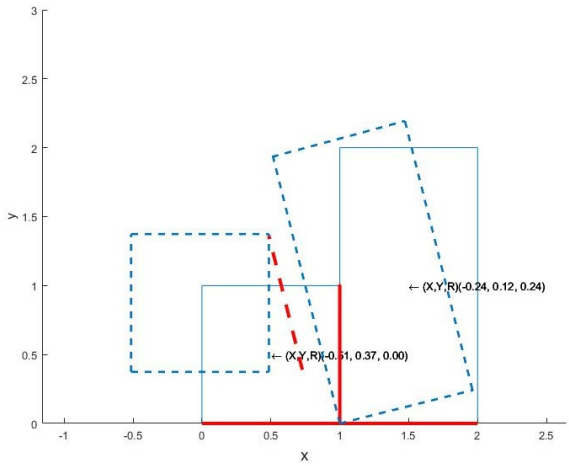

(a) Associative load factor ($\lambda = 0.6165$)

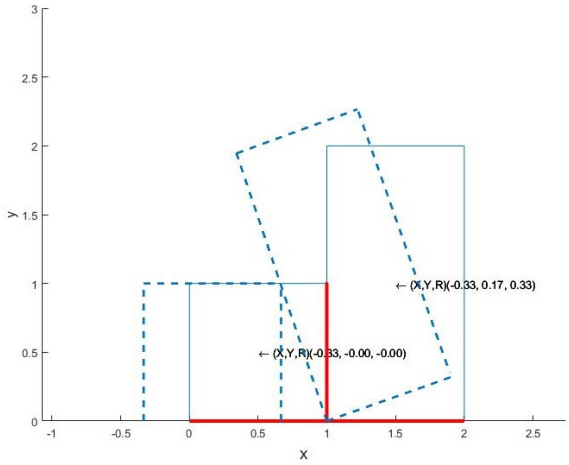

(b) Non-associative load factor ($\lambda = 0.5559$ - 0.6165)

Figure 6.8: Kinematic mechanism for two-block problem. (X: Displacement rate of the block centroid in X-direction; Y: Displacement rate of the block centroid in Y-direction; R: Rotation rate of the block centroid.)

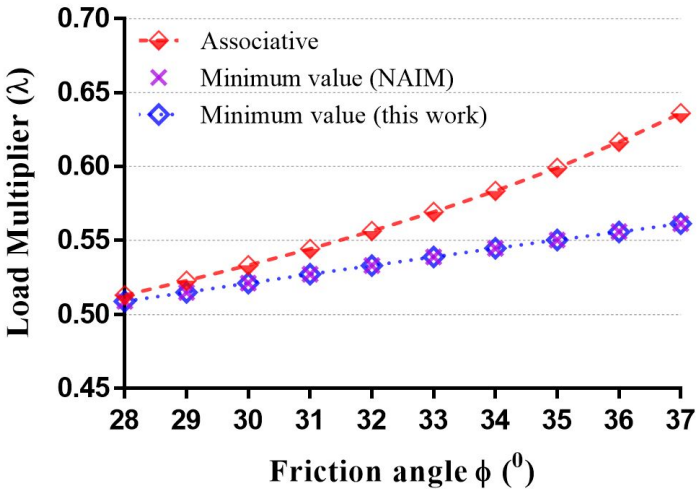

Figure 6.9: The comparisons in load multiplier λ with varying friction angle ϕ.

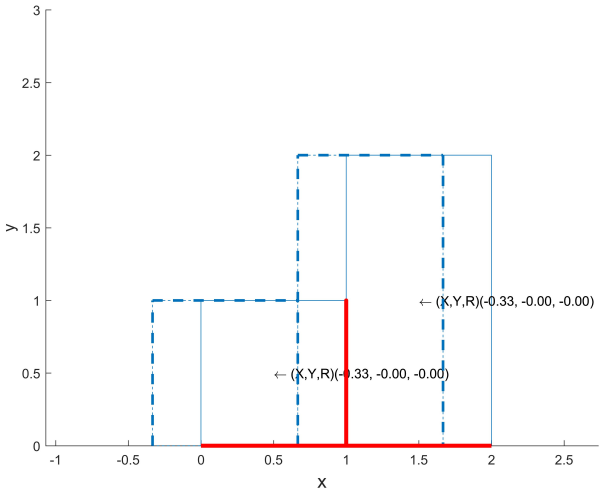

Collapse load factor $\lambda = 0.4877$

Figure 6.10: Non-associative collapse mechanism for two-block problem with $\alpha = \phi = 26°$.(X: Displacement rate of the block centroid in X-direction; Y: Displacement rate of the block centroid in Y-direction; R: Rotation rate of the block centroid.)

Figure 6.11 and for 4 blocks in Figure 6.12. The collapse mechanisms determined both by associative solution (dilation angle equals the friction angle) and minimum non-associative solution (caused by zero dilation) are predicted. Essentially, the permutation analysis involves 4^n (for n joints) sets of a single non-associative analysis with a different predefined failure mechanism. Based on the author's MATLAB code, each non-associative analysis takes around 0.5 seconds (0.4-0.6 seconds). Therefore, for two-block problem the computation time will be around 32 seconds. However, for six-block problem, the computation time will be around 2097152 seconds (nearly 24.3 days). Considering the computation time, this thesis only discusses the results for two- to five- block problems. As shown in Figure 6.13, the feasible range for the non-associative solution can be predicted by 'max-min method' based on the permutation method. And the maximum non-associative solution equals the associative solution.

For the 5-block system (the free body diagram for the five-block system considered in Figure 6.14), the kinematic failure mechanism for associative case with $\lambda = 0.5008$ is shown in Figure 6.15(a). The non-associative failure mechanism caused by zero dilation (obtained by Eq. 6.14 and $\lambda = 0.3274$) is similar to those for 2,3,4 block systems: the first block will slide, and other blocks will rotate, shown in Figure 6.15(b). By the proposed permutation equilibrium formulation, a different minimum non-associative solution ($\lambda = 0.4459$) can be picked out. To explore the difference from associative case, the shear and normal forces acting on the base and sides of each block are examined and the results are shown in Figure 6.16. In Figure 6.16, the minimum non-associative solution is for the non-associative case with $\lambda = 0.4459$. It can be concluded that the difference exists in the forces acting on the last two blocks. For other blocks, the forces are approximately the same. The directions of the shear force exerted on Joint 7 and Joint 9 tend to be opposite for the associative and the non-associative case. It leads to the difference in failure mechanisms: joint 9 will both slide and rotate in the associative case

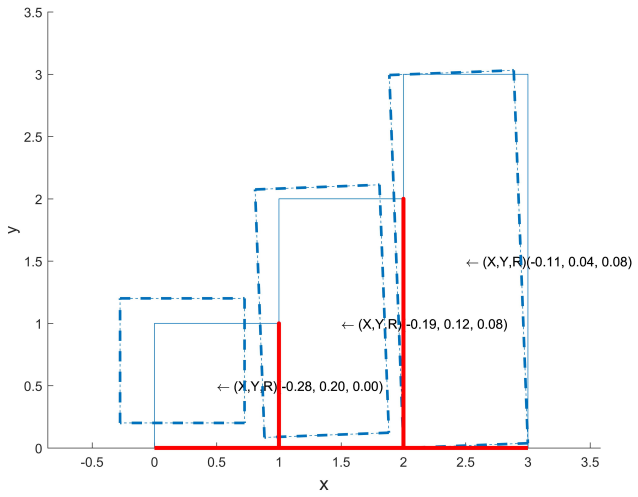

(a) Associative load factor ($\lambda = 0.5586$)

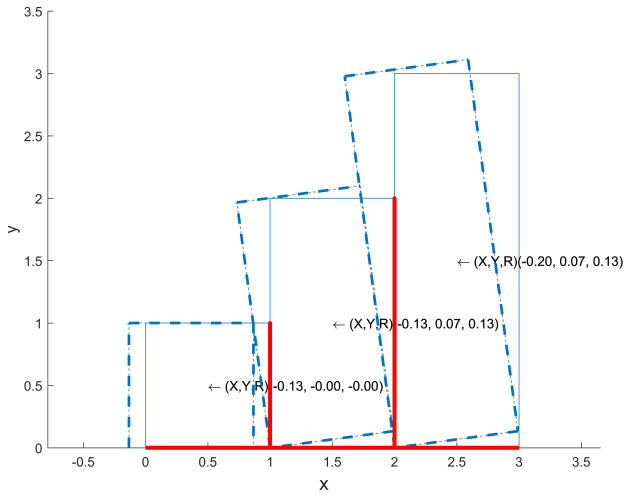

(b) NA load factor ($\lambda = 0.4564$ - 0.5586)

Figure 6.11: Collapse mechanism for three-block problem. (X: Displacement rate of the block centroid in X-direction; Y: Displacement rate of the block centroid in Y-direction; R: Rotation rate of the block centroid.)

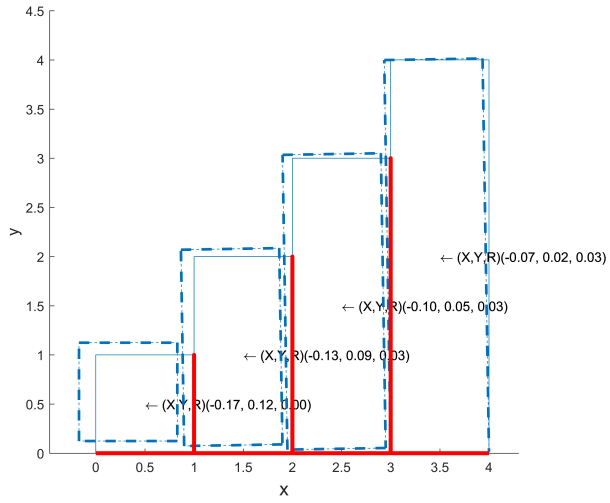

(a) Associative load factor ($\lambda = 0.5285$)

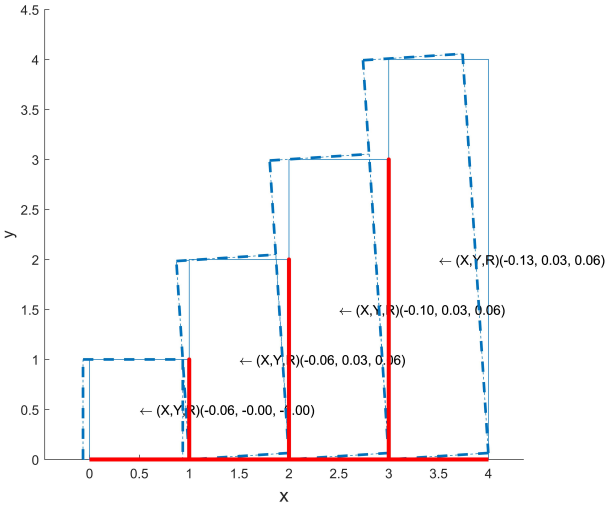

(b) NA load factor ($\lambda = 0.3844$ - 0.5285)

Figure 6.12: Collapse mechanism for four-block problem. (X: Displacement rate of the block centroid in X-direction; Y: Displacement rate of the block centroid in Y-direction; R: Rotation rate of the block centroid.)

(shown in Figure 6.17); however joint 9 will only rotate in the non-associative case. For the associative case, dilation occurs and there will be forces (for vertical joint 8) squeeze out two neighbouring blocks (Block 4 and Block 5), so the ground will generate reaction forces to the block. Therefore, the movement of joint 9 will slide uphill, which violates the initial assumption that all joints only slide downhill. For non-associative case ($\lambda = 0.4459$) with low dilation (non-zero dilation), there will be forces (for vertical joint 8) connecting two neighbouring blocks (Block 4 and Block 5), so the ground will generate reaction forces to the block. The difference between the associative and non-associative cases is the different directions of shear force of Joint 7 and Joint 9, this will lead to the different values of upward shear force acting between Block 4 and Block 5. For associative case, the shear force will be fully upwards, therefore the value of shear force of Joint 8 is bigger than that in non-associative case ($\lambda = 0.4459$).

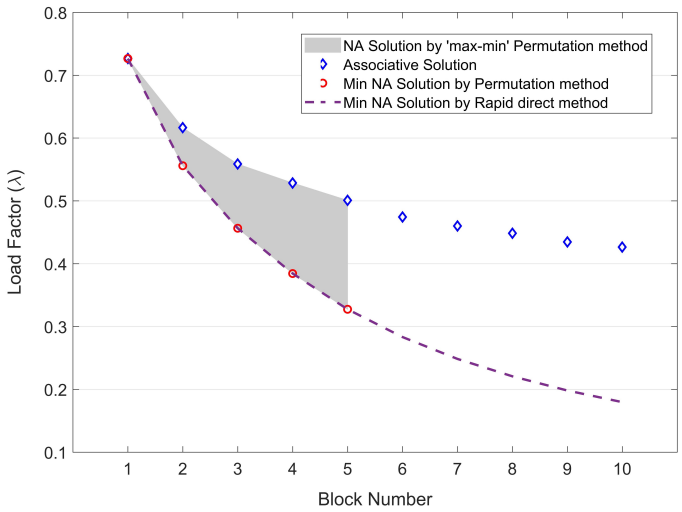

Figure 6.13: Comparison in load factor for multiple-block problems.

In summary, the results from the analysis of the simple systems demonstrate that the proposed non-associative procedure shows potential to predict different non-associative solutions established for a series of geometries involving a range of blocks. In order to predict the collapse mechanism for more complicated problems, the movements of joints in different directions should be considered in the assump-

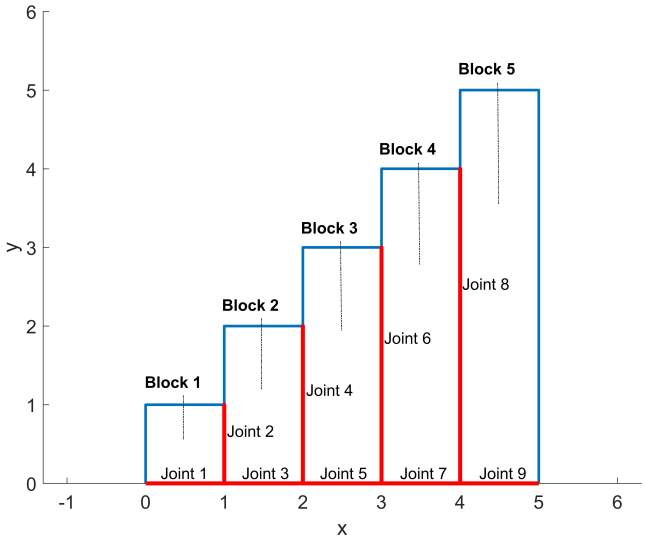

Figure 6.14: Five-block failure: free body diagrams.

tion. From the proposed kinematic non-associative formulation, it is convenient for readers to determine whether failure by a given mechanism is feasible. One limitation of the proposed permutation kinematic formulation in this thesis is that it can only predict the kinematic mechanism for the zero-dilation non-associative case.

6.5 Discussion of geometric variations

In reality, rock slopes will be composed of a number of irregular rock blocks in contact with each other. Therefore, it is meaningful to discuss the effects of geometric variations on the load factors. For convenience, this section only explores the effects of different ratios of the height difference to width of the blocks on the non-associative collapse loads and failure mechanisms. In this section, the ratio of the height difference (ΔH) to width (b) of each block is assumed the same and to be a constant, as shown in Figure 6.18.

Taking the two-block problem as an example, different values of $\Delta H/b$ lead to

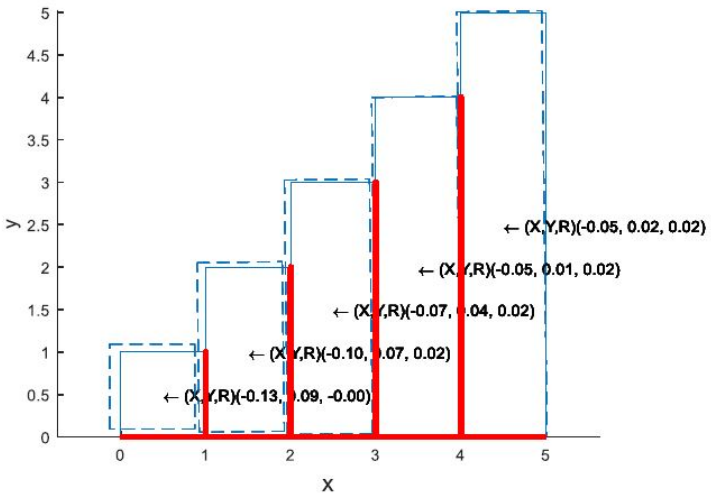

(a) Associative solution ($\lambda = 0.5008$)

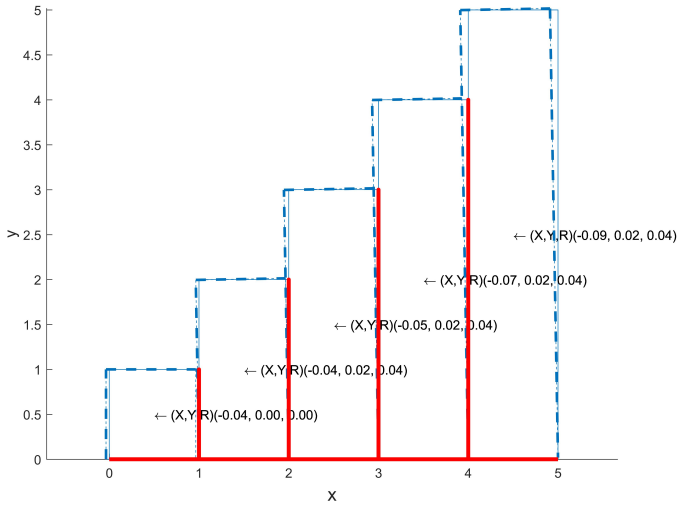

(b) Minimum non-associative solution ($\lambda = 0.3274$)

Figure 6.15: Five-block kinematic mechanism: (a) associative solution; (b) minimum non-associative solution (caused by zero dilation). (X: Displacement rate of the block centroid in X-direction; Y: Displacement rate of the block centroid in Y-direction; R: Rotation rate of the block centroid.)

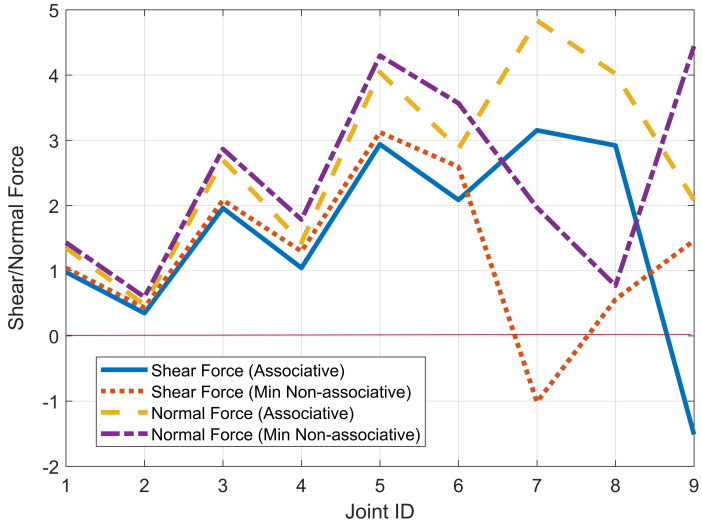

Figure 6.16: Comparison of normal and shear forces obtained from associative case and non-associative case.

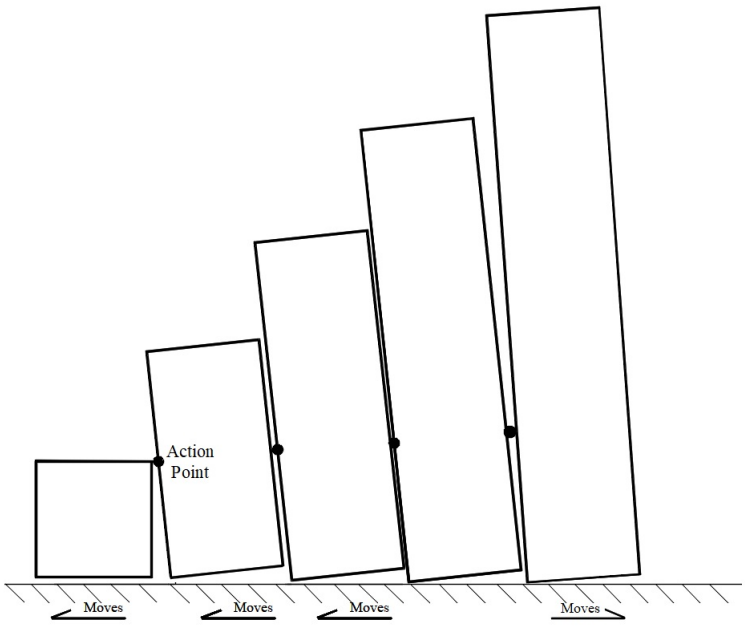

Figure 6.17: Associative kinematic mechanisms for five-block problem ($\lambda = 0.5008$).

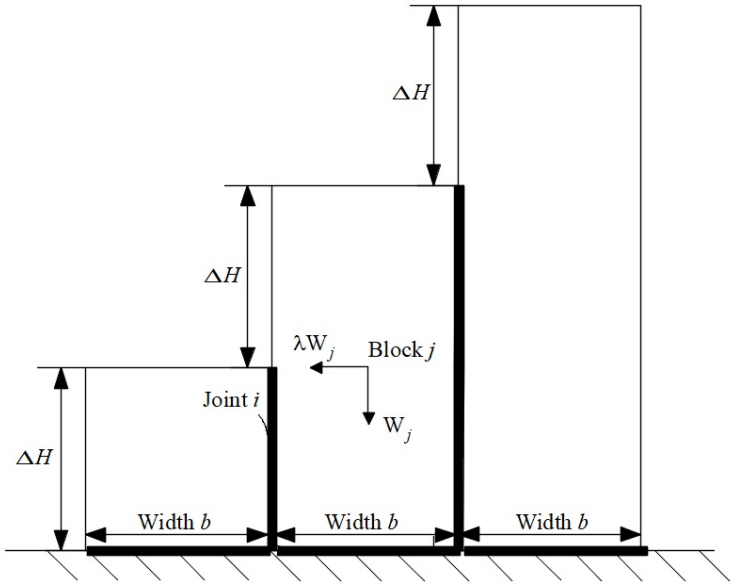

Figure 6.18: The definitions of the height difference and width of the blocks.

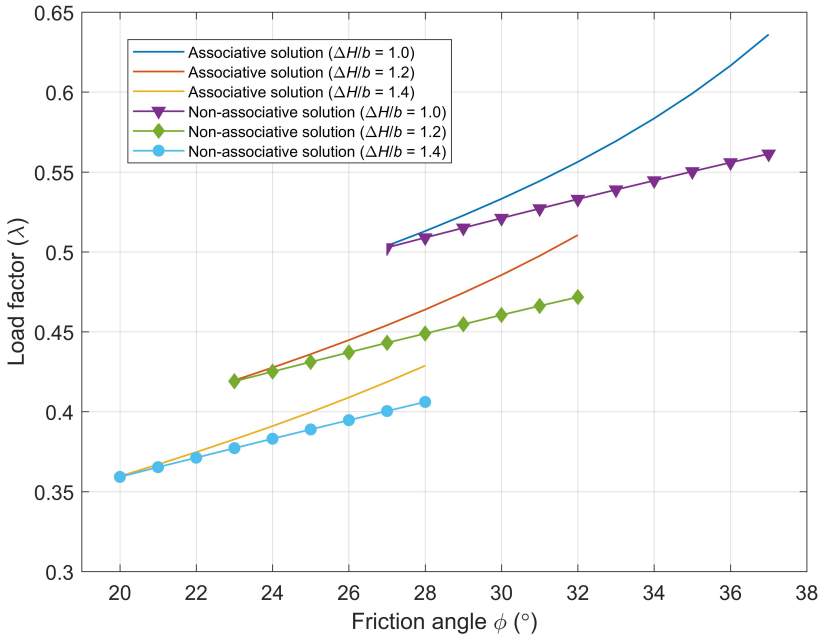

Figure 6.19: Comparison in collapse load factor with different values of $\Delta H/b$.

different non-associative load factors when the friction angle is fixed and dilation angle is zero. By comparison shown in Figure 6.19, it can be concluded that the collapse load factor is sensitive to small variations in initial geometry. And with the increase of the value of $\Delta H/b$, the associative and minimum non-associative (caused by zero dilation) load factors will decrease. For different values of $\Delta H/b$, the feasible ranges of the friction angle triggering toppling failure are different. The minimum value of the friction angle should satisfy the toppling yield condition and is bigger than $\arctan(b/h)$ (b is the width of the toppling block and h is the height of the toppling block). The maximum value of the friction angle should satisfy the boundary condition proposed in the analytical analysis for the block problem in Section 6.3.1: the mobilized strength should satisfy $-1 \leq m_{bs} \leq 1$. Furthermore, the effects of geometric variations on the collapse kinematic mechanisms should be discussed. When $\Delta H/b = 1.2$ and $\Delta H/b = 1.4$, by the proposed permutation method, the kinematic mechanisms are similar to those when $\Delta H/b = 1.0$. The kinematic mechanisms and load factors (when friction angle $\phi = 28°$) are shown in Figure 6.20, Figure 6.21 and Figure 6.22. However, when $\Delta H/b > 1.4$, no feasible non-associative load factor and related collapse kinematic mechanism could be found by the proposed permutation method with friction angle $\phi = 28°$. When the value of $\Delta H/b$ is bigger than 1.4, the effects of the friction angle on the associative load factor and minimum non-associative load factor (caused by zero dilation) are shown in Figure 6.23, Figure 6.24 and Figure 6.25.

6.6 Conclusions

1. Extended from the basic formulation used to tackle the associative toppling block problem previously, a new permutation method is proposed by arranging and combining possible movements of the joints connecting blocks. This approach gives full range of physically possible NA results compared with other numerical analysis and this generates solutions that successfully bracket

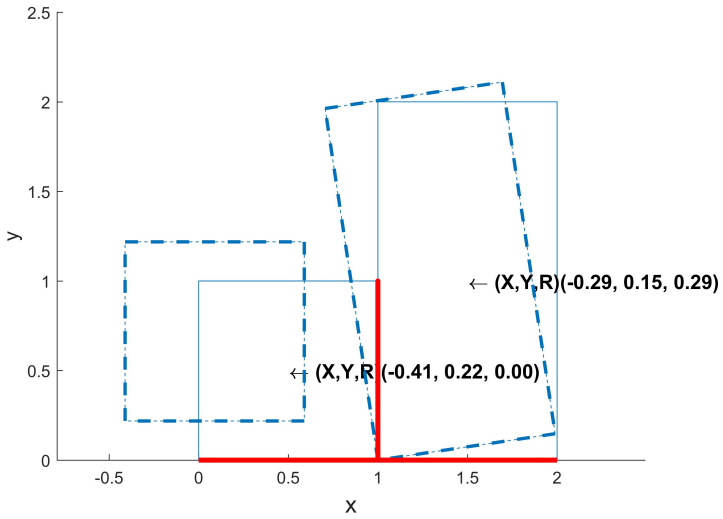

(a) Associative load factor ($\lambda = 0.5130$)

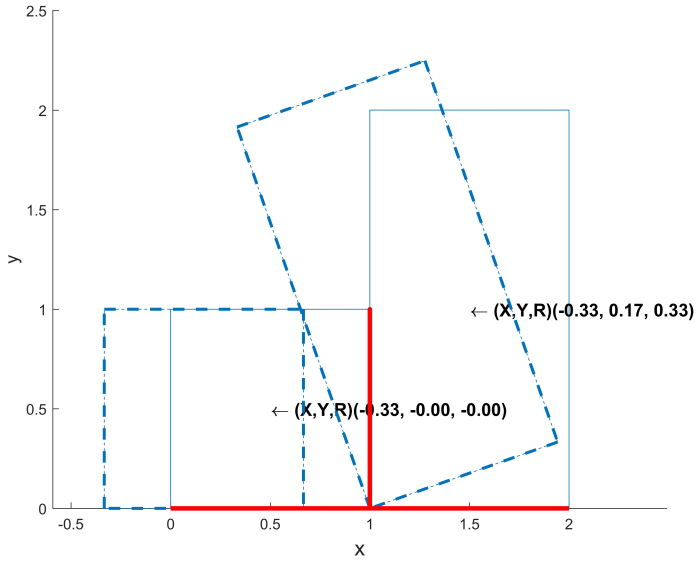

(b) NA load factor ($\lambda = 0.5089$ - 0.5130)

Figure 6.20: Collapse mechanism for two-block problem with $\Delta H/b = 1.0$. (X: Displacement rate of the block centroid in X-direction; Y: Displacement rate of the block centroid in Y-direction; R: Rotation rate of the block centroid.)

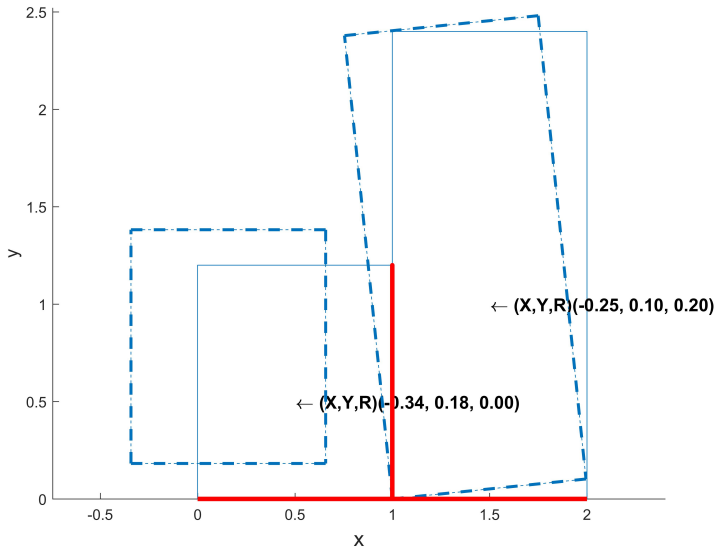

(a) Associative load factor ($\lambda = 0.4639$)

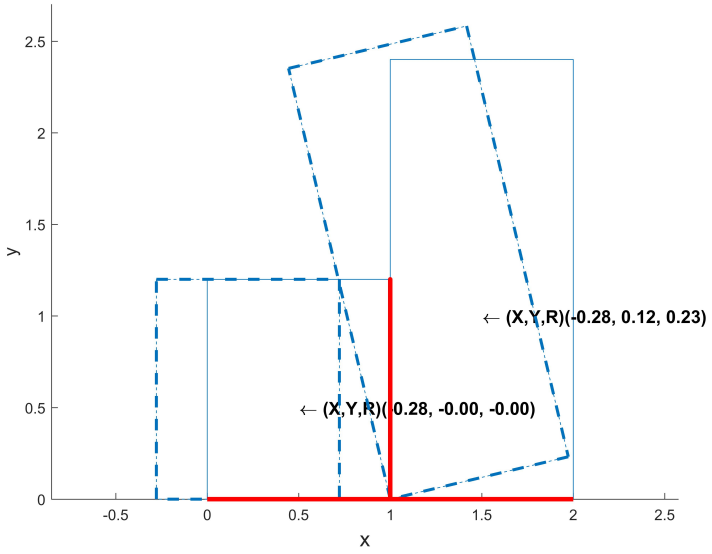

(b) NA load factor ($\lambda = 0.4489$ - 0.4639)

Figure 6.21: Collapse mechanism for two-block problem with $\Delta H/b = 1.2$. (X: Displacement rate of the block centroid in X-direction; Y: Displacement rate of the block centroid in Y-direction; R: Rotation rate of the block centroid.)

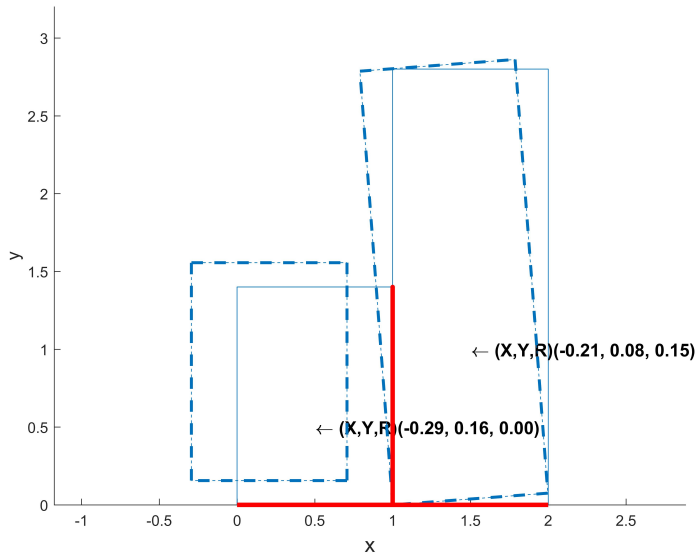

(a) Associative load factor ($\lambda = 0.4288$)

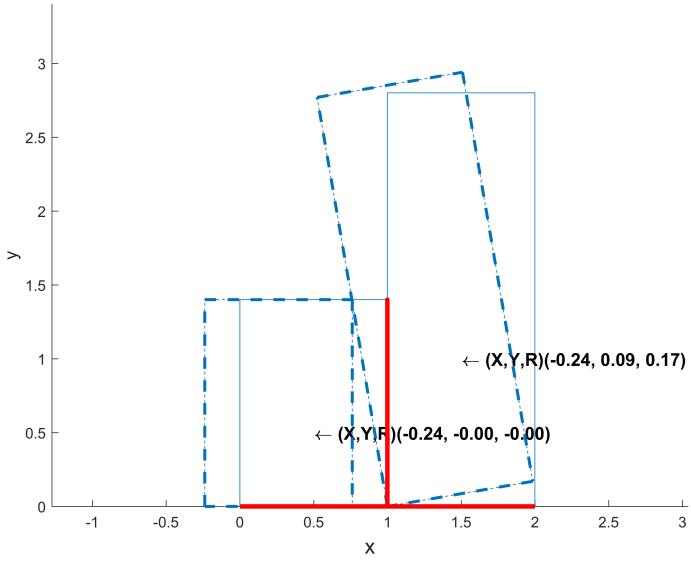

(b) NA load factor ($\lambda = 0.4061$ - 0.4288)

Figure 6.22: Collapse mechanism for two-block problem with $\Delta H/b = 1.4$. (X: Displacement rate of the block centroid in X-direction; Y: Displacement rate of the block centroid in Y-direction; R: Rotation rate of the block centroid.)

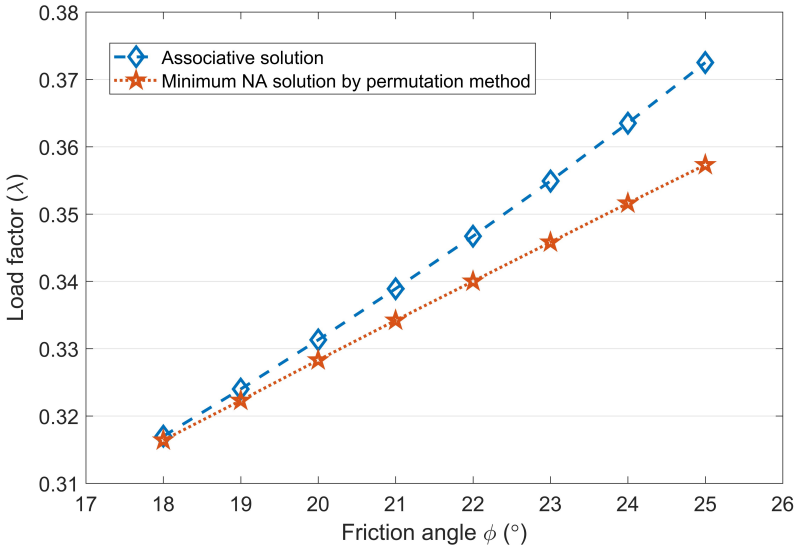

Figure 6.23: Effects of friction angle on the collapse load factor when $\Delta H/b = 1.6$.

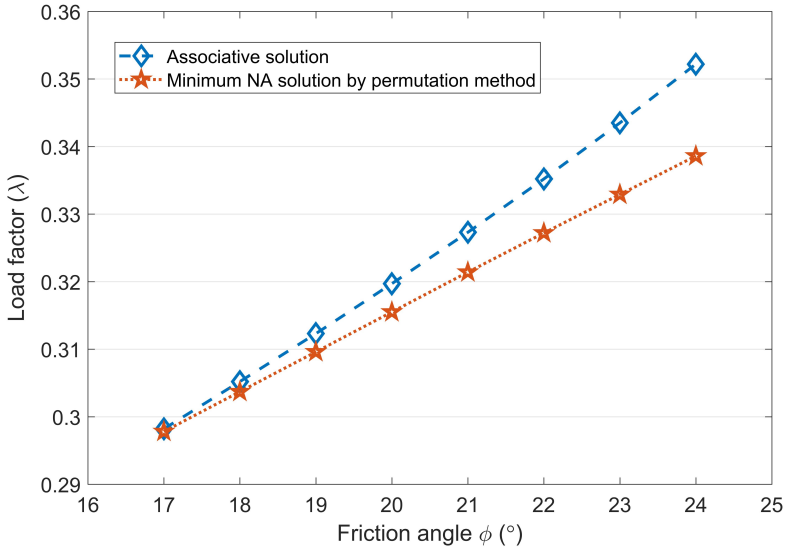

Figure 6.24: Effects of friction angle on the collapse load factor when $\Delta H/b = 1.7$.

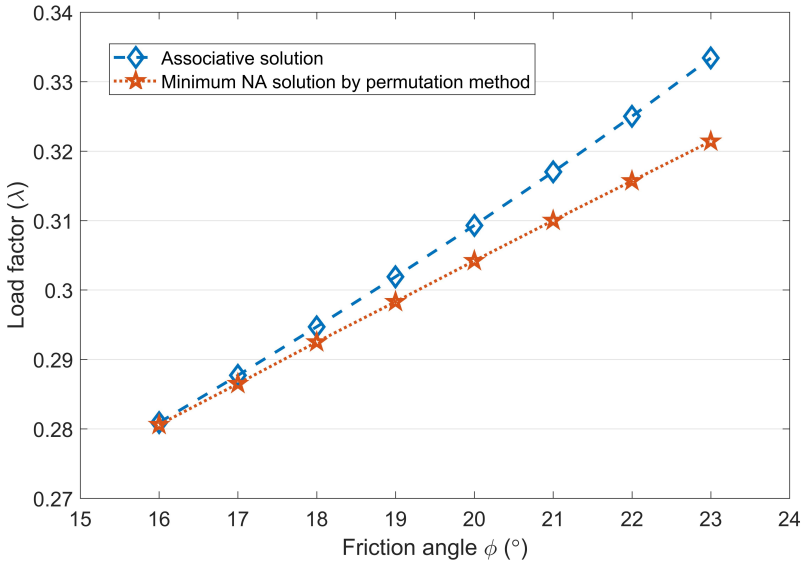

Figure 6.25: Effects of friction angle on the collapse load factor when $\Delta H/b = 1.8$.

previous solutions described in the literature.

2. Conventional associative friction limit analysis models are likely to grossly over-predict the stability of rock slopes when toppling of blocks is involved, and their use should therefore be avoided. This work shows potential to predict different physically possible case and non-associative solutions for a given geometry.

3. Taking the simple two-block problem as an example, the possible collapse kinematic mechanisms of the non-associative toppling block problems predicted by permutation method are similar to the proposed specific 'descriptive' kinematic mechanisms in existing literature.

4. The disadvantage of the proposed permutation method is that it is time-consuming for solving large-scale rigid block problems.

5. The proposed formulation can only force the movement of each joint in one direction, which cannot predict the realistic failure mechanism for more complicated problems. The movements of joints in different directions, such as sliding uphill, should be considered.

Chapter 7

Non-associative direct method for toppling block problems

7.1 Introduction

Using the permutation procedure proposed in previous chapter, all possible permutations of relative joint movements are solved by the developed LP formulation, which has been proved time-consuming. Therefore, an alternative rapid method for determining a range of non-associative solutions is proposed to reduce computation time. A series of numerical examples is presented to validate the current method, against both analytical and experimental results from the literature. When compared with other analytical and experimental results, the current work tends to provide safer estimates of the stability.

7.2 Rapid direct analysis

As discussed in Chapter 2, Babiker et al. (2014) proposed an iterative method that could determine a subset of non-associative solutions for a given problem. However the solution is not necessarily repeatable and does not always converge. Here a new procedure is proposed to overcome these difficulties. To validate the proposed

rapid direct method, the results by the proposed method will be compared with analytical and experimental results from the published literature.

The associative flow rule clearly requires $\phi_i = \psi_i$ (i.e. flow in the direction of the solid arrow shown in Figure 6.3(b)), whereas the required non-associative flow, with $\psi_i = 0$, will be in the direction indicated by the dashed arrow as shown in Figure 6.6(b). By the proposed rapid direct analysis, the non-associative collapse kinematic mechanism can be obtained from the associative formulation with $\psi_i = 0$ and cohesion $C_i = N_i \tan \phi_i$ (where N_i is from the associative equilibrium formulation). Therefore, the final non-associative solution will not only satisfy the original failure surface, but also will ensure that flow in a non-associative domain as required (the flow vector is also normal to the fictitious yield surface). This will be a valid non-associative solution and can be verified by the permutation approach.

Extending the process to all joints between blocks in the problem allows a numerical solution procedure to be developed as follows:

1. Solve the associative equilibrium formulation first to obtain indicative forces on every joint.

2. Solve the associative kinematic (displacement rate based) form setting $C_i = N_i \tan \phi_i$ (where N_i is from the previous associative solution), the dilation angle ψ_i is assumed zero.

3. Use the solution from Step 2 above to identify the kinematics of the problem, i.e. which joint is rotating, sliding, rotating and sliding, not moving relatively.

4. Use this information about kinematic mechanism from Step 3 to obtain the collapse load factor within permutation framework (using Eq. 6.9), forcing each joint to move according to the kinematics in Step 3 above.

5. This solution must be a valid non-associative result because it corresponds to the kinematics from Step 2 which are compatible for $\psi_i = 0$. The minimum non-associative load for the specific kinematic failure mechanism can be determined.

Displacement Rate	Joint 1	Joint 2	Joint 3	Joint 4	Joint 5
X-direction	0.00	-0.06	-0.06	0.00	-0.06
Y-direction	0.13	0.00	0.00	0.13	0.00
Rotation rate	0.00	0.13	-0.13	0.00	-0.13

Table 7.1: The movement of every joint in Step 2 using the proposed rapid direct approach.

For the non-associative permutation method formulation in Step 4, replacing $\min \lambda$ with $\max \lambda$ will find the maximum non-associative load thus bracketing the NA load. This is called 'Direct kinematic max-min procedure'. The above can always be extended by repeating the loop, but using $C_i = N_i \tan \phi_i$ from the previous stage 4 in a new stage 1. This iterative process may give the same answer or it may give a slightly different one. This can be repeated until a very small tolerance is obtained.

The above will work for any number of blocks and will be relatively rapid. For small numbers of blocks in the simple block problem, the permutation method will be used to validate the results by the proposed rapid direct method, as shown in Figure 6.13. The predicted minimum non-associative collapse load factor and collapse kinematic mechanism by the proposed rapid direct method are consistent with those by the permutation method.

.

7.3 Rapid direct analysis of specific problems

7.3.1 Analysis of simple block system

Taking the three-block problem as an example, the process for obtaining the minimum non-associative solution will be illustrated in detail step by step. Firstly, the force level can be obtained by using the associative equilibrium formulation assuming the friction angle $\phi = 36°$, the result is shown in Figure 7.1. In Step 2, on the basis of the associative kinematic formulation obeying the failure cri-

terion shown in Figure 6.6(b), the failure mechanism could be obtained by setting $C_i = N_i \tan \phi_i$ and zero dilation angle. For the three-block problem shown in Figure 7.1, $N_1 = 1.2584, N_2 = 0.3557, N_3 = 2.5168, N_4 = 1.0671, N_5 = 2.2247$. And the kinematics are shown in Table 7.1. From the data in Table 7.1, it can be concluded that the first joint is sliding, the second joint is rotating, the third joint is rotating, the forth joint is sliding and the last joint is rotating. Within permutation framework (using Eq. 6.9), the non-associative solution can be obtained based on the judgement of the movements of joints, shown in Figure 7.2. The non-associative solutions for the force levels are shown in Figure 7.3. Using $C_i = N_i \tan \phi_i$ and zero dilation angle, the above process could be repeated until a very small tolerance is obtained.

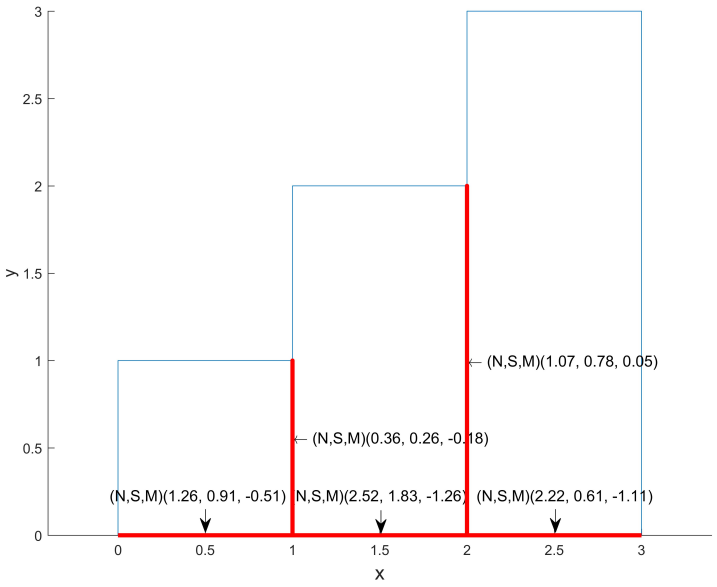

Figure 7.1: Predicted force level for associative three-block problem.(N: Normal force on the joint; S: Shear force on the joint; M: Moment on the joint.)

In the same way, the proposed rapid direct approach can be used to predict the minimum non-associative solution for the large-block problem quickly compared with the proposed permutation method (the average computation time is shown in Table 7.2). The failure mechanisms for 6, 7, 8, 9 blocks problem are shown in Figure 7.4, Figure 7.5, Figure 7.6 and Figure 7.7. It can be concluded that the

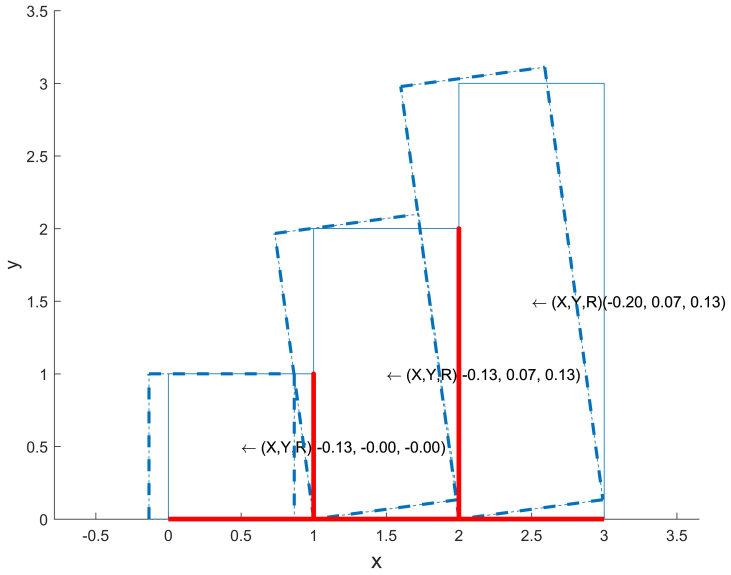

Figure 7.2: Collapse mechanism for three-block problem (minimum non-associative solution: $\lambda = 0.4564$). (X: Displacement rate of the block centroid in X-direction; Y: Displacement rate of the block centroid in Y-direction; R: Rotation rate of the block centroid.)

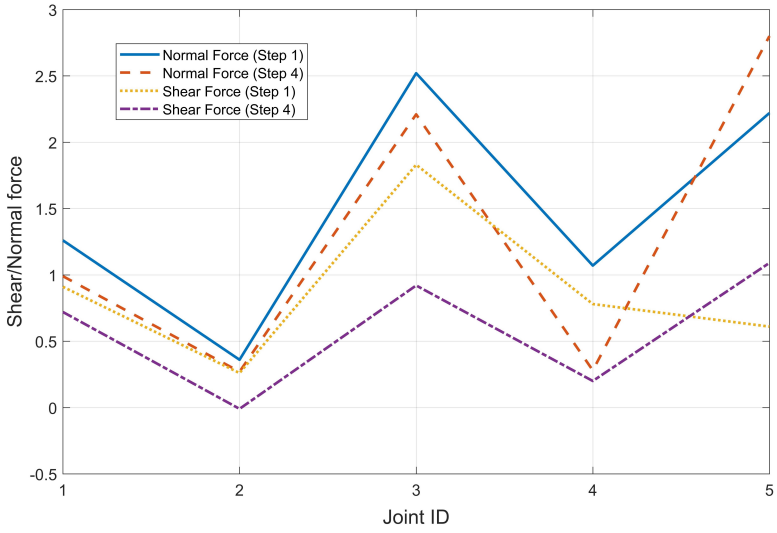

Figure 7.3: Comparison of normal and shear forces obtained from Step 1 and Step 4: three-block case.

failure mechanisms are similar: the first block slides, the other blocks rotate at the same rotation rate.

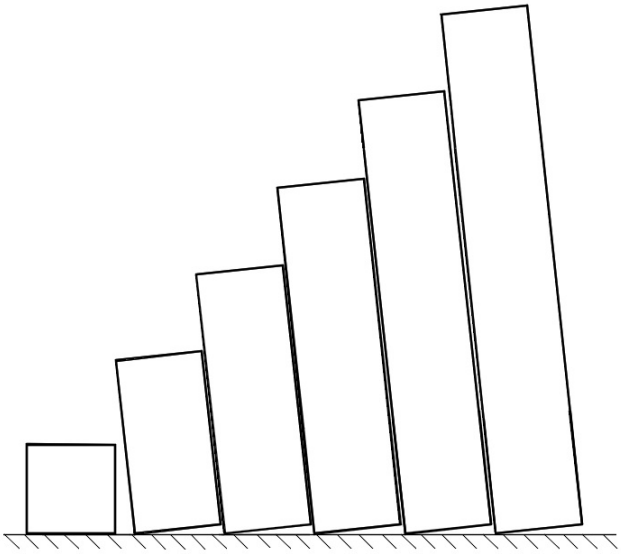

Figure 7.4: Collapse mechanism for six-block problem (minimum non-associative solution: $\lambda = 0.2832$).

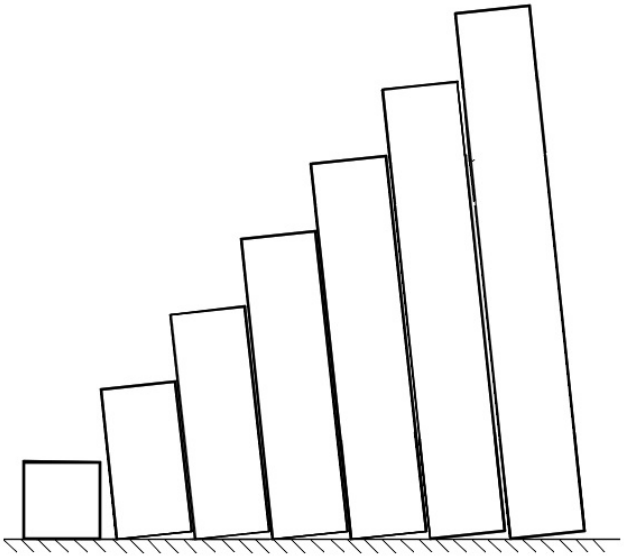

Figure 7.5: Collapse mechanism for seven-block problem (minimum non-associative solution: $\lambda = 0.2484$).

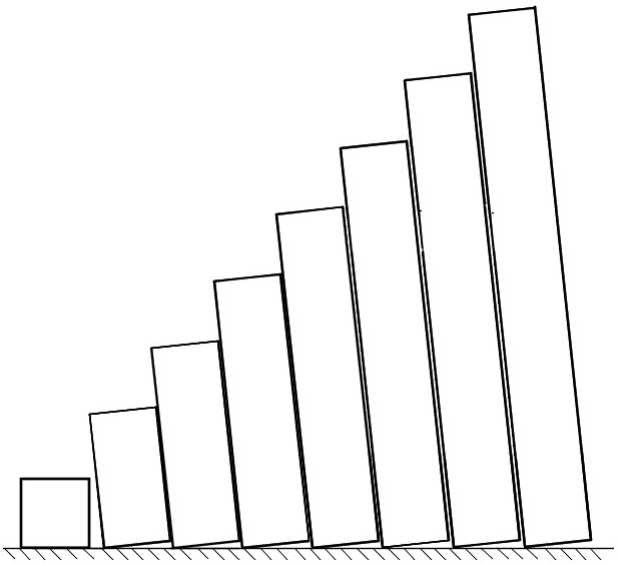

Figure 7.6: Collapse mechanism for eight-block problem (minimum non-associative solution: $\lambda = 0.2207$).

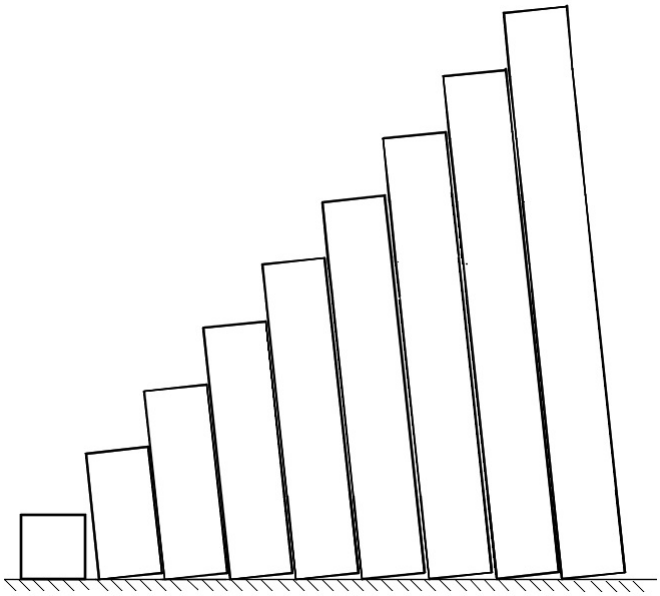

Figure 7.7: Collapse mechanism for nine-block problem (minimum non-associative solution: $\lambda = 0.1981$).

	Two-block	Three-block	Four-block	Five-block
Computation time (second)	1.2269	1.3668	1.4004	1.5210
Collapse load factor λ	0.5559	0.4564	0.3844	0.3274
λ (permutation method)	0.5559	0.4564	0.3844	0.3274
	Six-block	Seven-block	Eight-block	Nine-block
Computation time (second)	2.1877	2.3053	2.4595	2.6374
Collapse load factor λ	0.2832	0.2484	0.2207	0.1981

Table 7.2: The predicted average computation time and collapse load factor for multi-block problems.

7.3.2 Discussion of geometric variations

The proposed rapid direct method in this chapter could also address geometric variations of the simple multi-block problem and can obtain the minimum non-associative solution in a short computation time compared with the permutation method. For comparison, this section only explores the effects of different ratios of the height difference to width of the blocks on the non-associative collapse loads and failure mechanisms. As the same as the permutation analysis, the ratio of the height difference (ΔH) to width (b) of each block is assumed the same and to be a constant, as shown in Figure 6.18.

Taking the two-block problem as an example, by the proposed rapid direct method, both different values of $\Delta H/b$ (the geometry is defined in Figure 6.18) and different friction angles lead to different non-associative solutions. In order to validate the proposed rapid direct method, the comparison in minimum non-associative solution is made with the results by permutation method in Section 6.5. The effects of the friction angles on the minimum non-associative loads are shown from Figure 7.8 to Figure 7.10. It can be concluded that the collapse load factor predicted by the rapid direct method agrees well with that by the permutation method.

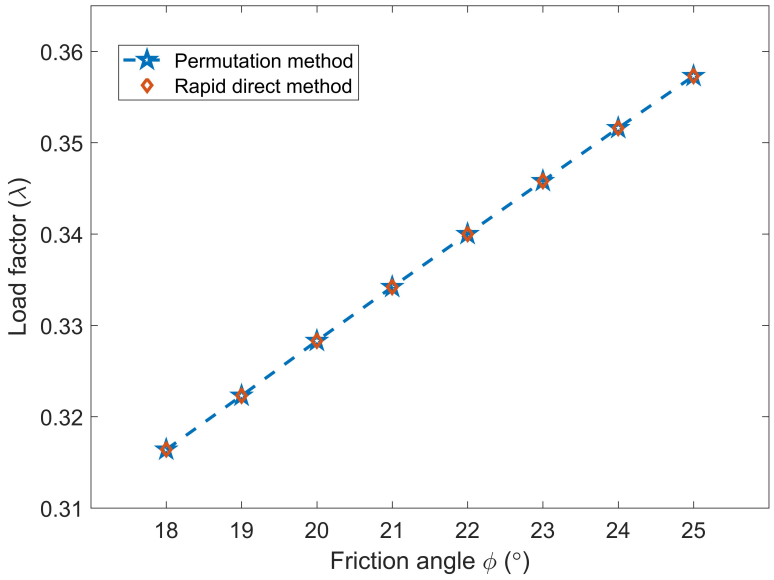

Figure 7.8: Comparison in minimum non-associative solution with $\Delta H/b = 1.6$.

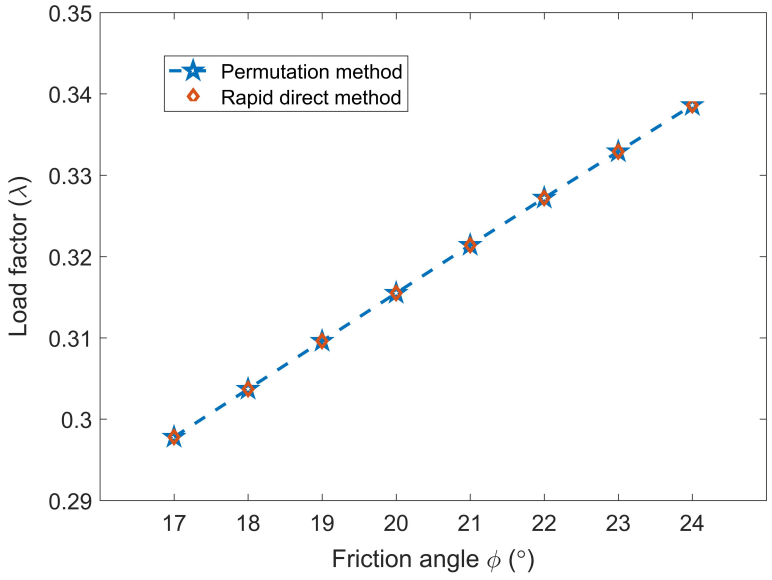

Figure 7.9: Comparison in minimum non-associative solution with $\Delta H/b = 1.7$.

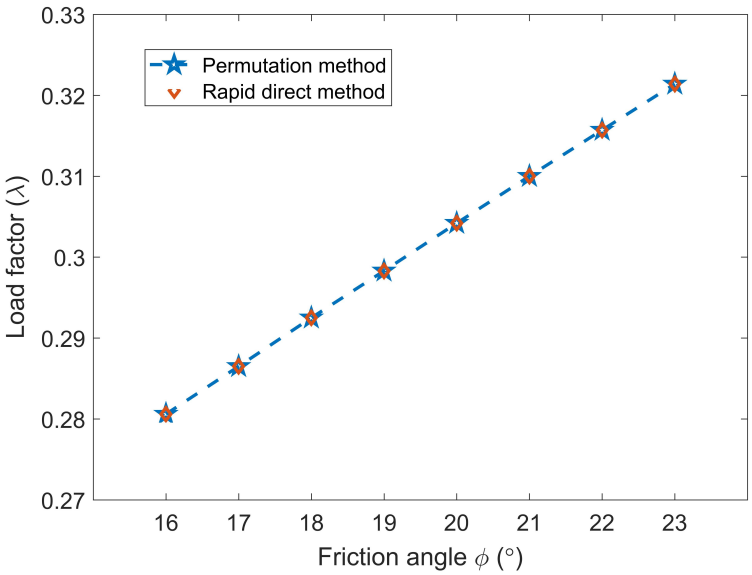

Figure 7.10: Comparison in minimum non-associative solution with $\Delta H/b = 1.8$.

7.4 Case studies

7.4.1 Example 1: stepped rock column problem (analytical)

To obtain the load factors triggering the toppling failure of rock slope in a classical problem (Goodman & Bray 1976), shown in Figure 7.11, different methods have been adopted by various researchers, such as the limit equilibrium method (Hoek & Bray 1977), limit analysis method (Babiker et al. 2014) and DEM (Koo & Chern 1998, Meng et al. 2018). The geometry for this problem is described below. A rock face 92.5 m high is cut at an angle of 56.6° in a layered rock mass dipping at 60° into the face. The width of each block is 10 m and the angle of the slope above the crest of the cut is 4°, the base of each block is stepped by 1 m. Based on this geometry, there are 16 columns formed between the toe and crest of the slope. The unit weight of the rock is 25 kN/m^3.

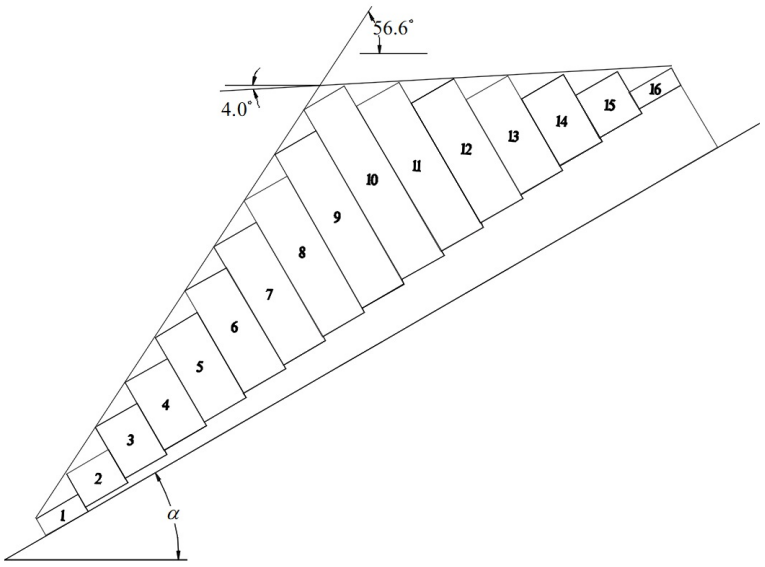

Figure 7.11: Example 1 - geometry of the rock slopes.

According to the analytical results by the limit equilibrium analysis, the top three blocks (16,15,14) are stable and the lowest three toe blocks (3,2,1) slide, while the rest of the blocks fail by toppling. The rock slope in this problem is unstable when the friction angles on the faces and bases of the blocks are 38.15°. With help of the proposed rapid direct method in this chapter, the predicted collapse mechanism is shown in Figure 7.12 when the friction angle is 38.15°. And this failure mechanism is different from that predicted by NAIM. According to the numerical results by NAIM, the top three blocks (16,15,14) are stable and the lowest two toe blocks (2,1) slide, while the rest of the blocks fail by toppling. Based on the predicted collapse mechanism by the proposed rapid direct method, when the load factor λ is preset ($\lambda = 0.5774$ in this work), the critical friction angle ϕ (required to achieve the tilt angle of 30°) can be obtained by utilising the permutation formulation (using Eq. 6.9). The result by rapid direct method shows that the critical friction angle was 46.2° for achieving the tilt angle of 30°, which provides a conservative solution compared with both limit equilibrium analysis (39°) and NAIM method (39.1°).

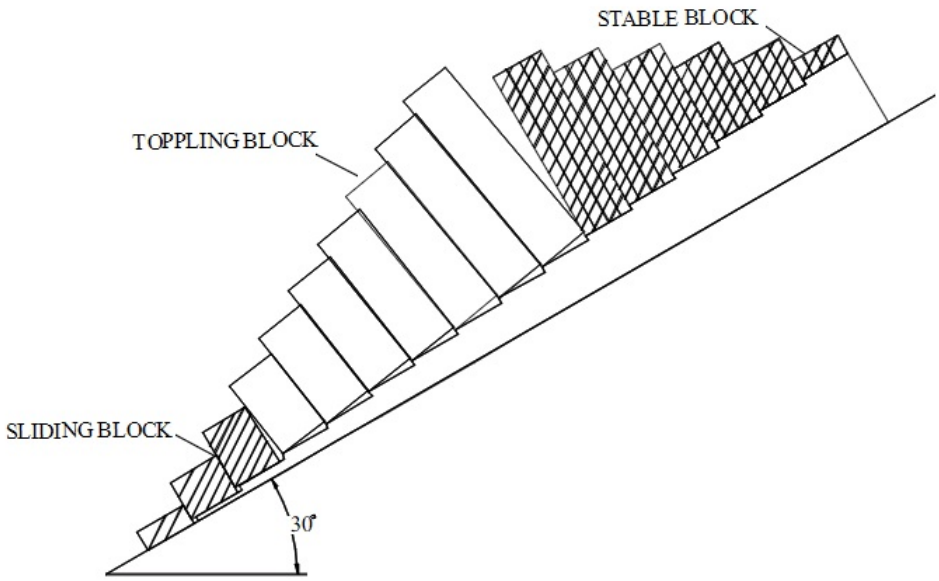

Figure 7.12: Example 1 - predicted toppling mechanism for a dip or tilt angle of 30°.

7.4.2 Example 2: Ashby's staggered joints problem (experimental)

Considering the experiments conducted by Ashby (1971), the load factor (tilt angle) of plaster blocks with an interface frictional angle of 36° is to be predicted. In this section, the staggered pattern of blocks was used which maintained a continuous but flexible column structure and produced consistent results. The basic block model geometry is illustrated in Figure 7.13. The figure shows the model which consisted of columns of blocks placed on the incline of a tilting frame. The columns of blocks were staggered like brickwork by means of half blocks placed at the base of alternate columns.

The failure mechanism for plaster blocks with an interface angle of friction of 36° can be predicted by the rapid direct approach, as shown in Figure 7.14. It can be observed that the toe blocks slide and there exists a triangular pocket of stable blocks on the base of the taller columns (the shaded blocks), the taller columns

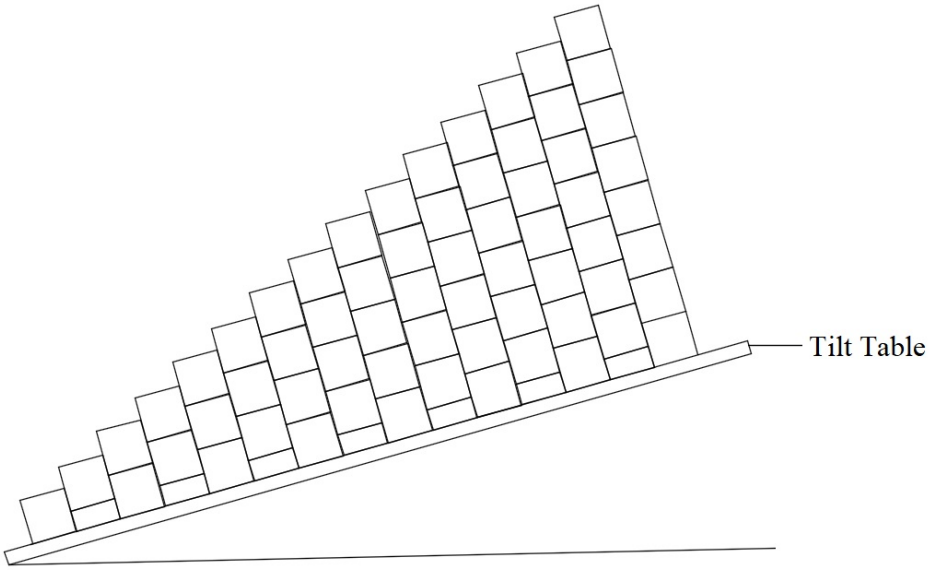

Figure 7.13: Example 2 - Geometry for staggered joints problem in Ashby's experimental work.

topple, which has similar mechanism to the experimental result. Based on the proposed rapid direct analysis, the prediction of the load factor of Ashby's staggered joints problem is shown in Figure 7.15. The same problems are modelled using the proposed 'Direct kinematic max-min procedure' and the results are compared in Figure 7.15. The results predicted by NAIM (Babiker et al. 2014) are also shown in Figure 7.15. It can be concluded that the proposed method provides a wider range for the possible non-associative solutions than Babiker's work.

As shown in Figure 7.15, the single column model fails by sliding only when the tilt angle reaches the friction angle of the base (36°). Obviously, the flow rule doesn't affect the collapse load factor triggering the slide of single block. For $\phi = 36°$, the tilt angle $\alpha = 36°$, which agrees well with the fact. As more columns are added, the tilt angle at failure reduces in experiments. However it can be concluded that when the number of block columns is bigger than 10, the numerical non-associative solutions by the proposed method are relatively insensitive to number of block columns (this is in stark contrast to the associative friction results, which

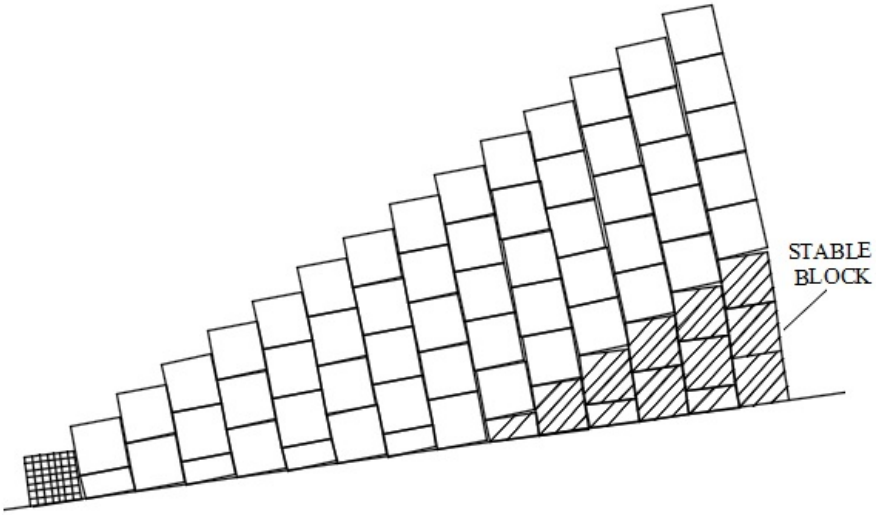

Figure 7.14: Example 2 - predicted failure mechanism for 15-column staggered joints problem in Ashby's experimental work. The shaded blocks remain stable, the hatched blocks are predicted to slide, the other blocks are predicted to topple.

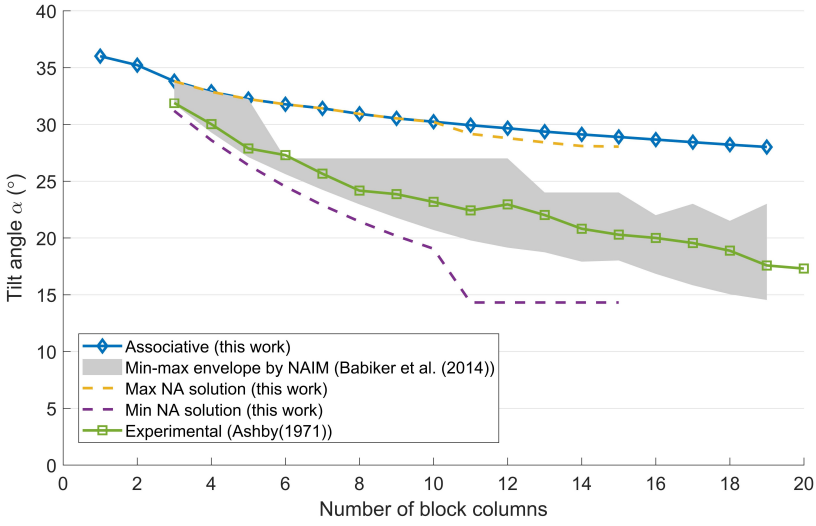

Figure 7.15: Example 2 - predicted and experimental results vs. number of columns.

suggests that stability increases with increasing of block column number) and the maximum NA results are lower than the associative results. The possible reason is that there exists a stable triangular zone (shown in Figure 7.16 and Figure 7.17) in the predicted failure mechanism when the number of block columns is bigger than 10. Compared with the experimental results, the minimum NA solutions by 'Direct kinematic max-min procedure' are always in the safe side. It could be seen that the method put forward by this work will give a safer prediction for the tilt angle at failure and the average of the minimum and maximum load factors provides a good estimation compared with the experimental results.

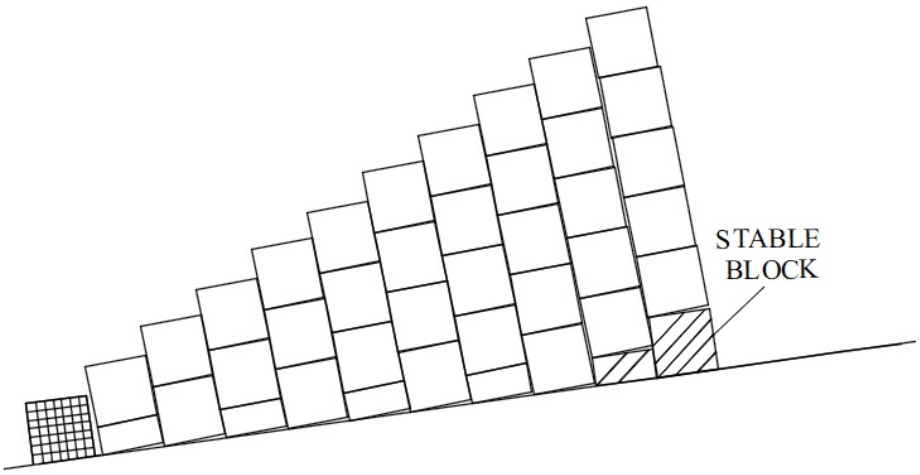

Figure 7.16: Example 2 - predicted failure mechanism for 11-column staggered joints problem in Ashby's experimental work. The shaded blocks remain stable, the hatched blocks are predicted to slide, the other blocks are predicted to topple.

In conclusion, the proposed rapid direct analysis provides reasonably good predictions of stability in the case of Ashby's staggered joints problem, and the 'Direct kinematic max-min procedure' successfully brackets all the experimental results.

7.5 Conclusions

1. A new rapid direct method for determining the range of non-associative solutions was evaluated, which is extended from a numerical iterative method for

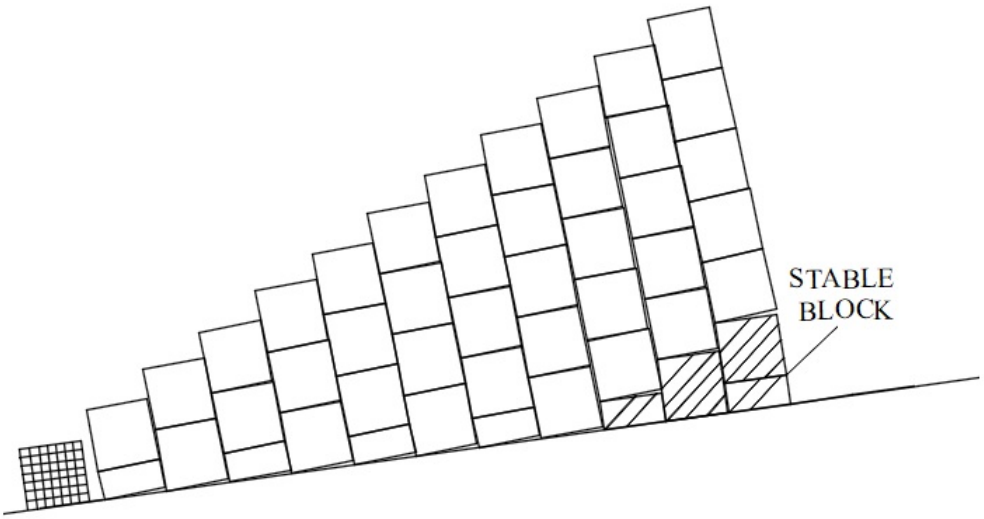

Figure 7.17: Example 2 - predicted failure mechanism for 12-column staggered joints problem in Ashby's experimental work. The shaded blocks remain stable, the hatched blocks are predicted to slide, the other blocks are predicted to topple.

determining non-associative load factors for block toppling/sliding problems. The predicted failure kinematic mechanisms by this method are similar to those observed experimentally, or obtained by analytical approach.

2. For simple block system problem with considering the geometric variations, the non-associative solutions by rapid direct approach show consistency with those by the proposed permutation method.

3. Two different examples are investigated to compare the kinematic mechanism and collapse load factor by the rapid direct approach with those by analytical and experimental methods. For the stepped rock column problem, the predicted collapse kinematic mechanism by the rapid direct method is similar to that by the analytical method, but the predicted critical friction angle leading to instability is bigger than that by the analytical method. For the staggered joints problem, the average of the minimum and maximum load factors provides a good estimation compared with the experimental results.

Chapter 8

Discussion

8.1 Introduction

This chapter is an opportunity to review the results in the overall context of the thesis, to discuss the advantages and disadvantages of the proposed methods and to reflect on the results in terms of the general topic area and the wider engineering aspects.

8.2 Summary of work

The aim of the thesis was to propose models that are both simple and realistic for limit analysis in practical engineering. Inspired by the discontinuity based numerical limit analysis, new methods are proposed considering non-linear and non-associative yield conditions, respectively. The advantage of the proposed methodology is that the procedures are easy to follow since they share strong similarities to conventional methodology using linear and associative yield conditions. Some examples have been conducted to show the proposed methodology provides safer estimations for the collapse of soils and rocks in real engineering. The proposed methodology also shows potential to be applied to DLO, which is a convenient method for engineers to obtain the limit loads and failure mechanisms with a good

balance of accuracy and efficiency.

8.3 Solution of limit analysis problems with a non-linear yield surface

For real soils, the assumption of linear behaviour is an idealisation and non-linear behaviour can be significant for some soils and fractured rock systems. In this thesis, two different methods are used to conduct the stability analysis of soils with a non-linear failure criterion: (1) multi-tangent non-linear method and (2) general variational method. Some key issues relating to the solutions of the proposed non-linear methods are discussed below.

8.3.1 Prediction of the normal stress distribution for multi-tangent DLO method

The multi-tangent DLO technique appears equally valid and good at generating results as the general variational approach and is more general. It may however require a 2 stage process to obtain the limit load and related failure mechanism on the basis of non-linear yield function. The first stage is to establish the range of normal stresses to be modelled in the problem, the second stage is to determine the optimal locations of tangency points based on the proposed 'Minimum Area' technique. One limitation of the multi-tangent DLO method is that it cannot produce normal stress distributions along the full lengths of the slip-lines directly. Therefore it is difficult to use the multi-tangent DLO method for complicated geotechnical problems for which it is hard for engineers to get the normal stress distribution according to practical experience.

The scope to use the variational method to generate stress distributions for essentially linear and non-linear problems has been demonstrated. Results so far indicate that these are credible values, consistent with results from other analysis methods. Further work is required to establish the conditions under which this is valid. Initial recommendations have been given for choice of the parameters describing both linear and non-linear yield functions, such as m, c_0 and σ_t.

8.3.2 Further robust validation for the general variational method

Taking the smooth retaining wall problem (both in static and seismic conditions) and anchor problem as examples, the limit loads predicted by the 'multi-tangent method' are compared with those by the variational method, whose differences are less than 2.5 percent. Any variation is probably due to the discretised nature of the analysis. However more work required to prove validity (or conditions when values are valid) for all cases. Additionally a sensitivity analysis should be conducted for the numerical tolerance and non-optimality of solution.

8.3.3 Incorporation of the variational method into DLO domain

There is significant scope to incorporate the variational method into the DLO framework in such a way that the 'slip-line global dilation' becomes an additional optimization parameter. For this optimization process, the first step is to determine the layout of the secant connecting the endpoints of the curve, then the variables for determining the global dilation angle and displacement rates can be optimized. The stress distribution at every single point along discontinuities can then be predicted, which provides potential to generate a stress field to calculate the related

lower bound solution.

8.4 Solution of limit analysis type problems with a non-associative flow rule

Most limit analysis approaches assume an associative flow rule in order to avoid the numerical complexity that arises if a non-associative flow rule is used. However, the non-associative phenomenon can not be ignored by engineers, especially for the stability prediction of rock toppling problems in real engineering. This thesis proposed two approaches to examine in detail the non-associative analysis of a classic toppling block problem considering a low dilation model: (1) permutation method and (2) rapid direct method. Some key issues relating to the solution of the proposed non-associative methods are discussed below.

8.4.1 Reduction of the number of permutations

The permutation method is promising in that it can potentially identify every possible distinct non-associative failure mechanism. The proposed 'max-min method' combined with the permutation approach was successfully applied to establish ranges of possible loads that could lead to collapse of the NA mechanisms for simple multi-block problems. However its limitation is that the number of permutations increases rapidly with the increasing number of blocks, thus limiting the scope to 6 or 7 blocks in a simple multi-block system. However there may be scope for making the search more efficient by limiting joint movements to credible values (at the risk of missing something unexpected) or finding more solutions by searching subsets of deformation modes (e.g. relative to kinematics found by another approach). For the simple two-block problem discussed in Section 6.4, the number

of permutations can be reduced by the analysis of the movements of the adjacent horizontal joints. In this way, all possible permutations (64 cases in total) can be reduced to only 6 cases, which makes the proposed permutation method more efficient. While the method was successfully demonstrated in this thesis, it was not able to find more than one non-associative mechanism in the problems studied. Further work is required to investigate more complex arrangements of blocks and demonstrate the ability of the method to find multiple distinct mechanisms.

8.4.2 Finding valid kinematics using the rapid direct method

The rapid direct method was demonstrated to work well for the example studies undertaken generating credible mechanisms and results very quickly. This is in contrast to e.g. NAIM which can require many iterations and may not converge consistently. It also tended to find a wider range of possible loads for some specific problems than NAIM when used in conjunction with the 'max-min procedure', e.g. Ashby's staggered joints problem. However while generally robust, the rapid direct method may fail to find a solution if the kinematics cannot be made to fit the required NA equilibrium. However there may be scope to model a series of successive problems with incrementally increasing friction angle so that valid kinematics can be modelled at each stage building on the results from the previous stage.

8.4.3 Extension to more general non-associative cases with non-zero dilation

Most analyses were presented for the zero-dilation case. It is noted that for many of the simple block toppling problems a distinct NA result is only possible for zero-dilation. For the zero dilation case, the feasible solution is one where kinematics are similar to those for cohesive material (obeys the associative flow rule natur-

ally). The proposed kinematic formulation is valid since it is modified from the associative formulation. However the proposed non-associative methods cannot predict some kinematic mechanisms caused by non-zero dilation accurately. For the two block problem, relative (sliding) movement between the blocks can only occur if the first block is sliding on the base with dilation. This forces mobilization of full shear strength on the inter-block interface. Only if there is zero dilation on the sliding block base, is there no relative sliding movement between the two blocks. This makes the two block problem a special case with sudden change in behaviour from zero to non-zero dilation. In limit analysis, relative displacement is required to mobilise full shear strength on an interface. If the relative displacement is zero then the shear stress can have any value smaller than the absolute value of shear strength. Taking the five-block problem in Section 6.4.2 as an example, the associative kinematic mechanism ($\lambda = 0.5008$) can be predicted directly by the kinematic form of the associative primal formulation. The minimum non-associative kinematic mechanism caused by zero dilation ($\lambda = 0.3274$) can also be predicted by the proposed non-associative kinematic formulation. However, for some minimum non-associative solution ($\lambda = 0.4459$), the calculations for displacement rates are more complicated for non-zero dilation case because both dilation and friction calculations need to be performed. The interesting question is whether this effect occurs also in complex multi-block problems or whether a NA result with small dilation is still smaller than the associative result. A more generalized formulation should be developed to solve non-zero dilation problem.

8.5 Combined non-linear and non-associative analysis

This thesis proposed different methods to apply the limit analysis method to non-linear and non-associative yield conditions, respectively. However, no general methods were proposed combining both a non-linear yield function with a

non-associative analysis. An interesting question is whether they can be combined. This very much depends on whether the problem is discrete or continuum:

For a discrete problem with pre-defined slip-planes, variable friction can be modelled along a straight line. Variable dilation would imply some kind of additional rotation, which would make an interesting future study.

For a continuum problem, assuming issues for linear non-associativity have been addressed, the problem is similar to that for the discrete above, but with many possible slip-lines. Zero-dilation (straight slip-lines) may be easier to handle than non-linear non-associative dilation. Optimization may not be directly applicable in this case and the rapid direct method may be required.

8.6 Application in practice

Acknowledging the non-linear nature of geo-materials can be significant in practice (e.g. the smooth retaining wall analysis). As discussed in Section 4.6, different shapes of yield functions lead to different active thrusts, which demonstrates the non-linear yield functions play key roles of the determinations of active thrusts. The variational method is a purely theoretical way to apply limit analysis method using the power-law non-linear yield function. However, this thesis only considered the curved yield function in power-law form and it is necessary to convert other widely-used yield functions (i.e. Hoek-Brown failure criterion) into the power-law form. Different yield functions (the yield surface should be convex and smooth) in different forms could also be considered. Furthermore, a linear material can also be approximated by the proposed non-linear method assuming the non-linear coefficient $m = 1.001$. Taking a smooth retaining wall analysis as an example, the difference in earth pressure between non-linear solution assuming $m = 1.001$ and

purely linear solution is around 0.35 percent. Through the sensitivity analysis in Section 4.6, the predicted limit active thrust increases with the increase of non-linear coefficient m and the non-linear solutions are bigger than linear solutions, which reflects that the non-linear method provides safer limit loads estimations for both static and seismic conditions.

It requires additional work by the engineer to determine the nature of the yield surface in the first place which itself will be subject to uncertainties. However as greater understanding of non-linear geo-materials is achieved this should become easier in the future.

There remains the general question of 'what is the correct NA collapse load?' The answer is probably that all are possible, but may have different probabilities and may be loading path dependent and may also be sensitive to minor geometrical variations in the problem. It may be possible to investigate the latter with the methods outlined in the thesis, but path dependence would probably require incremental methods.

Chapter 9

Conclusions and future work

9.1 Conclusions

1. An overview of a fully general variational approach for the upper bound analysis of stability problems in non-linear soils has been presented. The analysis follows the form of the classic upper bound multi-wedge analysis utilised for linear soils. A single wedge analysis for the smooth retaining wall problem has been investigated both in static and seismic conditions. A multi-wedge analysis for an anchor problem and cohesive backfill against smooth retaining wall problem are also conducted in detail.

2. The upper bound solutions generate good predictions of shear and normal stresses along multiple slip-lines for the problems investigated in this thesis, which is not normally obtained from an upper bound analysis and show strong consistency with related lower bound solutions. This provides a potentially useful way to extract more information from upper bound solutions when modelling linear and non-linear materials.

3. A DLO procedure using several linear yield surfaces to encompass the non-linear surface is used to validate the results by variational multi-wedge analysis in this thesis. This multi-tangent technique can be applied for failure analysis of different soil types in practical engineering.

4. Extended from the basic formulation used to tackle the associative toppling block problem, a new permutation method is proposed by arranging and combining possible movements of the joints connecting blocks. This approach shows potential to predict different physically possible non-associative results and thus generates different collapse kinematic mechanism from the associative case. The proposed 'max-min method' generates solutions that agree well with previous solutions for the simple block system analysis. The effects of geometric variations of the simple block problem on the collapse kinematic mechanism and collapse load factors are discussed.

5. A new rapid direct method for determining the range of non-associative solutions for block toppling/sliding problems is presented. The predicted failure kinematic mechanisms by this method are similar to those observed experimentally, or obtained by analytical approach. For simple block system analysis with geometric variations, the zero dilation kinematic mechanisms predicted by the rapid direct approach are consistent with those by permutation approach.

9.2 Future work

1. A general solution procedure for generating multi-wedge rigid block mechanisms is proposed by this thesis. While this thesis discussed only two-wedge failure mechanisms, further work is required to demonstrate the capability for more complex multi-wedge problems such as a rough retaining wall.

2. There is significant scope to incorporate the non-linear variational analysis within the DLO framework by introducing an additional 'dilation' parameter into the optimization.

3. The multi-tangent non-linear DLO method has only been verified with the variational method for simple examples: such as the smooth retaining wall

problem and anchor problem (where the normal stress distributions can be predicted). More validations are needed to check the proposed methods, particularly for more complicated geotechnical engineering problems which are not easy to predict the normal stress distribution.

4. For variational non-linear analysis, only translational failure was considered; however it should be possible to extend this to rotational mechanism with future work.

5. Like some other non-associative formulations, the collapse load factors predicted by the proposed non-associative permutation approach and rapid direct approach are not unique. More physical and mathematical investigations are required to fully expose the issues around non-associativity.

6. The developed non-associative formulation for rigid block problems can be applied in a three-dimensional context.

7. In order to make the developed non-associative analysis of rigid block problem useful in engineering, realistic soil models must be developed and ideally a database of these created.

References

Adhikary, D., Dyskin, A., Jewell, R. & Stewart, D. (1997), 'A study of the mechanism of flexural toppling failure of rock slopes', *Rock Mechanics and Rock Engineering* 30(2), 75–93.

Anderheggen, E. & Knöpfel, H. (1972), 'Finite element limit analysis using linear programming', *International Journal of Solids and Structures* 8(12), 1413–1431.

Anyaegbunam, A. J. (2013), 'Nonlinear power-type failure laws for geomaterials: Synthesis from triaxial data, properties, and applications', *International Journal of Geomechanics* 15(1), 04014036.

Ashby, J. (1971), Sliding and toppling modes of failure in models and jointed rock slopes, Master's thesis, Department of Mining, Imperial College of Science and Technology, London.

Babiker, A. (2013), Limit analysis using a non-associative flow rule, PhD thesis, Department of Civil and Structural Engineering, University of Sheffield, Sheffield.

Babiker, A. F. A., Smith, C. C., Gilbert, M. & Ashby, J. P. (2014), 'Non-associative limit analysis of the toppling-sliding failure of rock slopes', *International Journal of Rock Mechanics and Mining Sciences* 71, 1–11.

Baggio, C. & Trovalusci, P. (2000), 'Collapse behaviour of three-dimensional brick-block systems using non-linear programming', *Structural Engineering and Mechanics* 10(2), 181.

Baker, R. (2003), 'Inter-relations between experimental and computational aspects of slope stability analysis', *International Journal for Numerical and Analytical Methods in Geomechanics* 27(5), 379–401.

Baker, R. (2004), 'Nonlinear Mohr envelopes based on triaxial data', *Journal of Geotechnical and Geoenvironmental Engineering* 130(5), 498–506.

Baker, R. & Frydman, S. (1983), 'Upper bound limit analysis of soil with non-linear failure criterion', *Soils and Foundations* 23(4), 34–42.

Bolton, M. (1981), 'Limit state design in geotechnical engineering', *Ground Engineering* 14(6), 39–46.

Bolton, M. (1986), 'The strength and dilatancy of sands', *Géotechnique* 36(1), 65–78.

Bottero, A., Negre, R., Pastor, J. & Turgeman, S. (1980), 'Finite element method and limit analysis theory for soil mechanics problems', *Computer Methods in Applied Mechanics and Engineering* 22(1), 131–149.

Charles, J. & Soares, M. (1984), 'Stability of compacted rockfill slopes', *Géotechnique* 34(1), 61–70.

Charles, J. & Watts, K. (1980), 'The influence of confining pressure on the shear strength of compacted rockfill', *Géotechnique* 30(4), 353–367.

Chen, W. (1975), *Limit analysis and soil plasticity*, Elsevier Scientific Publishing, Amsterdam.

Chen, W.-F. & Liu, X. (1990), *Limit Analysis in Soil Mechanics*, Developments in Geotechnical Engineering 52, Elsevier.

Chen, W. & Scawthorn, C. (1968), Limit analysis and limit equilibrium solutions in soil mechanics, Technical report, Fritz Engineering Laboratory, Department of Civil Engineering, Lehigh University.

Collins, I. (1969), 'The upper bound theorem for rigid/plastic solids generalized to include coulomb friction', *Journal of the Mechanics and Physics of Solids* 17(5), 323–338.

Collins, I. F., Gunn, C. I. M., Pender, M. J. & Yan, W. (1988), 'Slope stability analyses for materials with a non-linear failure envelope', *International Journal for Numerical and Analytical Methods in Geomechanics* 12(5), 533–550.

Cox, A. (1963), *The use of non-associated flow rule in soil plasticity*, Royal Armament Research and Development Establishment.

Crotty, J. & Wardle, L. (1985), Boundary integral analysis of piecewise homogeneous media with structural discontinuities, *in* 'International Journal of Rock Mechanics and Mining Sciences & Geomechanics Abstracts', Vol. 22, Elsevier, pp. 419–427.

Das, B. M. (2008), *Advanced Soil Mechanics*, Taylor & Francis.

Davis, E. H. (1968), Theory of plasticity and the failure of soil masses, *in* 'I. K. Lee, ed., Soil Mechanics: Selected Copies', Butterworths, London, pp. 341–380.

Davis, R. O. & Selvadurai, A. P. (2002), *Plasticity and Geomechanics*, Cambridge University Press.

Day, R. W. & Axten, G. W. (1989), 'Surficial stability of compacted clay slopes', *Journal of Geotechnical Engineering* 115(4), 577–580.

De Borst, R. & Vermeer, P. (1984), 'Possibilites and limitations of finite elements for limit analysis', *Géotechnique* 34(2), 199–210.

De Freitas, M. & Watters, R. (1973), 'Some field examples of toppling failure', *Géotechnique* 23(4), 495–513.

De Josselin De Jong, G. (1959), Statics And Kinematics In The Failable Zone Of Granular Material, PhD thesis, University of Delft.

De Mello, V. F. (1977), 'Reflections on design decisions of practical significance to embankment dams', *Géotechnique* 27(3), 281–355.

Drescher, A. & Christopoulos, C. (1988), 'Limit analysis slope stability with nonlinear yield condition', *International Journal for Numerical and Analytical Methods in Geomechanics* 12(3), 341–345.

Drescher, A. & De Jong, G. D. J. (1972), 'Photoelastic verification of a mechanical model for the flow of a granular material', *Journal of the Mechanics and Physics of Solids* 20(5), 337–340.

Drescher, A. & Detournay, E. (1993), 'Limit load in translational failure mechanisms for associative and non-associative materials', *Géotechnique* 43(3), 443–456.

Drucker, D. C. (1953), 'Limit analysis of two and three dimensional soil mechanics problems', *Journal of the Mechanics and Physics of Solids* 1(4), 217–226.

Drucker, D. C. (1957), A definition of stable inelastic material, Technical report, Brown University, Providence, Rhode Island.

Drucker, D., Prager, W. & Greenberg, H. (1952), 'Extended limit design theorems for continuous media', *Quarterly of Applied Mathematics* 9(4), 381–389.

Ferris, M. & Tin-Loi, F. (2001), 'Limit analysis of frictional block assemblies as a mathematical program with complementarity constraints', *International Journal of Mechanical Sciences* 43(1), 209–224.

Fraldi, M. & Guarracino, F. (2009), 'Limit analysis of collapse mechanisms in cavities and tunnels according to the Hoek–Brown failure criterion', *International Journal of Rock Mechanics and Mining Sciences* 46(4), 665–673.

Fraldi, M. & Guarracino, F. (2010), 'Analytical solutions for collapse mechanisms in tunnels with arbitrary cross sections', *International Journal of Solids and Structures* 47(2), 216–223.

Gilbert, M., Casapulla, C. & Ahmed, H. (2006), 'Limit analysis of masonry block structures with non-associative frictional joints using linear programming', *Computers and Structures* 84, 873–887.

Gilbert, M. & Melbourne, C. (1994), 'Rigid-block analysis of masonry structures', *Structural engineer* 72(21).

Goodman, R. & Bray, J. (1976), Toppling of rock slopes, *in* 'ASCE Speciality Conference on Rock Engineering for Foundation and Slopes, Boulder, Colorado', ASCE, pp. 201–234.

Goodman, R. E., Taylor, R. L. & Brekke, T. L. (1968), 'A model for the mechanics of jointed rock', *Journal of Soil Mechanics & Foundations Div* 94, 637–659.

Hill, R. (1950), *The Mathematical Theory of Plasticity*, Oxford Classic Texts in the Physical Sciences Series, Clarendon Press.

Hoek, E. (1990), Estimating Mohr-Coulomb friction and cohesion values from the Hoek-Brown failure criterion, *in* 'Intnl. J. Rock Mech. & Mining Sci. & Geomechanics Abstracts', Vol. 12, pp. 227–229.

Hoek, E. (1994), 'Strength of rock and rock masses', *ISRM News Journal* 2(2), 4–16.

Hoek, E. & Bray, J. (1977), 'Rock slope engineering, 2nd edn', *The Institution of Mining and Metallurgy, London* .

Hoek, E. & Brown, E. T. (1997), 'Practical estimates of rock mass strength', *International Journal of Rock Mechanics and Mining Sciences* 34(8), 1165–1186.

Hoek, E., Kaiser, P. & Bawden, W. (1995), 'Support of underground excavations in hard rock., 1995', *AA Balkema, Rotterdam* .

Ishida, T., Chigira, M. & Hibino, S. (1987), 'Application of the distinct element method for analysis of toppling observed on a fissured rock slope', *Rock Mechanics and Rock Engineering* 20(4), 277–283.

Jiang, J.-C., Baker, R. & Yamagami, T. (2003), 'The effect of strength envelope nonlinearity on slope stability computations', *Canadian Geotechnical Journal* 40(2), 308–325.

Jiang, Q. & Zhou, C. (2017), 'A rigorous solution for the stability of polyhedral rock blocks', *Computers and Geotechnics* 90, 190–201.

Knappett, J. & Craig, R. (2012), *Craig's Soil Mechanics*, Taylor & Francis.

Koo, C. & Chern, J.-C. (1998), 'Modification of the DDA method for rigid block problems', *International Journal of Rock Mechanics and Mining Sciences* 35(6), 683–693.

Krabbenhøft, K., Lyamin, A. & Sloan, S. (2007), 'Formulation and solution of some plasticity problems as conic programs', *International Journal of Solids and Structures* 44(5), 1533–1549.

Krabbenhøft, K., Lyamin, A. V. & Sloan, S. W. (2008), 'Three-dimensional Mohr–Coulomb limit analysis using semidefinite programming', *Communications in Numerical Methods in Engineering* 24(11), 1107–1119.

Lade, P. V. (2002), 'Instability, shear banding, and failure in granular materials', *International Journal of Solids and Structures* 39, 3337–3357.

Lanaro, F., Jing, L., Stephansson, O. & Barla, G. (1997), 'D.E.M. modelling of laboratory tests of block toppling', *International Journal of Rock Mechanics and Mining Sciences* 34, 173.e1–173.e15.

Lefebvre, G. (1981), 'Fourth Canadian Geotechnical Colloquium: Strength and slope stability in Canadian soft clay deposits', *Canadian Geotechnical Journal* 18(3), 420–442.

Li, X. (2007), 'Finite element analysis of slope stability using a nonlinear failure criterion', *Computers and Geotechnics* 34(3), 127–136.

Livesley, R. K. (1978), 'Limit analysis of structures formed from rigid blocks', *International Journal for Numerical Methods in Engineering* 12(12), 1853–1871.

Lyamin, A. & Sloan, S. (2002*a*), 'Lower bound limit analysis using non-linear programming', *International Journal for Numerical Methods in Engineering* 55(5), 573–611.

Lyamin, A. V. & Sloan, S. (2002*b*), 'Upper bound limit analysis using linear finite elements and non-linear programming', *International Journal for Numerical and Analytical Methods in Geomechanics* 26(2), 181–216.

Lysmer, J. (1970), 'Limit analysis of plane problems in soil mechanics', *Journal of Soil Mechanics & Foundations Div* 96, 1311–1334.

Maier, G., Zavelani-Rossi, A. & Benedetti, D. (1972), 'A finite element approach to optimal design of plastic structures in plane stress', *International Journal for Numerical Methods in Engineering* 4(4), 455–473.

Makrodimopoulos, A. & Martin, C. (2006), 'Lower bound limit analysis of cohesive-frictional materials using second-order cone programming', *International Journal for Numerical Methods in Engineering* 66(4), 604–634.

Makrodimopoulos, A. & Martin, C. (2007), 'Upper bound limit analysis using simplex strain elements and second-order cone programming', *International Journal for Numerical and Analytical Methods in Geomechanics* 31(6), 835–865.

Makrodimopoulos, A. & Martin, C. (2008), 'Upper bound limit analysis using discontinuous quadratic displacement fields', *Communications in Numerical Methods in Engineering* 24(11), 911–927.

Maksimovic, M. (1989), 'Nonlinear failure envelope for soils', *Journal of Geotechnical Engineering* 115(4), 581–586.

Mehrabadi, M. & Cowin, S. (1978), 'Initial planar deformation of dilatant granular materials', *Journal of the Mechanics and Physics of Solids* 26(4), 269–284.

Meng, J., Huang, J., Sloan, S. & Sheng, D. (2018), 'Discrete modelling jointed rock slopes using mathematical programming methods', *Computers and Geotechnics* 96, 189–202.

Mononobe, N. (1929), On determination of earth pressure during earthquake, *in* 'Proc. World Engineering Congress', Vol. 9, pp. 177–185.

Murray, E. & Geddes, J. D. (1987), 'Uplift of anchor plates in sand', *Journal of Geotechnical Engineering* 113(3), 202–215.

Perry, J. (1994), 'A technique for defining non-linear shear strength envelopes, and their incorporation in a slope stability method of analysis', *Quarterly Journal of Engineering Geology and Hydrogeology* 27(3), 231–241.

Roscoe, K. H. (1970), 'The influence of strains in soil mechanics', *Géotechnique* 20(2), 129–170.

Sadrekarimi, A. & Olson, S. M. (2011), 'Critical state friction angle of sands', *Géotechnique* 61(9), 771–783.

Sagaseta, C., Sanchez, J. & Canizal, J. (2001), 'A general analytical solution for the required anchor force in rock slopes with toppling failure', *International Journal of Rock Mechanics and Mining Sciences* 38(3), 421–435.

Sarfaraz, H. & Amini, M. (2019), 'Numerical modeling of rock slopes with a potential of block-flexural toppling failure', *Journal of Mining and Environment* (Articles in Press).

Shi, G.-H. (1992), 'Discontinuous deformation analysis: a new numerical model for the statics and dynamics of deformable block structures', *Engineering Computations* 9(2), 157–168.

Shukla, S. K. (2015), 'Generalized analytical expression for dynamic active thrust from c–φ soil backfills', *International Journal of Geotechnical Engineering* 9(4), 416–421.

Sloan, S. (1988), 'Lower bound limit analysis using finite elements and linear programming', *International Journal for Numerical and Analytical Methods in Geomechanics* 12(1), 61–77.

Sloan, S. (1989), 'Upper bound limit analysis using finite elements and linear programming', *International Journal for Numerical and Analytical Methods in Geomechanics* 13(3), 263–282.

Sloan, S. (2013), 'Geotechnical stability analysis', *Géotechnique* 63(7), 531–571.

Smith, C. C. (1998), 'Limit loads for an anchor/trapdoor embedded in an associative Coulomb soil', *International Journal for Numerical and Analytical Methods in Geomechanics* 22(11), 855–865.

Smith, C. C. & Gilbert, M. (2015), 'Modelling rotational failure in confined geometries using DLO', *Proceedings of the Institution of Civil Engineers-Engineering and Computational Mechanics* 168(4), 155–168.

Smith, C. & Cubrinovski, M. (2011), 'Pseudo-static limit analysis by discontinuity layout optimization: application to seismic analysis of retaining walls', *Soil Dynamics and Earthquake Engineering* 31(10), 1311–1323.

Smith, C. & Gilbert, M. (2007), 'Application of discontinuity layout optimization to plane plasticity problems', *Proceedings of the Royal Society A: Mathematical, Physical and Engineering Sciences* 463(2086), 2461–2484.

Smith, C. & Gilbert, M. (2010), Advances in computational limit state analysis and design, *in* 'GeoFlorida 2010: Advances in Analysis, Modeling & Design', pp. 119–128.

Smith, C. & Gilbert, M. (2013), 'Identification of rotational failure mechanisms in cohesive media using discontinuity layout optimisation', *Géotechnique* 63(14), 1194–1208.

Smoltczyk, U. (2003), *Geotechnical Engineering Handbook, Procedures*, Geotechnical Engineering Handbook, John Wiley & Sons.

Soon, S.-C. & Drescher, A. (2007), 'Nonlinear failure criterion and passive thrust on retaining walls', *International Journal of Geomechanics* 7(4), 318–322.

Spencer, A. (1964), 'A theory of the kinematics of ideal soils under plane strain conditions', *Journal of the Mechanics and Physics of Solids* 12(5), 337–351.

Sun, Y.-J. & Song, E.-X. (2016), 'Active earth pressure analysis based on normal stress distribution function along failure surface in soil obeying nonlinear failure criterion', *Acta Geotechnica* 11(2), 255–268.

Taylor, R. (1978), 'Properties of mining wastes with respect to foundations', *Foundation engineering in difficult ground* pp. 175–203.

Terzaghi, K. (1943), *Theoretical Soil Mechanics*, J. Wiley and Sons, inc.

Thornton, C. & Zhang, L. (2006), 'A numerical examination of shear banding and simple shear non-coaxial flow rules', *Philosophical Magazine* 86, 3425–3452.

Wyllie, D. C. (1980), 'Toppling rock slope failures examples of analysis and stabilization', *Rock Mechanics* 13(2), 89–98.

Yang, X.-L. (2007), 'Upper bound limit analysis of active earth pressure with different fracture surface and nonlinear yield criterion', *Theoretical and Applied Fracture Mechanics* 47(1), 46–56.

Yang, X.-L. & Huang, F. (2011), 'Collapse mechanism of shallow tunnel based on nonlinear Hoek–Brown failure criterion', *Tunnelling and Underground Space Technology* 26(6), 686–691.

Yang, X.-L., Li, L. & Yin, J.-H. (2004), 'Seismic and static stability analysis for rock slopes by a kinematical approach', *Géotechnique* 54(8), 543–549.

Yang, X.-L. & Long, Z.-X. (2015), 'Roof collapse of shallow tunnels with limit analysis method', *Journal of Central South University* 22(5), 1929–1936.

Yang, X.-L. & Yin, J.-H. (2005), 'Upper bound solution for ultimate bearing capacity with a modified Hoek–Brown failure criterion', *International Journal of Rock Mechanics and Mining Sciences* 42(4), 550–560.

Yu, H.-S. (2007), *Plasticity and Geotechnics*, Springer.

Yu, H., Salgado, R., Sloan, S. & Kim, J. (1998), 'Limit analysis versus limit equilibrium for slope stability', *Journal of Geotechnical and Geoenvironmental Engineering* 124(1), 1–11.

Zanbak, C. (1983), 'Design charts for rock slopes susceptible to toppling', *Journal of Geotechnical Engineering* 109(8), 1039–1062.

Zhang, G., Wang, F., Zhang, H., Tang, H., Li, X. & Zhong, Y. (2018), 'New stability calculation method for rock slopes subject to flexural toppling failure', *International Journal of Rock Mechanics and Mining Sciences* 106, 319–328.

Zhang, R. & Smith, C. (2019), 'Upper bound limit analysis of soils with a non-linear failure criterion', *Canadian Geotechnical Journal* .

Zhang, X. & Chen, W. (1987), 'Stability analysis of slopes with general nonlinear failure criterion', *International Journal for Numerical and Analytical Methods in Geomechanics* 11(1), 33–50.

Appendix **A**

Empirical method for multiple-tangent analysis

The case where there are 3 lines, but line 1 is tangent at the start of the interval, line 2 is tangent at the end of the interval, as shown in Figure 3.4. In this thesis, the two endpoints σ_G , σ_H are determined by the minimum and maximum normal stresses in the assumed uniform normal stresses distribution system. The analytical solution for determination of the optimal locations of tangency points is difficult to find since the area difference should be divided into three sections and more variables should be considered. Therefore, an empirical solution is given here instead of an analytical one: the optimal location of point σ_F (the value of normal stress at point F) is in the middle of the interval [σ_G , σ_H] since this analysis is similar to single tangential line analysis introduced above. It is more difficult to obtain the analytical solutions for the specific locations of the tangency points when more tangents are considered. Therefore an empirical solution is proposed below to provide a guidance for adopting the multi-tangent technique.

Similar to the 2-line analysis, the optimum locations of σ_{M1} and σ_{M2} should be determined in a 4-line analysis. In this thesis, the 4-line analysis adds one tangent at the start of the interval (σ_D shown in Figure 3.3) and the other tangent at the

end of the interval (σ_E shown in Figure 3.3) when compared with 2-line analysis. For 5-line analysis, two more tangents are added at the point $(\sigma_F + \sigma_G)/2$ and $(\sigma_F + \sigma_H)/2$ when compared with 3-line analysis. For all examples used in this thesis, if more tangents (tangent number > 5) are added, the calculated limit loads are almost the same no matter where the added tangents are located.

Appendix **B**

Non-linear approximation of a linear yield function

For validation purposes and also in order to access the stress values along a slip-line, it is useful to use the non-linear model described to represent a linear system by adopting a value of m very close to 1.0. The accuracy of this approximation can be calculated as follows:

Taking $a = 0$ for simplicity, the following can be written

$$\tau = c_0(\sigma_n/\sigma_t)^{1/m} \tag{B.1}$$

Let this equation and the linear form $\tau = c_{0l}(\sigma_n/\sigma_t)$ intersect at the origin and when $\sigma_n = \sigma_{n1}$. This defines the range of the approximation. Thus

$$c_{0l} = c_0(\sigma_{n1}/\sigma_t)^{(1-m)/m} \tag{B.2}$$

The difference between the linear and non-linear curves at any value of σ_n, as a proportion of the intersection value at σ_{n1} is given by:

$$\frac{c_0(\sigma_n/\sigma_t)^{1/m} - c_{0l}(\sigma_n/\sigma_t)}{c_0(\sigma_{n1}/\sigma_t)^{1/m}} \tag{B.3}$$

As shown in Figure B.1, a plot of this function shows that this has a maximum at around $0.4\sigma_n/\sigma_{n1}$ and is approximately equal to $0.37 \times (m-1)$ for small $m-1$.

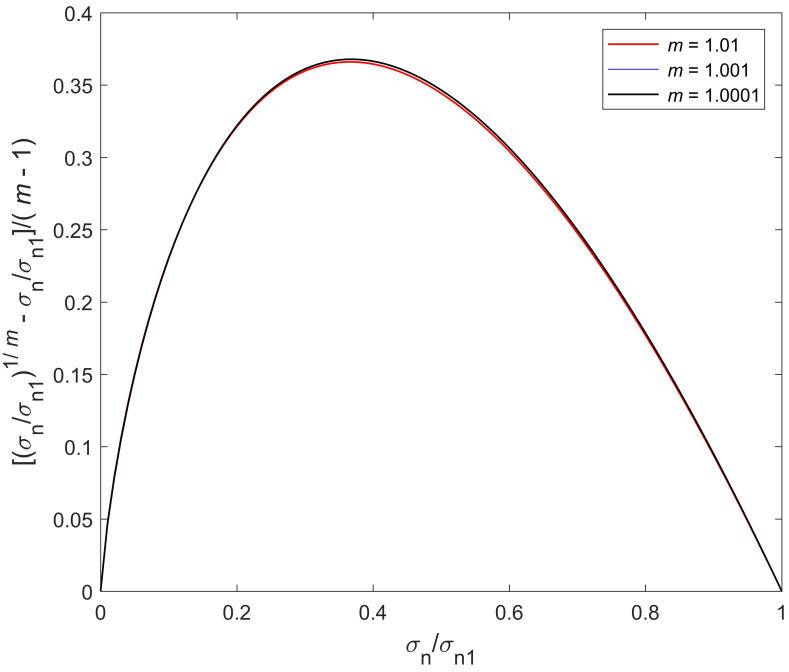

Figure B.1: Predicted value of function (Eq. B.3) against σ_n/σ_{n1} for small $m-1$.

Appendix C

Primal-dual derivation for non-associative permutation formulation

Step 1: we aim to minimize the following problem:

Objective:

$$\min \lambda$$

subject to:

$$\mathbf{Bq} - \lambda \mathbf{f}_{\mathrm{L}} = \mathbf{f}_{\mathrm{D}} \tag{C.1}$$

$$\mathbf{N}_{unc}^{T}\mathbf{q}_{unc} \leq \mathbf{C}_{unc}$$

$$\mathbf{N}_{for}^{T}\mathbf{q}_{for} = \mathbf{C}_{for}$$

Step 2: rearrange the expressions of the constraints making the right hand side term equal to zero:

$$\min \lambda$$

where the variables of the LP are $\mathbf{q}$ and λ ,

subject to:

$$-\mathbf{Bq} + \lambda \mathbf{f}_{\mathrm{L}} + \mathbf{f}_{\mathrm{D}} = 0 \tag{C.2}$$

$$\mathbf{N}_{unc}^{T}\mathbf{q}_{unc} - \mathbf{C}_{unc} \leq 0$$

$$\mathbf{N}_{for}^{T}\mathbf{q}_{for} - \mathbf{C}_{for} = 0$$

Step3: define a non-negative dual variable for each inequality constraint, and an unrestricted dual variable for each equality constraint: In our case, the variables corresponding to the previous equations will be $\mathbf{d}^{T}$ and $\mathbf{p}^{T}$ respectively. To constraints we associate variables $\mathbf{p}_{unc}^{T} \geq 0$; $\mathbf{d}^{T}$ and $\mathbf{p}_{for}^{T}$ are unrestricted.

Step4: for each constraint, eliminate the constraint and add the term (dual variable)*(left hand side of constraint) to the objective. Maximize the result over the dual variables:

$$\max \ \min \lambda$$

$+\mathbf{d}^{T}$(-Bq + $\lambda \mathbf{f}_{\mathrm{L}} + \mathbf{f}_{\mathrm{D}}$)

$+\mathbf{p}_{for}^{T}(\mathbf{N}_{for}^{T}\mathrm{q}_{for} - \mathbf{C}_{for})$

$+\mathbf{p}_{unc}^{T}(\mathbf{N}_{unc}^{T}\mathrm{q}_{unc} - \mathbf{C}_{unc})$

where it has been adopted the notation for the contract product vector-matrix, using the transposed when necessary.

Step5: group the new expressions so that the objective will appear as (primal variable)*(expression with dual variables), plus remaining terms involving only dual variables.

$$\max \ \min \mathbf{f}_{\mathrm{D}}^{T}\mathbf{d} - \mathbf{C}^{T}\mathbf{p}$$

$$+\lambda(1 + \mathrm{d}^{T}\mathbf{f}_{\mathrm{L}})$$

$$+\mathbf{q}^{T}(\mathbf{N}\mathrm{p}-\mathrm{B}^{T}\mathrm{d})$$

Step6: remove each term of the form (primal variable)*(expression with dual variables) and replace it with a constraint of the form:

- expression≥ 0, if the primal variable is non-negative;
- expression≤ 0, if the primal variable is non-positive;
- expression$= 0$, if the primal variable is unrestricted.

Thus the final dual problem states as follows.

$$\max \mathbf{f}_{\mathrm{D}}^{T}\mathbf{d} - \mathbf{C}^{T}\mathbf{p}$$

subject to:

$$\mathbf{N^{0}p} - \mathrm{B}^{\mathbf{T}}\mathbf{d} = \mathbf{0} \tag{C.3}$$

$$\mathbf{f}_{\mathrm{L}}^{T}\mathbf{d} = -1$$

$$\mathbf{p}_{unc} \geq \mathbf{0}$$

$$\infty \geq \mathbf{p}_{for} \geq -\infty$$

where $\mathbf{d}^T$ is a $3b-$ vector of nodal unconstrained displacement rates of the block centroids (corresponding to the nodal loads $\mathbf{f}$ in a virtual work sense). The discontinuity displacement rates in $\mathbf{d}$ and the resultant displacement rates in $\mathbf{p}$ ($\mathbf{p}_{for}$ is forced part; $\mathbf{p}_{unc}$ is unconstrained part) are the LP variables.

Which can also be expressed as:

$$\min \ -\mathbf{f}_{\mathrm{D}}^T\mathbf{d} + \mathbf{C}^T\mathbf{p}$$

subject to:

$$\mathbf{N^0p} - \mathrm{B}^{\mathbf{T}}\mathbf{d} = \mathbf{0} \tag{C.4}$$

$$\mathbf{f}_{\mathrm{L}}^T\mathbf{d} = -1$$

$$\mathbf{p}_{unc} \geq \mathbf{0}$$

$$\infty \geq \mathbf{p}_{for} \geq -\infty$$

where in all cases 0 is the zero vector. Note here than since there was an inequality in the equation corresponding to $\mathbf{p}$, it appears as a special variable defining the sign.

Appendix D

Explicit dual form for non-associative permutation method formulation

The dual of the equilibrium formulation is the kinematic solution, which is derived by duality principles. Similar to derivation of associative formulation, the kinematic non-associative permutation method formulation can be obtained. In the kinematic form, the objective function seeks to minimize the energy dissipated due to shearing along the discontinuities.

$$\min \ -\mathbf{f}_{\mathrm{D}}^{T}\mathbf{d} + \mathbf{C}^{T}\mathbf{p}$$

subject to:

$$\mathbf{N^0 p} - \mathrm{B}^{\mathbf{T}}\mathbf{d} = \mathbf{0} \tag{D.1}$$

$$\mathbf{f}_{\mathrm{L}}^{T}\mathbf{d} = -1$$

$$\mathbf{p}_{unc} \geq \mathbf{0}$$

$$\infty \geq \mathbf{p}_{for} \geq -\infty$$

where $\mathbf{d}^T$ is a $3b-$ vector of nodal unconstrained displacement rates of the block

centroids (corresponding to the nodal loads $\mathbf{f}$ in a virtual work sense). The displacement rates in $\mathbf{d}$ and the resultant displacement rates in $\mathbf{p}$ ($\mathbf{p}_{for}$ is forced part; $\mathbf{p}_{unc}$ is unconstrained part) are the LP variables. Due to the unrestricted $\mathbf{p}_{for}$ variable, it is not expected that this will generate realistic displacement rates.

Furthermore, for the same contact interface, the displacement rates contained in $\mathbf{u_i}$ are related to the respective non-negative resultant displacement rates in $\mathbf{p}_i$ as follows:

$$\mathbf{u_i} = \mathbf{N}_i^0 \mathbf{p}_i, \mathbf{p}_i \geq 0 \tag{D.2}$$

or in explicit form:

$$\begin{bmatrix} \varepsilon_i \\ \gamma_i \\ \kappa_i \end{bmatrix} = \begin{bmatrix} -l_i/2 & -l_i/2 & -\tan\psi_i & -\tan\psi_i \\ 0 & 0 & 1 & -1 \\ 1 & -1 & 0 & 0 \end{bmatrix} \begin{bmatrix} r_i^+ \\ r_i^- \\ v_i^+ \\ v_i^- \end{bmatrix}, \begin{bmatrix} r_i^+ \\ r_i^- \\ v_i^+ \\ v_i^- \end{bmatrix} \geq \begin{bmatrix} 0 \\ 0 \\ 0 \\ 0 \end{bmatrix} \tag{D.3}$$

where now $\mathbf{u}$ contains displacements along the joints, $\mathbf{u}^T = \{\varepsilon_1, \gamma_1, \kappa_1, \varepsilon_2, \gamma_2, \kappa_2 ... \varepsilon_c, \gamma_c, \kappa_c\}$, where ε_i, γ_i and κ_i are the displacement rates between blocks at joints i describing joint separation, sliding and rotation (related to $\mathbf{q}$ in a virtual work sense); $\mathbf{p}$ is a $(4c)$ vector of resultant displacement rates. The normality rule is satisfied when $\mathbf{N}_i^0 = \mathbf{N}_i$, i.e. when $\psi_i = \phi_i$.

In terms of non-associative case, for different cases of movement of the joint i, the Eq. D.2 has different forms:

(1) If the joint i only rotates. The Eq. D.2 should be converted to:

$$\begin{bmatrix} \varepsilon_i \\ \gamma_i \\ \kappa_i \end{bmatrix} = \begin{bmatrix} -l_i/2 & l_i/2 & -\tan\psi_i & -\tan\psi_i \\ 0 & 0 & 1 & -1 \\ -1 & 1 & 0 & 0 \end{bmatrix} \begin{bmatrix} r_i^+ \\ r_i^- \\ v_i^+ \\ v_i^- \end{bmatrix}, \begin{bmatrix} r_i^+ \\ v_i^+ \\ v_i^- \end{bmatrix} \geq \begin{bmatrix} 0 \\ 0 \\ 0 \end{bmatrix}, r_i^- \text{unrestricted;} \tag{D.4}$$

(2) If the joint i both rotates and slides. The Eq. D.2 should be converted to:

$$\begin{bmatrix} \varepsilon_i \\ \gamma_i \\ \kappa_i \end{bmatrix} = \begin{bmatrix} -l_i/2 & l_i/2 & -\tan\psi_i & -\tan\psi_i \\ 0 & 0 & 1 & -1 \\ -1 & 1 & 0 & 0 \end{bmatrix} \begin{bmatrix} r_i^+ \\ r_i^- \\ v_i^+ \\ v_i^- \end{bmatrix}, \begin{bmatrix} r_i^+ \\ v_i^- \end{bmatrix} \geq \begin{bmatrix} 0 \\ 0 \end{bmatrix}, r_i^-, v_i^+ \text{unrestricted;} \tag{D.5}$$

(3) If the joint i only slides. The Eq. D.2 should be converted to:

$$\begin{bmatrix} \varepsilon_i \\ \gamma_i \\ \kappa_i \end{bmatrix} = \begin{bmatrix} -l_i/2 & l_i/2 & -\tan\psi_i & -\tan\psi_i \\ 0 & 0 & 1 & -1 \\ -1 & 1 & 0 & 0 \end{bmatrix} \begin{bmatrix} r_i^+ \\ r_i^- \\ v_i^+ \\ v_i^- \end{bmatrix}, \begin{bmatrix} r_i^+ \\ r_i^- \\ v_i^- \end{bmatrix} \geq \begin{bmatrix} 0 \\ 0 \\ 0 \end{bmatrix}, v_i^+ \text{unrestricted.} \tag{D.6}$$

The dual of the associative equilibrium formulation is the kinematic solution, which is derived by duality principles. However this does not mean that the dual of the non-associative primal permutation formulation is a valid kinematic solution. The non-associative kinematic solution by analogous derivation of associative formulation should be checked.

Appendix E

Additional data for two-block study

E.1 Associative analysis

For the associative case, assuming ϕ =0.6283 (36°), for the equilibrium form, the result is

$$\text{Variables} \begin{bmatrix} q_1 \\ q_2 \\ q_3 \\ \lambda \end{bmatrix} = \begin{bmatrix} 1.1693 & 0.8496 & -0.4566 \\ 0.2330 & 0.1693 & -0.1165 \\ 1.8307 & 1.0000 & -0.9153 \\ 0.6165 & & \end{bmatrix}$$

When it comes to its kinematic form, the result is:

$$\text{Variables} \begin{bmatrix} d_1 \\ d_2 \\ p_1 \\ p_2 \\ p_3 \end{bmatrix} = \begin{bmatrix} -0.5143 & 0.3737 & 0 & \\ -0.2428 & 0.1214 & 0.2428 & \\ 0 & 0 & -0.5143 & 0 \\ 0 & 0.2428 & -0.3737 & 0 \\ 0 & 0.2428 & 0 & 0 \end{bmatrix}$$

$$\text{Joints displacement } \mathrm{u}_i = \mathbf{N}_i \mathbf{p}_i \begin{bmatrix} u_1 \\ u_2 \\ u_3 \end{bmatrix} = \begin{bmatrix} 0.3737 & -0.5143 & 0 \\ 0.3929 & -0.3737 & 0.2428 \\ 0.1214 & 0 & 0.2428 \end{bmatrix}$$

In associative case, it could be through analysis that the first joint will only slide along the direction at a dilation angle $\phi = \psi \ = 0.6283$ to the horizontal. The second joint will both slide and rotate and the third joint will only rotate, which agrees well with previous analysis.

E.2 Non-associative solutions

Using the proposed non-associative formulations based on permutation analysis, the results are shown below. With reference to the dual kinematic form of the block problem, a range of minimum values of λ could be obtained.
In the first case, the primal solution is:

Case 1. The first joint only slides; the second joint only rotates; the third joint only rotates: $\lambda = 0.5559$.

$$\text{Variables} \begin{bmatrix} q_1 \\ q_2 \\ q_3 \\ \lambda \end{bmatrix} = \begin{bmatrix} 0.9188 & 0.6676 & -0.4302 \\ 0.1117 & -0.0812 & -0.0559 \\ 2.0812 & 1.0000 & -1.0406 \\ -0.5559 & & \end{bmatrix}$$

For the case dilation angle $\psi_i = 0$ in kinematically dual form, the result is

Case 1.

$$\text{Variables} \begin{bmatrix} d_1 \\ d_2 \\ p_1^0 \\ p_2^0 \\ p_3^0 \end{bmatrix} = \begin{bmatrix} -0.3333 & 0 & 0 \\ -0.3333 & 0.1667 & 0.3333 \\ 0 & -0.3333 & \\ -0.3333 & 0 & \\ -0.3333 & 0 & \end{bmatrix}$$

$$\text{Joints displacement } \mathrm{u}_i = \mathbf{D}_i \mathbf{p}_i^0 \begin{bmatrix} u_1 \\ u_2 \\ u_3 \end{bmatrix} = \begin{bmatrix} 0 & -0.3333 & 0 \\ 0.1667 & 0 & 0.3333 \\ 0.1667 & 0 & 0.3333 \end{bmatrix}$$

Case 2. The first joint only slides; the second joint slides and rotates; the third joint only rotates: $\lambda = 0.6165$.

For the case dilation angle $\psi_i = \phi_i = 0.6283$ in primal form, the result is

$$\text{Variables} \begin{bmatrix} q_1 \\ q_2 \\ q_3 \\ \lambda \end{bmatrix} = \begin{bmatrix} 1.1693 & 0.8496 & -0.4566 \\ 0.2330 & 0.1693 & -0.1165 \\ 1.8307 & 1.0000 & -0.9153 \\ -0.6165 & & \end{bmatrix}$$

Case 2.

For the case dilation angle $\psi_i = \phi_i = 0.6283$ in kinematically dual form, the result is

$$\text{Variables} \begin{bmatrix} d_1 \\ d_2 \\ p_1 \\ p_2 \\ p_3 \end{bmatrix} = \begin{bmatrix} -0.5143 & 0.3737 & 0 & \\ -0.2428 & 0.1214 & 0.2428 & \\ 0 & 0 & -0.5143 & 0 \\ 0 & 0.2428 & -0.3737 & 0 \\ 0 & 0.2428 & 0 & 0 \end{bmatrix}$$

$$\text{Joints displacement } \mathrm{u}_i = \mathbf{N}_i^0 \mathbf{p}_i \begin{bmatrix} u_1 \\ u_2 \\ u_3 \end{bmatrix} = \begin{bmatrix} 0.3737 & -0.5143 & 0 \\ 0.3929 & -0.3737 & 0.2428 \\ 0.1214 & 0 & 0.2428 \end{bmatrix}$$

In this case which is as the same as the associative one, it could be through analysis that the first joint will only slide along the direction at a dilation angle $\phi = \psi \ = 0.6283$ to the horizontal. The second joint will both slide and rotate and the third joint will only rotate, which shows a good agreement with associative

result.

Case 3. The first joint only slides; the second joint only slides; the third joint only rotates: $\lambda = 0.5000$.

The primal result is

$$\text{Variables} \begin{bmatrix} q_1 \\ q_2 \\ q_3 \\ \lambda \end{bmatrix} = \begin{bmatrix} 1.3486 & 0.9798 & -0.0757 \\ 0.4798 & 0.3486 & 0.2399 \\ 1.6514 & 0.5202 & -0.8257 \\ -0.5000 & & \end{bmatrix}$$

Case 3. The first joint only slides; the second joint only slides; the third joint only rotates: $\lambda = 0.5000$.

For the case in kinematically dual form, the result is

$$\text{Variables} \begin{bmatrix} d_1 \\ d_2 \\ p_1 \\ p_2 \\ p_3 \end{bmatrix} = \begin{bmatrix} 0 & 0 & 0 & \\ -0.5000 & 0.2500 & 0.5000 & \\ 0 & 0 & 0 & 0 \\ 0.5000 & 0 & 0 & 0 \\ 0 & 0.5000 & 0 & 0 \end{bmatrix}$$

$$\text{Joints displacement } \mathrm{u}_i = \mathbf{N}_i^0 \mathbf{p}_i \begin{bmatrix} u_1 \\ u_2 \\ u_3 \end{bmatrix} = \begin{bmatrix} 0 & 0 & 0 \\ -0.2500 & 0 & 0.5000 \\ 0.2500 & 0 & 0.5000 \end{bmatrix}$$

From these data, it could be concluded that the kinematic failure mechanism for Case 3 is invalid since the first block is still but the taller block rotates.

As discussed above, in permutation analysis, there exist both primal and dual solutions for each movement case. From the point of primal-dual theory in this

work, if the results calculated from primal form and modified dual form put forward above are the same, it means the results are feasible solutions. By considering the combined physical effects on blocks movements, the possible range for non-associative solutions can be obtained straightforwardly.

Colophon

This thesis is based on a template developed by Matthew Townson and Andrew Reeves. It was typeset with LaTeX 2_ε. It was created using the *memoir* package, maintained by Lars Madsen, with the *madsen* chapter style. The font used is Latin Modern, derived from fonts designed by Donald E. Kunith.